



**AFRL-RX-WP-TR-2016-0071**

# **INTEGRATED MODELING OF POLYMER COMPOSITES UNDER HIGH ENERGY LASER IRRADIATION**

**Brent Volk, Gregory Ehlert, and Jeffery W. Baur  
AFRL/RXCC**

**Ajit Roy  
AFRL/RXAN**

**W. Joshua Kennedy, Keith Slinker, and Vikas Varshney  
Universal Technology Corporation**

**Trenton Godar  
University of Dayton Research Institute**

**30 OCTOBER 2015  
Interim Report**

**Distribution Statement A. Approved for public release; distribution unlimited.**

*See additional restrictions described on inside pages*

**STINFO COPY**

**AIR FORCE RESEARCH LABORATORY  
MATERIALS AND MANUFACTURING DIRECTORATE  
WRIGHT-PATTERSON AIR FORCE BASE, OH 45433-7750  
AIR FORCE MATERIEL COMMAND  
UNITED STATES AIR FORCE**

## NOTICE AND SIGNATURE PAGE

Using Government drawings, specifications, or other data included in this document for any purpose other than Government procurement does not in any way obligate the U.S. Government. The fact that the Government formulated or supplied the drawings, specifications, or other data does not license the holder or any other person or corporation; or convey any rights or permission to manufacture, use, or sell any patented invention that may relate to them.

This report was cleared for public release by the USAF 88th Air Base Wing (88 ABW) Public Affairs Office (PAO) and is available to the general public, including foreign nationals.

Copies may be obtained from the Defense Technical Information Center (DTIC)  
(<http://www.dtic.mil>).

AFRL-RX-WP-TR-2016-0071 HAS BEEN REVIEWED AND IS APPROVED FOR  
PUBLICATION IN ACCORDANCE WITH ASSIGNED DISTRIBUTION STATEMENT.

\_\_\_\_\_  
//SIGNATURE//  
PATRICK CARLIN, Project Engineer  
Composite Materials and Processing Section  
Composite Branch  
Structural Materials Division

\_\_\_\_\_  
//SIGNATURE//  
AMBER I. DAVIS, Chief  
Composite Materials and Processing Section  
Composite Branch  
Structural Materials Division

\_\_\_\_\_  
//SIGNATURE//  
ROBERT T. MARSHALL, Deputy Chief  
Structural Materials Division  
Materials And Manufacturing Directorate

This report is published in the interest of scientific and technical information exchange, and its publication does not constitute the Government's approval or disapproval of its ideas or findings.

# REPORT DOCUMENTATION PAGE

Form Approved  
OMB No. 0704-0188

The public reporting burden for this collection of information is estimated to average 1 hour per response, including the time for reviewing instructions, searching existing data sources, gathering and maintaining the data needed, and completing and reviewing the collection of information. Send comments regarding this burden estimate or any other aspect of this collection of information, including suggestions for reducing this burden, to Department of Defense, Washington Headquarters Services, Directorate for Information Operations and Reports (0704-0188), 1215 Jefferson Davis Highway, Suite 1204, Arlington, VA 22202-4302. Respondents should be aware that notwithstanding any other provision of law, no person shall be subject to any penalty for failing to comply with a collection of information if it does not display a currently valid OMB control number. **PLEASE DO NOT RETURN YOUR FORM TO THE ABOVE ADDRESS.**

1. REPORT DATE (DD-MM-YY) 30 October 2015			2. REPORT TYPE Interim		3. DATES COVERED (From - To) 22 July 2013 – 30 September 2015	
4. TITLE AND SUBTITLE INTEGRATED MODELING OF POLYMER COMPOSITES UNDER HIGH ENERGY LASER IRRADIATION					5a. CONTRACT NUMBER In-House	
					5b. GRANT NUMBER	
					5c. PROGRAM ELEMENT NUMBER 62102F	
6. AUTHOR(S) (See back)					5d. PROJECT NUMBER 4347	
					5e. TASK NUMBER	
					5f. WORK UNIT NUMBER X0S7	
7. PERFORMING ORGANIZATION NAME(S) AND ADDRESS(ES)  (See back)					8. PERFORMING ORGANIZATION REPORT NUMBER	
9. SPONSORING/MONITORING AGENCY NAME(S) AND ADDRESS(ES) Air Force Research Laboratory Materials and Manufacturing Directorate Wright-Patterson Air Force Base, OH 45433-7750 Air Force Materiel Command United States Air Force					10. SPONSORING/MONITORING AGENCY ACRONYM(S) AFRL/RXCC	
					11. SPONSORING/MONITORING AGENCY REPORT NUMBER(S) AFRL-RX-WP-TR-2016-0071	
12. DISTRIBUTION/AVAILABILITY STATEMENT Distribution Statement A. Approved for public release; distribution unlimited.						
13. SUPPLEMENTARY NOTES PA Case Number: 88ABW-2016-0050; Clearance Date: 07 Jan 2016. This report contains color.						
14. ABSTRACT (Maximum 200 words) This report is a summary of research activities funded by AFOSR Lab Task 13RXCOR. An integrated computational materials science and engineering (ICMSE) approach was used to investigate the role of fiber-matrix interfaces in controlling optical and thermal energy flow in structural composite materials subject to high energy laser irradiation. Modeling tools, including molecular dynamics and finite elements methods, were used to characterize optical and thermal transport at multiple length scales spanning from nanometers to millimeters. Advanced experimental characterization techniques were used to parameterize and validate these models. Two new experimental techniques were developed at AFRL as part of this project: lateral thermal transport measurements using scanning thermal microscopy (SThM), and microscale temperature sensing via gold nanorods. Modeling and experimental techniques are explained, and important considerations for future work are outlined. Peer-reviewed articles containing detailed results and analysis are included as an appendix.						
15. SUBJECT TERMS organic matrix composites, polymer matrix composites, lasers, thermal transport, ICMSE, molecular dynamics, finite element analysis, gold nanorods, nano-scale sensing, thermal gradients						
16. SECURITY CLASSIFICATION OF:			17. LIMITATION OF ABSTRACT:  SAR	18. NUMBER OF PAGES  106	19a. NAME OF RESPONSIBLE PERSON (Monitor) Patrick Carlin	
a. REPORT Unclassified	b. ABSTRACT Unclassified	c. THIS PAGE Unclassified			19b. TELEPHONE NUMBER (Include Area Code) (937) 904-5547	

## REPORT DOCUMENTATION PAGE Cont'd

### 6. AUTHOR(S)

Brent Volk, Gregory Ehlert, and Jeffery W. Baur – AFRL/RXCC

Ajit Roy - AFRL/RXAN

W. Joshua Kennedy, Keith Slinker, and Vikas Varshney - Universal Technology Corporation

Trenton Godar - University of Dayton Research Institute

### 7. PERFORMING ORGANIZATION NAME(S) AND ADDRESS(ES)

AFRL/RXCC Composites Branch  
Structural Materials Division  
Materials and Manufacturing Directorate  
Air Force Research Laboratory  
Wright-Patterson AFB, OH 45433-7750

AFRL/RXAN Nanoelectronic Materials Branch  
Functional Materials Division  
Materials and Manufacturing Directorate  
Air Force Research Laboratory  
Wright-Patterson AFB, OH 45433-7750

Universal Technology Corporation  
1270 N Fairfield Road  
Dayton, OH 45432-2600

University of Dayton Research Institute  
300 College Park Avenue  
Dayton, OH 45469-0001



## Table of Contents

<b><u>Section</u></b>	<b><u>Page</u></b>
List of Figures .....	ii
1 Overview .....	1
2 Approach .....	3
3 Develop an integrated optical and continuum model .....	4
3.1 COMSOL ® Multiphysics .....	4
3.1.1 2-D Idealized Geometry .....	4
3.1.2 3-D Dogbone Model .....	7
3.1.3 3-D Cross-sections .....	8
3.1.4 Complex Microstructure .....	8
3.2 Molecular Dynamics Modeling .....	9
3.2.1 Graphitic Orientation, Defect Density, and Hydrogen Saturation .....	11
3.2.2 Surface Functionalization .....	12
3.2.3 Interface Roughness and Carbon Nanotubes .....	12
3.2.4 Considerations .....	12
3.2.5 MD Summary .....	13
4 Compare modeled and experimental results .....	13
4.1 Nanoparticle Temperature Sensing .....	13
4.1.1 Nanorod Preprocessing .....	14
4.1.2 Dogbone Preparation .....	14
4.1.3 Resistive Heating .....	14
4.1.4 Direct Laser Heating .....	15
4.2 Scanning Thermal Microscopy .....	17
5 Conclusion .....	22
Appendix A. Molecular Dynamics for Modeling of Interface Thermal Resistance .....	23
Appendix B. Gold Nanorod Temperature Sensors .....	69
Appendix C. COMSOL ® Multiphysics .....	83
LIST OF ACRONYMS, ABBREVIATIONS, AND SYMBOLS .....	100

## List of Figures

<b><u>Figure</u></b>	<b><u>Page</u></b>
Figure 1: Key optical and thermal phenomena in laser interactions with composites.....	2
Figure 2: Understanding laser interactions in composite materials is fundamentally multiscale in nature.....	3
Figure 3: Example of one of the 2-D FEA models used to explore the dependence of energy flow on constituent properties in a simple composite system.....	5
Figure 4: Results from 2-D idealized model with local heat source.....	6
Figure 5: FEA model of dogbone sample with heat source from a single embedded carbon fiber.....	7
Figure 6: COMSOL ® model of a cross-sectional slice of the dogbone sample upon laser radiation of the fiber at one end or on the side .....	9
Figure 7: Multiphysics modeling of full microstructures.. .....	10
Figure 8: Interface features studied by MD. ....	11
Figure 9: Laser heating geometries for decoupling interface effects.....	16
Figure 10: Spectroscopically measured temperature maps for end-on laser heating of a carbon fiber with (left) and without (right) an insulating coating of $\text{Al}_2\text{O}_3$ .. .....	16
Figure 11: SEM of Thermalever probe from Anasys Instruments. ....	17
Figure 12: Schematic for semi-quantitative SThM measurements.....	18
Figure 13: Topographical map of a cross-section of a single carbon fiber emerging from the surrounding BMI matrix obtained via contact mode AFM.. .....	21
Figure 14: Scanning thermal microscopy of carbon fibers in a BMI matrix with a transverse heat flow. ....	22

# Integrated Modeling of Polymer Composites under High Energy Laser Irradiation

W. Joshua Kennedy, Gregory Ehlert, Keith Slinker, Vikas Varshney,  
Trenton Godar, Brent Volk, Ajit Roy, and Jeffery W. Baur

December 2015

## 1 Overview

The interaction of laser energy with organic matrix composites (OMCs) is important in a wide variety of processes relevant to both commercial and defense interests. For example, lasers are used in the machining of composites during laser cutting of bulk panels as well as for micromachining detailed features. Lasers are used in additive manufacturing processes, both in fused deposition modeling and laser sintering, and similar processes are desired for additive manufacturing of OMCs. Finally, high energy lasers make up one component of emerging threats to modern weapons systems. Understanding the fundamental interactions between lasers and OMCs will lead to increased option space for engineering desired responses.

This project proposed to address gaps in the community's understanding of laser interactions in OMCs through a combination of modeling and experimental efforts. Specifically, the project's tasks include the following.

1. Develop an integrated optical and continuum model for thermal and mechanical properties of composites under illumination from high energy laser.
2. Compare modeled and experimental results as a function of interface nanotailoring (modulation of absorption, thermal transport, and degradation).

3. Explore autonomous sensing and responsive concepts based on nanoparticle thermo-chromophores and smart materials.

A key challenge in each of these tasks is the multiscale nature of the relevant physics as illustrated in Figure 1. Optical energy can be transmitted, reflected, or absorbed by each individual component of the composite. Absorbed energy is efficiently transduced to heat, which then flows through individual components as well as across interface boundaries.

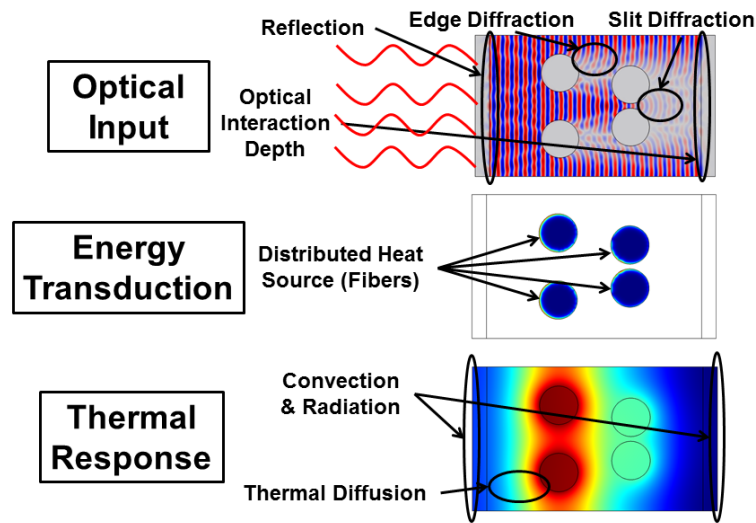


Figure 1: Key optical and thermal phenomena in laser interactions with composites.

As illustrated in Figure 2, bulk average optical properties are determined by nanoscale features such as constituent dielectrics and the nature of material interfaces. Thus, even thin coatings on fibers can have a substantial impact on the overall optical properties of a composite. Similarly, thermal interactions are important at the nano- (interfaces), micro- (material properties and structure), and macro- (bulk transport) scales. The approach taken in this project incorporates both modeling and experimental methods to understand, quantify, and tailor the key phenomena which regulate energy transduction multiscale transport. Importantly, this study does not address nonlinear interactions such as ablation, plasma generation, temperature-dependent optical responses, or thermochemical effects.

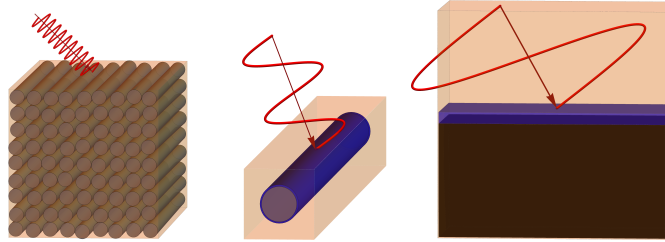


Figure 2: Understanding laser interactions in composite materials is fundamentally multiscale in nature. (left) Bulk heterogeneity determines overall optical and thermal transport in the material. (center) The interactions between material properties of the fiber, matrix, and any coatings determine the amount of optical energy that is absorbed and the rate of thermal transport, which is highly anisotropic. (right) The smoothness, relative index of refraction, and thermal resistance at the fiber-matrix interface are nanoscale phenomena that govern the properties at larger scales.

## 2 Approach

At both the nanoscale and the microscale, computational models are used to help develop a more detailed fundamental understanding of the energy transport within composites subject to high energy laser irradiation. At the micro- and macroscales, COMSOL® Multiphysics ® was used to generate finite element models (FEM) of simple and complex model systems of composites under laser irradiation. At the nanoscale the effects of both chemistry and structure on thermal transport have been explored by detailed molecular dynamics (MD) models. For each of these models, experimental techniques are developed to provide physical parameters and validate model predictions. MD models track thermal energy at the atomic level, and they are used to calculate the interface thermal conductance across the fiber-matrix interface. These parameters are notoriously difficult to measure experimentally, but a novel application of scanning thermal microscopy (SThM) was successfully used to measure the relative thermal conductance among fibers with various coatings. Similarly, recording the maximum temperature experienced within a composite is important for validating multiscale models, but such measurements are impossible in bulk samples using state-of-the-art thermometry techniques. As part of this project, a temperature sensor based on the thermal reshaping of gold nanorods was been developed.

This report summarizes the key findings of each these efforts, identifies pitfalls and challenges, and outlines potential routes forward. It is organized according to the key tasks listed in the Overview. The appendices comprise articles published in peer-reviewed journals which provide detailed results and analyses not found in the body of the report.

## **3 Develop an integrated optical and continuum model**

### **3.1 COMSOL® Multiphysics**

To develop an understanding of the fundamental constraints on energy flow within OMCs upon laser irradiation, finite element analysis (FEA) was employed to analyze optical interactions, opto-thermal transduction, and thermal transport in a variety of model systems. COMSOL® Multiphysics is a commercial FEA package that allows for multiple physics modules, solvers, and parameterizations in one, two, and three dimensions. Models were constructed in COMSOL® in variations of two basic geometries: an idealized 2-D system and several full 3-D systems representing experimentally realized configurations.

#### **3.1.1 2-D Idealized Geometry**

An idealized system consisting of a single cylindrical fiber embedded in a rectangular matrix was constructed to isolate the role of material properties in the response of composites to laser irradiation. This allows the study of the potential to tune laser response by varying constituent properties in a composite. First, analytical and computational models for the optical absorption by carbon fibers were used to determine whether or not the directionality of the heat input is significant. These computations indicate that any optical energy which penetrates the fiber surface is absorbed within tens of nanometers, and that optical energy is quickly and efficiently thermalized uniformly throughout the fiber. Thus, the 2-D multiphysics models are constructed using a direct heat source at the fiber, and one such model is shown in Figure 3. The dependence of resulting temperature profiles on bulk thermal conductivities, interface thermal conductance (modeled as a finite coating), surface

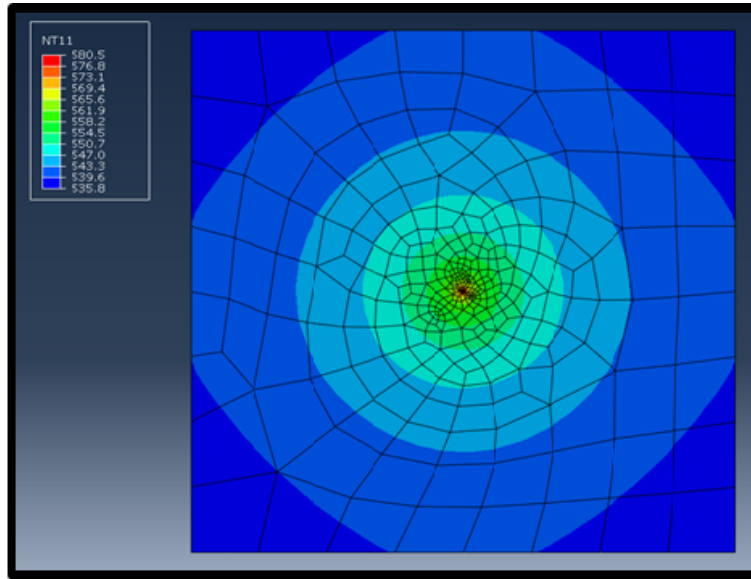


Figure 3: Example of one of the 2-D FEA models used to explore the dependence of energy flow on constituent properties in a simple composite system.

heat transfer coefficients (including convection and radiation), fiber optical properties, and input power were investigated using this model geometry.

Figure 4 shows the most important results from these models, and Appendix C comprises a conference report summarizing the most significant findings. It was found that, for uniform heat sources, the steady-state temperature gradient within the homogeneous matrix does not depend on interface thermal resistance. This is because at long times the energy balance is uniquely determined by the temperature at the outside boundary; the rate of energy flow out of the system depends only on temperature and the surface heat transfer coefficient.

However, two features of the temperature profile do depend on the interface resistance. First, the rate at which the resin heats up for a uniform heat source at the fiber is slower for larger values of the interface resistance. Second, the maximum steady-state temperature of the fibers is higher for larger values of the interface resistance. Both of these phenomena are a result of increased thermal energy storage in the fiber. Therefore, engineering the interface thermal resistance between the fiber and matrix allows for the control of heat rates and temperature distribution between the fibers and the matrix.

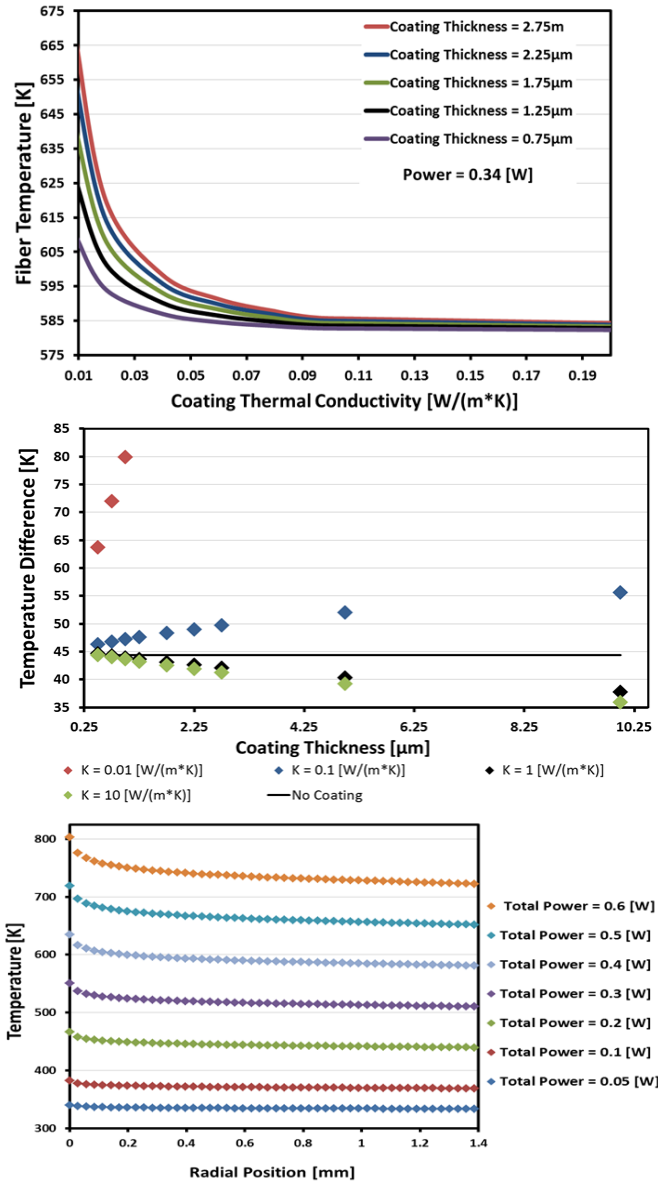


Figure 4: Results from 2-D idealized model with local heat source. (top) Fiber temperature as a function of coating thermal conductivity (ie, effective interface conductance) for several thicknesses of coatings. (middle) Temperature difference between the fiber surface and sample surface as a function of coating thickness for different values of the coating conductance. (bottom) Temperature profile in the resin for several values of input power.



### 3.1.2 3-D Dogbone Model

While the idealized model results give insights into the significance of various constituent material properties, they do not allow for quantitative predictions of energy flow because they rely on independent measurements of those properties. To connect model results to experimental measurements, a full 3-D “dogbone” geometry was created to analyze an experimentally realized model system (see Nanoparticle Temperature Sensing below). This system consists of a single carbon fiber spanning the length of a long, thin rod with wide, trapezoidal tabs at each end as shown in Figure 5 and Appendix B. The temperature profile was calculated under two scenarios: resistive heating of the fiber within the dogbone, and direct laser irradiation in cross-section. Resistive heating will be discussed here, and laser irradiation will be left for the experiment description to follow.

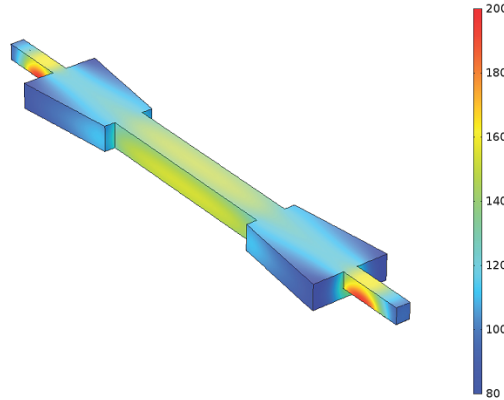


Figure 5: FEA model of dogbone sample with heat source from a single embedded carbon fiber.

In order to measure specific material properties for accurate FEA models, the COMSOL® model of the dogbone geometry was calculated for a wide variety of material properties. The bulk thermal conductivity, effective surface heat transfer coefficient, input power, and interface resistance were each varied, and the resulting steady-state temperature profile was calculated in each case. These temperature profiles were then compared, using an automated computer algorithm in Mathematica, to experimentally measured temperature profiles, and the parameter set corresponding to the lowest square deviation was chosen as representative of the physical system (see Ap-

pendix B and the Nanoparticle Temperature Sensing section below). Thus, the COMSOL® model was fully parameterized with experimental data from the corresponding physical system without needing to make several independent measurements of each property. This allows for the model to be used in a predictive way for more complex geometries (in which the corresponding physical parameters are even more difficult to directly determine). This success highlights one of the advantages of a truly integrated computational materials science and engineering (ICMSE) approach.

### **3.1.3 3-D Cross-sections**

Models were also constructed for the analysis of direct heating of discrete slices of the dogbone. As discussed in the experimental section below, direct laser heating at the end of an exposed fiber was used to circumvent some of the challenges involved in resistive heating. The COMSOL® models helped give insight into the role of the fiber-matrix interface in the axial energy flow under these conditions. Figure 6 shows typical COMSOL® results for this geometry. As with the idealized 2-D geometry, when the interface resistance is large the fiber heats up more. In the case of end-on heating this results in more thermal transport along the axis of the fiber and a more even distribution of temperature along the axial direction in the matrix. For low values of the interface thermal resistance the heat is readily wicked out of the fiber and the temperature profile is distributed in the resin near the irradiated surface.

### **3.1.4 Complex Microstructure**

Once the COMSOL® Multiphysics model was parameterized and validated by detailed temperature measurements in the dogbone geometry, it was then used to model a geometry more representative of structural composites. By incorporating known material properties into the fully vetted models, predictive computations are enabled that take advantage of the full power of the multiphysics solvers to obtain a complete picture of the energy transport in OMCs. As of the time of the writing of this report, these models continue to be developed for specific cases of interest. A general picture of the power of the fully parameterized model is illustrated in Figure 7. Recent efforts to fully quantify the thermal response to laser irradiation in OMCs using this approach are summarized in Appendix C.

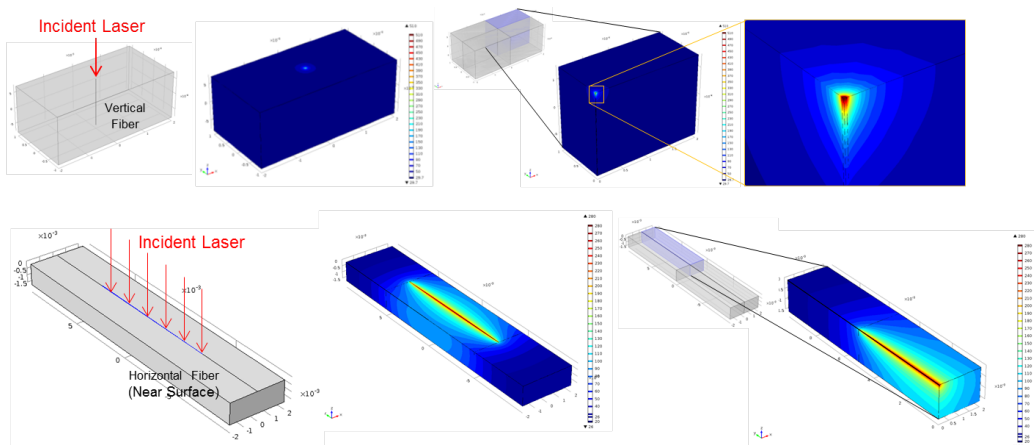


Figure 6: COMSOL® model of a cross-sectional slice of the dogbone sample upon laser radiation of the fiber at one end or on the side.

## 3.2 Molecular Dynamics Modeling

In highly filled, heterogeneous composite materials, heat phenomena are strongly affected by barriers to thermal transport across the interfaces between constituents. A molecular dynamics model was developed to investigate the thermal transport across the fiber-matrix interface for a variety of carbon fibers in a cross-linked bismaleimide (BMI) polymer matrix as summarized in Figure 8. A detailed description of the methods and results was published in ACS Applied Materials and Interfaces (see Appendix A). An ACS Conference Proceedings report is also included in Appendix A which describes some of the nuances related to varying time scales in the types of laser events of interest. An outline of the MD approach and summary of key conclusions is given here.

The first step in the MD approach is to generate the atomic coordinates for the fiber and the resin. For the BMI resin, monomeric molecules of 4, 4'-bismaleimidodiphenyl methane (BMPM) and O, O'-diallyl bisphenol A were constructed in Materials Studio and a collection of these monomers were placed at random to fill up the model region. The monomers were allowed to equilibrate through several steps as outlined in Appendix A, but the complex chemical cross-linking was not modeled via MD.

The carbon fiber surface was treated as crystalline graphite, but with several modifications. The graphitic orientation, presence of sp-3 hybridized

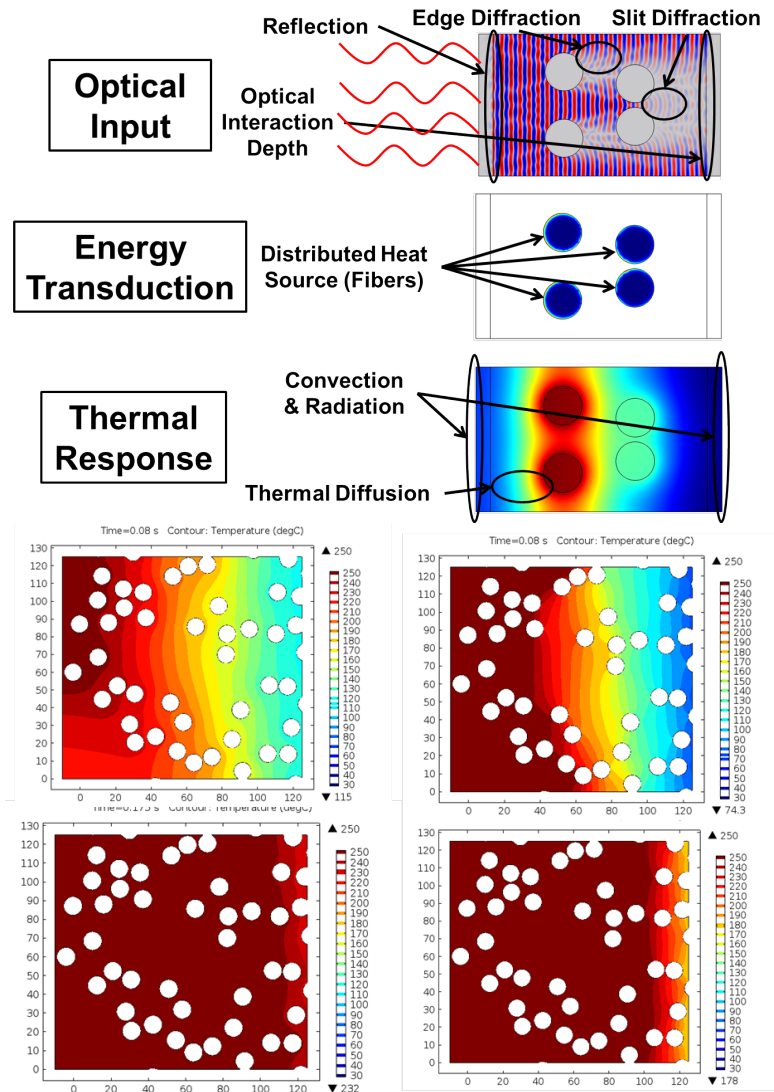


Figure 7: Multiphysics modeling of full microstructures. (top) Illustration of different physics captured by the model. (bottom) Model results for full, randomized microstructure including all relevant physics for interfaces with high (left) and low (right) interface thermal conductance.

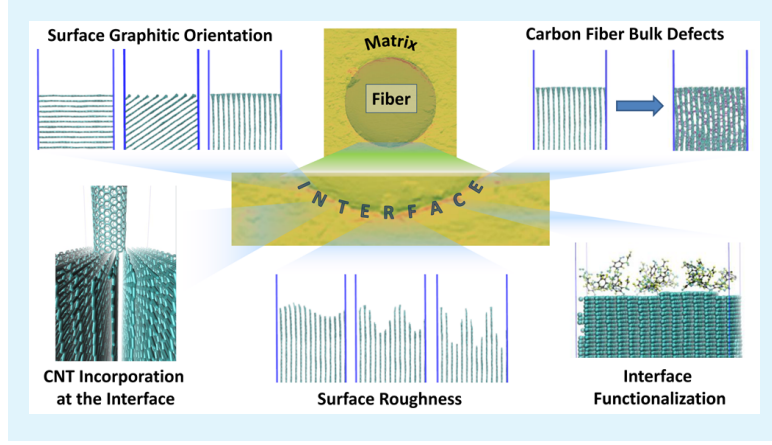


Figure 8: Interface features studied by MD.

“defects”, thickness of the modeled graphite region, surface functionalization, surface roughness, presence of carbon nanotubes, and amount of hydrogen saturation were all varied in the models. Each of these modifications corresponds to physical parameters that may be tuneable or otherwise amenable to designing an autonomous and/or adaptive response in the presence of optical or thermal energy.

In each case, the effective thermal conductance across the interface is calculated by enforcing a fixed heat flux across the interface and measuring the average temperature as a function of position along the flux. The interface thermal conductance is calculated according to

$$\Gamma = \frac{Q}{A\Delta T} \quad (1)$$

where  $Q$  is the heat flux,  $A$  is the cross-sectional area, and  $T$  is the temperature.

### 3.2.1 Graphitic Orientation, Defect Density, and Hydrogen Saturation

For unsaturated carbon fiber surfaces, the MD models predict a thermal conductance that decreases when the angle between the graphite planes and the interface increases (see Appendix A). This is attributed to the decrease in low frequency modes in the graphite planes compared to those present along

the  $\langle 001 \rangle$  direction, which couple readily into the matrix. For saturated surfaces, the larger atomic number density provided by the additional small hydrogen atoms increases this conductance for all orientations.

Conversely, the presence of sp-3 defects in the otherwise sp-2 graphite planes primarily serves to scatter these low frequency, out-of-plane modes and has minimal impact on the in-plane modes. Thus, at moderate defect densities ( $\sim 6 \text{ nm}^{-3}$ ) the interface conductance of every orientation becomes comparable to each of the others.

These results help extend current knowledge about thermal transport within carbon fibers having different atomic structure. The models provide valuable insights into the influence of fiber structure on bulk composite conductivity through variations in interface thermal conductance.

### **3.2.2 Surface Functionalization**

A common strategy for increasing interactions between dissimilar constituents in a composite material is via chemical functionalization. Within the MD system, functionalization is modeled by enforcing additional constraints during the model construction and by the addition of energy terms that reflect chemical bonds between certain monomers and the carbon fiber surface. As expected, the MD results show that the interface thermal conductance increases with increasing surface functionalization density (see Appendix A).

### **3.2.3 Interface Roughness and Carbon Nanotubes**

As the roughness of the fiber surface increases, so does the effective area over which heat transport can occur. Thus, in general, surface roughness increases the interface thermal conductance. Similarly, the presence of carbon nanotubes grown on the fiber surface extends the effective region of carbon into the matrix and thereby increases the thermal conductance. Quantifying this increase is difficult, however, because the interface itself becomes more ambiguous at the atomic level (see Appendix A).

### **3.2.4 Considerations**

There are two main gaps or limitations in the insights provided by the MD simulations. First, the MD models assume perfect interfaces, even with varying surface roughness and degree of functionalization. Any voids at the fiber surface, such as inevitably arise through any real manufacturing processes,

would tend to decrease the average interface thermal conductance. Also, the cross-linked BMI matrix is expected to have higher thermal conductivity than the un-cross-linked model system. This should result in a higher overall thermal conductance into the matrix, and this would be especially true for low frequency vibrational modes, potentially skewing the differences arising from graphitic orientation, functionalization, and bond saturation.

### **3.2.5 MD Summary**

These MD results offer new insights into the importance of several chemical and structural factors in determining the interface thermal conductance. This conductance, as shown later, is an important input in models at more coarse length scales, and it can make a large difference in the response of composite materials to laser irradiation.

## **4 Compare modeled and experimental results**

### **4.1 Nanoparticle Temperature Sensing**

A key requirement for the successful parameterization and validation of multiphysics models for composite material response to laser irradiation is the precise measurement of internal temperatures with high spatial resolution. While several high-resolution temperature sensing mechanisms exist, none of them allow for both three-dimensional mapping of temperature and the recording of temperature for ex-situ measurement. A major contribution of this project was to develop a solution with those capabilities. To that end, the optically detected, thermally induced shape transformation of gold nanorods in response to heating was used to invent a nanoparticle-based, microscale temperature recording technology.

The details of the experimental approach, innovative analytical techniques, and resulting technological application have been published in ACS Applied Materials and Interfaces, and the article is reproduced in Appendix B for reference. However, several experimental details have been omitted from that article and are included here for completeness.

#### **4.1.1 Nanorod Preprocessing**

In calibration samples, test samples, and dogbone specimens alike, careful processing of the nanocomposite is required to avoid unwanted shape change in the nanorods. Uncoated gold nanorods begin to change shape as soon as their temperature exceeds  $\sim 10 - 15^\circ \text{C}$ . Because this change is irreversible, any exposure to elevated temperatures before an experiment begins will reduce the dynamic range of potential temperature measurement. While investigations are currently under way to engineer nanomaterials with increased temperature capabilities, a preliminary approach to this problem was to identify a material system that did not require excessive heating in the fabrication stages.

Several materials were investigated for their usefulness as room-temperature cure systems. Various addition-cure epoxies and silicones were tested along with solution-cast thermoplastics such as polystyrene and polyethylene. Only the epoxy systems enabled facile dispersion of the CTAB-encapsulated nanorods without further chemical modification beyond the scope of the project. Room-temperature cures of these epoxies generally result in a very brittle material that is difficult to work with. Thus, a compromise between material properties and nanorod shape change was found for a moderate temperature cure, and the resulting cure cycle is detailed in Appendix B.

#### **4.1.2 Dogbone Preparation**

The preparation of the dogbone samples is delicate. First, a tool is machined from aluminum, and silicone molds are then cast from the tool. The overall geometry is modeled after common tensile testing specimens, but it includes an extra channel at each end of the specimen which is used to hold a single carbon fiber in place. Tape tabs are placed at each end of a single carbon fiber, and the fiber is draped across the mold with the tabs hanging off the end. The weight of the tabs provides tension during the cure. Resin is mixed and degassed in the usual way, and then it is slowly dispensed at each end of the mold using a wide pipette (ie, “eye-dropper”).

#### **4.1.3 Resistive Heating**

As discussed above, it was demonstrated that direct heating of the carbon fiber, such as through Joule heating, is a suitable surrogate for laser heating when the matrix is transparent. Thus, many of the experiments used for



comparison with the FEA models were heated by passing a current through the fiber embedded in the dogbone. This is accomplished by placing a small amount of silver paint directly into the silicone mold. The paint is dabbed onto the ends of the fiber before the resin is added. After curing, the spot of silver paint forms a contact pad at either end of the specimen. More silver paint is used to connect fine wires to the ends of the sample, and these wires are then used to inject current directly into the fiber.

Often the electrical resistance of these contacts is similar to, or even greater than, the resistance through the fiber. For the 2 inch long (PAN) carbon fibers used in these experiments the total resistance of the circuit was typically 10 – 30 k $\Omega$ . One consistent difficulty in resistively heating the dogbone samples arises from the CTE mismatch between the carbon fiber and the host. In many samples (> 50%) the thermal strain in the host caused the fiber to break, which breaks the electrical circuit and prematurely arrests the heating. The results published in Appendix B were those lucky few that survived the resistive heating, and so may be biased toward those with poor mechanical interfaces between the fiber and resin.

#### 4.1.4 Direct Laser Heating

To avoid the complications arising from resistive heating of the dogbones, an experiment was designed to realize direct laser irradiation of the fiber within the matrix. A diode laser with  $\lambda = 1.1\mu\text{m}$  was focused to a nearly diffraction limited spot size ( $\sim 2\mu\text{m}$  diameter gaussian beam). The beam was aligned to the fiber using an IR imaging camera in two ways as shown in Figure 9.

First, to create a heat source directly within the fiber, the laser was focused onto the exposed end of the fiber and the temperature profile was mapped using the gold nanorod sensors. As predicted by the COMSOL® models, different interface coatings gave rise to different temperature profiles in this configuration due to the differences in axial heat transport. Figure 10 shows two nanorod temperature maps: one with no coating, and one with an insulating ( $\text{Al}_2\text{O}_3$ ) coating.

Second, the samples were polished on one side until the fiber surface was nearly even with the matrix surface. A very thin layer (< 0.5 mm) of matrix material was left between the fiber and sample surface. This was done to avoid any direct heating of the matrix by the laser while maintaining the optical properties of the fiber-matrix interface. Unfortunately, these measurements had to be suspended due to lack of available equipment and

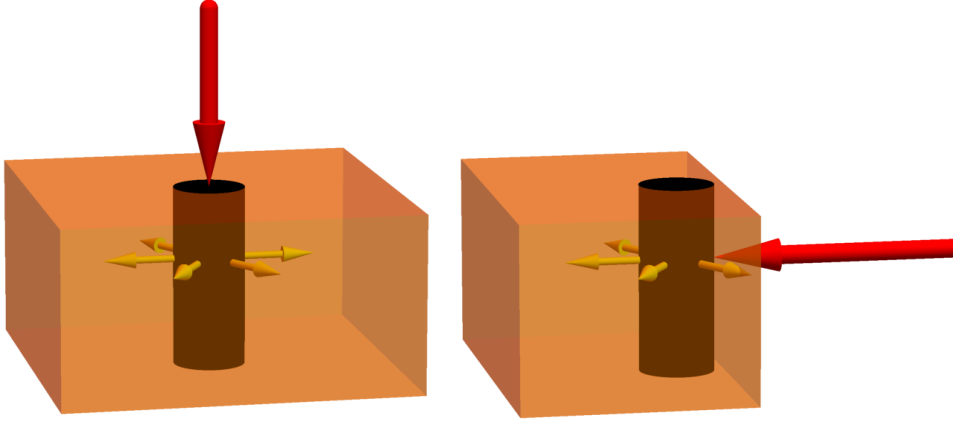


Figure 9: Laser heating geometries for decoupling interface effects. (left) End-on irradiation. (right) Edge irradiation.

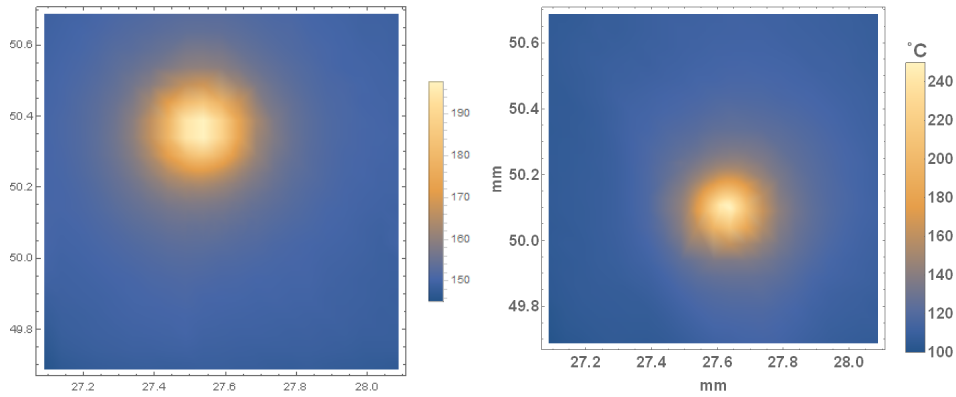


Figure 10: Spectroscopically measured temperature maps for end-on laser heating of a carbon fiber with (left) and without (right) an insulating coating of  $\text{Al}_2\text{O}_3$ . All spatial units are millimeters. Low thermal conductance (left) causes the heated zone to spread more in the axial direction, making the surface temperature distribution broader and the overall temperature lower. High thermal conductance (right) causes the heat to transfer into the matrix near the irradiation surface so that the overall temperature is higher, resulting in a sharper gradient.

space, so no temperature maps of these heating geometries are complete.

## 4.2 Scanning Thermal Microscopy

In order to verify some of the trends in interface thermal conductance predicted by the MD simulations, experimental approaches were developed to measure heat flow across an interface directly. Scanning thermal microscopy (SThM) is a class of nanoscale surface thermal measurements that employ a surface probe with some thermal functionality. The Anasys Instruments NanoIR2 is equipped with a module that enables the relative heat flux between a special tip, shown in Figure 11, and the sample.

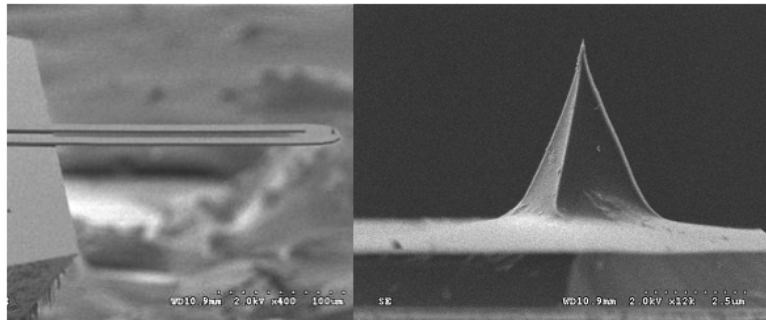


Figure 11: SEM of Thermalever probe from Anasys Instruments (<http://www.anasysinstruments.com/products/thermal-probes-tips-afm-sthm/>)

Typically, SThM is used to generate images using thermal conductivity as a contrast mechanism. Attempts to use probes such as the Thermalever probe shown in Figure 11 are complicated by the many conductive pathways between the measurement device and the sample. Careful calibration can be performed, but it requires a specialized and dedicated apparatus, usually under high vacuum and controlled environment.

In practice, the SThM probe is heated with a bias voltage to a few degrees above ambient temperature (or above the sample temperature), and the voltage across the probe is brought to zero by changing the value of a variable resistor placed opposite the probe in a wheatstone bridge configuration. As the temperature of the probe changes, so does its resistance, and the SThM signal consists of the voltage that appears. Positive voltages result when the resistance of the probe increases as a result of heat not flowing out

of the probe, and negative voltages indicate excess heat flowing out of the probe. Thus, in most SThM images bright regions correspond to low thermal conductance and dark regions correspond to high thermal conductance.

Even without quantitative calibration, useful information can still be obtained from the probe, but only relative properties between multiple samples can be reliably determined. By subjecting the surface to a constant heat flux along a prescribed direction, relative changes in temperature are associated with changes in the SThM voltage. These changes will be different for different materials, so the temperature gradient across two dissimilar materials is unquantifiable without additional knowledge of the heat transfer mechanisms in the immediate neighborhood. Nevertheless, for two samples of similar composition but different interfaces the relative interface thermal conductance can be calculated.

When the sample temperature is close to the ambient temperature, so that losses to the environment are minimized, it can be shown that the thermal resistance  $R$  across an interface of two materials having different effective thermal conductivities can be written as

$$R = m(T_1)(S_1 - S_2) \quad (2)$$

where  $S_n$  is the SThM signal (voltage) in region  $n$ , and  $m$  is a smoothly increasing function of temperature. For small changes in temperature (ie, small transverse heat fluxes as shown in Figure 12)  $m$  is approximately linear. Thus, the relative interface resistance between two interfaces can be measured by the ratio of the slopes of  $\Delta S(Q_T)$ , where  $Q_T$  is the heat flux in the plane of the surface.



Figure 12: Schematic for semi-quantitative SThM measurements.

Several specimens consisting of a single carbon fiber in a BMI matrix were fabricated, and the samples were polished to expose the cross-section of the fiber at the surface. The processing of test specimens for the SThM measurements deviates from standard procedures for neat resin and prepreg composites. Individual carbon fibers are suspended or draped across a wide,

flat silicone mold. Caution must be taken while pouring and curing the resin to avoid trapped bubbles and to preserve the relative position and orientation of sparsely distributed fibers through buckling of the neat resin during cure. The two components (one a liquid resin, the other a dry crystalline powder) are stirred by hand in a hot glycerin bath at 130° C until a uniform melt is obtained. When the viscosity decreases during melting the shear forces become insufficient to break up the dry component, and the mixture must be cooled to increase the viscosity. This is repeated several times until a uniform mixture is obtained.

Once the components are mixed the vessel is placed in a vacuum oven preheated to 150° C and the pressure is reduced to degas the mixture. The resin is held at elevated temperature and low pressure for 5 minutes and then removed from the oven. It is then poured carefully into the mold containing the carbon fibers and the mold is placed back in the vacuum oven at 150° C and low vacuum for 30 min more. By this time the resin has started to gel. The pressure is then increased to atmospheric pressure and the temperature is raised to the cure temperature of 240° C for 4 hours. In order to minimize the effect of topography, samples are polished according to the recipe in Table 1 until the difference between the fiber surface and the surrounding matrix is less than 200 nm. Care must be taken not to polish too vigorously or too slowly so as not to create a large difference between the fiber and matrix surfaces because of the difference in hardness between the two materials.

A variety of surface preparation techniques were attempted, including ion etching, focused ion beam milling, chemical etching, and microtome cutting. However, no technique consistently produces useable samples more often than the traditional polishing technique described in Table 1.

Figure 13 shows an atomic force micrograph (AFM) of one such sample. To measure  $S_1$  and  $S_2$  precisely requires a perfect interface boundary. In practice, however, this is never achieved. Key challenges in sample preparation include maintaining a minimum height difference between the fiber and the matrix, and a minimum gap between the fiber and the matrix at the surface. The height difference between the fiber and the sample will not contribute significantly to errors in the STHM signal as long as the difference is not greater than one third the height of the probe. To account for a physical gap between the fiber and the matrix we extrapolate the linear signal  $S(x)$  where  $x$  is the position along the trace. This approach introduces negligible error as long as the gap size in either direction is less than the probe height. The sample shown in Figure 13 has a height difference of less than 200 nm

Table 1: Polishing procedure for the preparation of samples for SThM measurements.

1. Using a diamond saw, cut slices of the material at right angles to the fiber into 3mm thick slabs.
2. Attach slabs to a fixed substrate using glue or crystal bond.
3. Grind the top surface using 400 grit SiC paper at 100 rpm until the surface is parallel to the mount and uniformly roughened. Rinse well with DI water.
4. Polish at successively finer grits (600, 800, & 1200 grit), pausing every 30-45 seconds during each step to insure that the surface is being uniformly abraded. If large streaks develop and are not polished easily, go back to the previous step. Clean thoroughly with DI water after each step.
5. Polish with 0.3  $\mu\text{m}$  alumina suspension on ChemoMet lapping cloth for 5-10 minutes to remove scratches.
6. Wash with detergent (Microsoap or equivalent) in water, then rinse with isopropanol and methanol/ethanol to remove any residue. Dry under flowing nitrogen.

and a gap width of less than 500 nm, which is sufficiently small for the probes that were used.

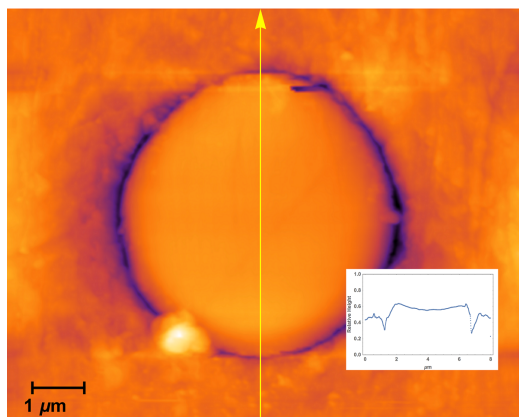


Figure 13: Topographical map of a cross-section of a single carbon fiber emerging from the surrounding BMI matrix obtained via contact mode AFM.

After the surface is prepared, the sample is mounted on a nickel puck for placement in the SThM apparatus. A local heat source along one edge is used to generate a net flux along the plane of the sample surface, and the resulting SThM signal is analyzed according to Equation 2 to find the relative interface thermal resistance.

Figure 14 shows a thermal micrograph for one sample and the plots of  $\Delta S(Q_T)$  for a carbon fiber with and without an alumina coating as a thermal barrier. The obvious increase in thermal resistance for an insulating coating demonstrates the type of information that can be obtained from SThM in this way. For the samples in Figure 14, PAN-based carbon fibers (Hexcel T300) were coated with 200 nm of alumina using atomic layer deposition (ALD). After coating, the interfacial thermal resistance between the fiber and the matrix increased by a factor of 2.18. This change is consistent with MD predictions for the effect of a roughened or functionalized surface, so it is still unclear what the underlying mechanism is for the increase. At the time of the preparation of this report, investigations are underway for samples that represent the types of surface modifications modeled by the MD systems, including varying the surface structure, functionalization, and presence of carbon nanotubes.

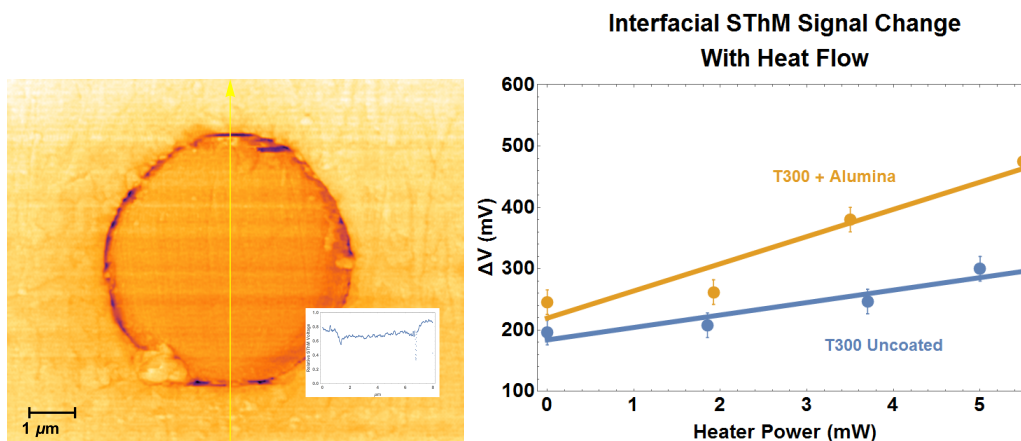


Figure 14: Scanning thermal microscopy of carbon fibers in a BMI matrix with a transverse heat flow. (left) SThM Micrograph. Inset shows the variation of the signal with position along the center line. (right) Signal differences at the interface as a function of transverse heat flow. The higher slope for the alumina-coated sample indicates a higher thermal resistance at the interface.

## 5 Conclusion

An ICMSE approach to understanding laser interactions in OMCs was developed across multiple length scales. Molecular dynamics and nanoscale surface probes were used together to determine the magnitude and influence of interface thermal resistance between carbon fibers and the polymer host. Finite element analysis was used along with high resolution measures of local temperature gradients to elucidate the influences of constituent material properties on optical and thermal energy transport in these materials. As part of this effort, a novel microscale temperature measurement technique was developed using gold nanorods. The knowledge and techniques developed during this project will be invaluable in future efforts to engineer adaptive responses to laser irradiation at the fiber-matrix interface.



## Appendix A. Molecular Dynamics for Modeling of Interface Thermal Resistance

# Modeling the Role of Bulk and Surface Characteristics of Carbon Fiber on Thermal Conductance across the Carbon-Fiber/Matrix Interface

Vikas Varshney,<sup>\*,†,‡</sup> Ajit K. Roy,<sup>†</sup> and Jeffery W. Baur<sup>\*,†</sup>

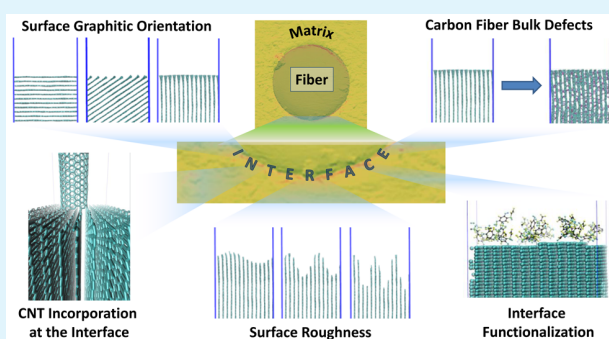
<sup>†</sup>Materials and Manufacturing Directorate, Air Force Research Laboratory, Wright-Patterson Air Force Base, Ohio 45433-7749, United States

<sup>‡</sup>Universal Technology Corporation, Dayton, Ohio 45432-2636, United States

## S Supporting Information

**ABSTRACT:** The rapid heating of carbon-fiber-reinforced polymer matrix composites leads to complex thermophysical interactions which not only are dependent on the thermal properties of the constituents and microstructure but are also dependent on the thermal transport between the fiber and resin interfaces. Using atomistic molecular dynamics simulations, the thermal conductance across the interface between a carbon-fiber near-surface region and bismaleimide monomer matrix is calculated as a function of the interface and bulk features of the carbon fiber. The surface of the carbon fiber is modeled as sheets of graphitic carbon with (a) varying degrees of surface functionality, (b) varying defect concentrations in the surface-carbon model (pure graphitic vs partially graphitic), (c) varying orientation of graphitic carbon at the interface, (d) varying interface saturation (dangling vs saturated bonds), (e) varying degrees of surface roughness, and (f) incorporating high conductive fillers (carbon nanotubes) at the interface. After combining separately equilibrated matrix system and different surface-carbon models, thermal energy exchange is investigated in terms of interface thermal conductance across the carbon fiber and the matrix. It is observed that modifications in the studied parameters (a–f) often lead to significant modulation of thermal conductance across the interface and, thus, showcases the role of interface tailoring and surface-carbon morphology toward thermal energy exchange. More importantly, the results provide key bounds and a realistic degree of variation to the interface thermal conductance values at fiber/matrix interfaces as a function of different surface-carbon features.

**KEYWORDS:** carbon fibers, BMI resin, molecular dynamics, interfaces, thermal conductance



## 1. INTRODUCTION

Today, laser technology is being used in a wide variety of fields including communications, industrial and environmental applications, medicine, and materials' research and development (R&D). Some of the key areas in materials' R&D include mass spectral analysis using matrix-assisted laser desorption/ionization (MALDI)<sup>1</sup> and fabrication and machining of micro-/nano-patterned surfaces and thin films using pulsed or continuous lasers (such as fabrication of nanoelectronic devices and patterning of polymeric nanocomposites).<sup>2,3</sup> Our specific interest lies in how different lasers interact with the polymeric composite materials, what parameters govern the interaction behavior, and how these laser–composite interactions lead to evolution of composites' thermophysical properties over time.

The basic mechanism of laser interaction with materials involves many nonequilibrium processes (thermal, mechanical, chemical, and physical) at varying length and time scales caused by fast deposition of laser energy and its dissipation in various forms.<sup>4,5</sup> Because of the rapid heating rate, these non-

equilibrium processes cause spatial variability in thermophysical and mechanical properties of the matrix such as local heating, local matrix degradation due to sudden local increase in temperature, pressure wave formation, etc.<sup>4,5</sup> In the context of polymeric composites, it is often desired to delay the onset of ablation and keep the composite intact by tailoring the interfaces between matrix and fillers (such as carbon fibers, carbon nanotubes, exfoliated graphite/graphene, and metallic nano-/micro-particles, etc.) by modulating the interactions between the two components. Since the ablation onset is primarily driven by a rise in temperature, it becomes crucial to understand individual thermal conduction characteristics of the matrix and fillers (thermal conductivity), as well as of their mutual interface (interface thermal conductance).

**Received:** September 11, 2015

**Accepted:** November 9, 2015

**Published:** November 9, 2015

Within the framework of carbon-fiber-based nano-/micro-composites, several experimental techniques (laser flash, photoacoustic,  $3\omega$ , thermoreflectance, infrared microscopy, etc.) have been employed to measure the thermal conductivity of individual components as well as the “effective” thermal conductivity of the nanocomposites.<sup>6,7</sup> However, because of the small length scales involved, it has been significantly challenging to directly and accurately measure the nanocomposite interface features, both morphological (roughness, interfacial bonding nature, fractional contact area, etc.) and thermal transport characteristics. Most of the experimentally reported values of interface thermal conductance for carbon-based nanocomposites are evaluated indirectly (fitting the measured experimental data using different mathematical models, often requiring thermal properties of individual components as input parameters).<sup>8–14</sup>

On the contrary, because of the sharpness of molecular interfaces, atomistic molecular dynamics (MD) simulations<sup>15</sup> offer an alternative as well as a direct approach to calculate the thermal energy exchange across matrix/filler interfaces in terms of interface thermal conductance. In these simulations, only the details of microscopic interactions need to be specified (often extracted using quantum chemical calculations) and no further assumptions need to be made in order to investigate the equilibrium or nonequilibrium phenomenon happening at these time scales. To date, within the framework of carbon/polymeric interfaces, most molecular modeling reports have estimated thermal conductance primarily with either carbon nanotubes or single/few-layer graphene (1–2 nm fillers).<sup>14,16–30</sup> Furthermore, in many of these studies, interface functionalization has been used as the key parameter to tailor the interfacial thermal transport characteristics.<sup>18,20,23,24,27,29,30</sup>

In principle, apart from interface functionalization, several other parameters could be altered to modulate the thermal transport across carbon-fiber/matrix interfaces. This could include *interface characteristics* such as interface roughness, the nature of dangling bonds, incorporation of high conductive fillers (nanotubes, metal nanoparticles) at the interface; *carbon-fiber characteristics* such as its amorphous or graphitic nature and graphitic orientation near the interface; and *matrix features* such as degree of curing, local crystallinity, or molecular order near the interface, etc. To the best of the authors’ knowledge, these parameters have either not been explored or been explored in a very limited way from the perspective of interface thermal conductance across carbon-fiber/matrix interfaces.

This work addresses several of the highlighted issues to (a) model different types of carbon-fiber surface models ranging between ~5 and ~17 nm (mimicking the near-surface region of carbon fiber to a much larger scale than what is reported to date); (b) model high-temperature BMI monomeric resins (specifically Matrimid BMI-5292 because of its high temperature stability) with atomistic resolution; and (c) model the effect of the aforementioned parameters (including functionalization) on carbon-fiber/BMI-matrix interfacial thermal transport in a single comprehensive study.

It is important to point out that while modeling thermal transport across carbon-fiber/crosslinked resin is ideal, the following study investigates the transport characteristics across its uncrosslinked counterpart because of the following reasons. (A) Cross-linking reactions in BMI are notably more complex than well-studied epoxy-based resins. For example, unlike curing in epoxy, BMI curing consists of five different reaction pathways;<sup>31,32</sup> (B) Specific reaction pathways are temperature

dependent, and their relative importance to experimental conditions are not well-quantified. (C) Inclusion of cross-linking would significantly broaden the scope of the investigation, i.e., investigating the effect of the degree of curing and the effect of different reactions and their relative occurrence on investigated properties, etc. We do, however, discuss the possible modulation of interfacial thermal transport because of curing phenomenon toward the end of the article. Understanding thermal transport across the carbon-fiber and monomeric matrix interface is also pertinent from the perspective of laser-assisted curing of carbon-fiber composites. Here, the interfacial thermal transport is expected to govern the heat flow from carbon fiber to the matrix (most of the laser energy is absorbed by the carbon fiber), subsequently determining the temperature rise and distribution in the monomeric matrix and thus affecting its curing kinetics.<sup>31,32</sup>

## 2. SIMULATION SETUP AND METHODOLOGY

The section is divided into five subsections, dealing with the (a) preparation of BMI matrix, (b) preparation of different surface-carbon and (c) interface models, (d) preparation of combined systems for thermal conductance calculations, and (e) simulation methodology for thermal conductance calculations.

**2.1. Matrix Preparation.** The BMI resin (Matrimid BMI-5292) is composed of 4,4′-bismaleimidodiphenyl methane (BMPM) and O,O′-diallylbisphenol A (DABPA) monomers, often in a 1:1 molar ratio.<sup>33,34</sup> The schematic representations of these monomers, along with their molecular structures, are shown in Figure 1. As a part of the initial

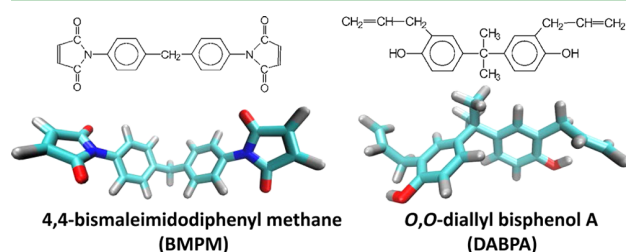


**Figure 1.** Molecular structure and schematic representation of the two monomer components of the Matrimid BMI-5292 resin. Color scheme: cyan, carbon; blue, nitrogen; red, oxygen; silver, hydrogen.

simulation setup, these monomers were constructed in Materials Studio.<sup>35</sup> Among several all atom force fields tested (CVFF,<sup>36</sup> PCFF,<sup>37</sup> and GAFF<sup>38,39</sup>) for successful generation of bonded and nonbonded parameters, only the general amber force field (GAFF) was able to generate all of the required parameters. Hence, GAFF parameters were employed to model the BMI matrix as well as all carbon-surface models for this study. It is often reported that when employing GAFF force field, restrained electrostatic potential (RESP) charges are best suited to model organic or biomolecules.<sup>38,39</sup> For our simulations, RESP charge estimations and fittings were performed using GAUSSIAN09 software<sup>40</sup> and RESP code within the framework of the R.E.D. program.<sup>41</sup> The LAMMPS package was employed to carry out all molecular dynamics simulations.<sup>42</sup> For van der Waals interactions, a distance cutoff value of 12 Å was used while PPPM (particle–particle–particle mesh) technique was used to model long-range Coulombic interactions as implemented in LAMMPS.

First, a system of ~9500 atoms was created by replicating both BMI monomers 108 times (total) along  $x$ -,  $y$ -, and  $z$ -directions. Following the initial minimization, MD simulations were carried out in NVT (canonical) ensemble to equilibrate the temperature at 300 K for 200 ps, followed by NPT (isothermal–isobaric) ensemble to equilibrate the density (and pressure) for 5 ns with independent barostats along the  $x$ -,  $y$ -, and  $z$ -directions. Afterward, 200 ps equilibration was performed in NVE (microcanonical) ensemble to confirm the energy

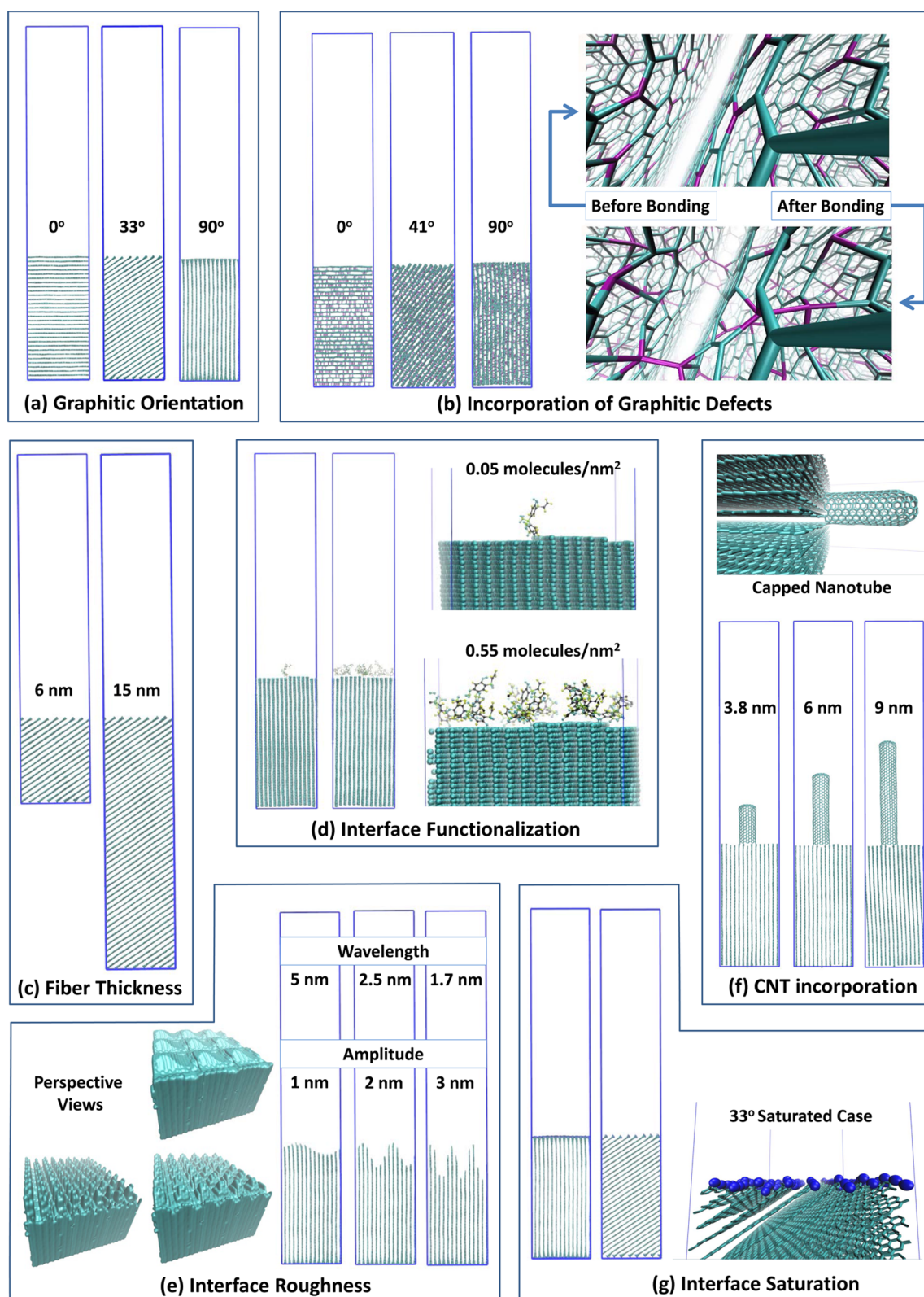


**Figure 2.** Several schematics of generated carbon-fiber surface models pertaining to (a) graphitic orientation; (b) incorporation of  $\text{sp}^3$  defects within the graphitic structure (structure before and after bonding is also shown; purple,  $\text{sp}^3$  carbon atoms; cyan,  $\text{sp}^2$  carbon atoms); (c) effective fiber thickness; (d) interface functionalization (close-up interface region of two functionalized cases is also shown); (e) interface roughness with different roughness wavelengths and amplitude (perspective view is shown to reveal two-dimensional roughness features); (f) incorporation of bonded CNTs at the interface (close-up picture of nanotube cap is also shown); and (g) saturation of interface bonds (saturated H atoms are shown as blue spheres in close-up perspective).



conservation of the equilibrated system. For these simulations, periodic boundary conditions were employed in all three orthogonal directions to mimic bulk-like behavior. A time step of 1.0 fs was used during the equilibration phase. After successful equilibration, the system was subjected to a series of additional simulations for estimation and experimental comparison of the glass transition temperature, room temperature density, coefficient of thermal expansion, and thermal conductivity for the validation of the employed force field, which are reported elsewhere.<sup>43</sup>

**2.2. Carbon-Surface Models: Bulk Features Preparation.** Intrinsic carbon-fiber parameters such as graphitic order and its orientation with respect to heat flow direction, content of amorphous carbon within the carbon fiber, and  $sp^2/sp^3$  bond ratio are important parameters which impact its bulk thermal transport characteristics. In principle, these parameters could also affect how interfaces of such fibers with organic matrices respond to an applied thermal gradient. In order to explore this, we generated several of such models incorporating differences in the aforementioned bulk carbon-fiber features which are discussed as follows.

**2.2.1. Graphitic Orientation.** In order to investigate the impact of graphitic layer orientation on interfacial thermal transport, several carbon-surface models were created with several different orientation angles of graphitic layers, ranging from  $0^\circ$  to  $90^\circ$  with respect to the  $x$ -direction (parallel to the interface). We will refer to these cases as  $C_\theta$ , where  $\theta$  represents the orientation angle of the graphitic layers with respect to the interface. Several models, with orientation angles of  $0^\circ$ ,  $8^\circ$ ,  $16^\circ$ ,  $24.5^\circ$ ,  $33^\circ$ ,  $41^\circ$ ,  $51^\circ$ ,  $66^\circ$ , and  $90^\circ$  were created using in-house scripts with a fiber surface thickness of 10 nm. The details of building the carbon-surface models with different orientations are outlined in [Supporting Information](#) section S1. [Figure 2a](#) shows a few representative cases of carbon-surface models with graphitic orientations of  $C_0$ ,  $C_{33}$ , and  $C_{90}$ .

**2.2.2. Incorporation of Defects.** From the perspective of defects inclusion, pristine graphitic and amorphous carbon fibers represent two extremes of structural order. While models of pristine graphitic carbon are discussed in earlier text, interface thermal conductance across amorphous carbon and BMI matrix was recently modeled by us and is discussed elsewhere.<sup>43</sup> In this study, we create partially defective graphitic carbon-fiber surface models and investigate the effect of structural graphitic defects within carbon fibers on thermal conductance across fiber/matrix interfaces.

The defective graphitic carbon models can either be generated by incorporating defects in the pristine graphite or incorporating graphitic order starting from fully amorphous carbon.<sup>44</sup> For this study, the former route is chosen to create graphitic models with defects.<sup>45</sup> In this approach, we create interlayer bonding between carbon atoms and modify their hybridization from  $sp^2$  to  $sp^3$ . Here, we make use of the fact that, in AB layer stacking of graphite, there is one set of atom pair which lie on top of each other (looking along the  $c$ -axis), where atoms are 3.4 Å apart.<sup>46</sup> We randomly choose a predetermined number of such pairs (based on the final defect concentration), move atoms in each pair closer toward each other (1 Å each), and create a bond between the two. The bond creation is followed by updating the surrounding topology information (adding several new bond angles and dihedral angles and deleting two improper angles). By doing so, several models were created with volumetric defect concentrations ranging up to  $\sim 6$  defects/nm<sup>3</sup> for three graphitic orientations, namely,  $C_0$ ,  $C_{41}$ , and  $C_{90}$ , and are shown in [Figure 2b](#), which also shows the structural changes before and after the bond creation for a representative case.

**2.2.3. Fiber Surface Morphology Thickness.** In order to explore the effect of thickness of fiber surface morphology (effective system size in MD simulations), several models were created with varying carbon-fiber thicknesses along the  $z$ -direction. Here, the  $C_{41}$  graphitic orientation model with thickness values ranging from 6 to 18 nm were created by deleting atoms on the boundaries of a much longer  $C_{41}$  model along the  $z$ -direction. Two of the created systems are shown in [Figure 2c](#).

**2.3. Carbon-Surface Models: Interface Features Preparation.** In addition to bulk carbon-fiber surface characteristics, interface

modification can also provide substantial modulation of interfacial thermal transport characteristics as evident from previous studies, mainly focused on functionalization.<sup>18,20,23,24,27,29,30</sup> Below, we detail other interface modifications (in addition to functionalization) that can be employed to modify interface thermal conductance across fiber/matrix interfaces.

**2.3.1. Functionalization.** In order to investigate the effect of interface functionalization, five different carbon-surface models were created using graphitic orientation model  $C_{90}$  with a surface functionalization density ranging from 0.05 to 0.55 molecules/nm<sup>2</sup>. Among different graphitic orientation models, the  $C_{90}$  model was chosen for interface functionalization studies because of two primary reasons; (a) in literature, most investigations dealing with the effect of interface functionalization on thermal conductance have been performed on  $C_0$  type interfaces, such as the side wall of CNTs or surface modification in single-layer/few-layer graphene, and their outcomes are well-investigated; and (b) the  $C_{90}$  model provides the most number of possible functionalization sites because of the most number of edge carbon atoms among nonzero graphitic orientation models. For the  $C_{90}$  model, interface functionalization was carried out by bonding one of the monomers (DABPA) to the edge carbon atoms of a  $C_{90}$  carbon surface. In order to carry out bonding at the interface, first, a combined system of a BMI-matrix and  $C_{90}$  graphitic model was created. Then, a predetermined number of DABPA molecules were slowly dragged to the carbon-fiber surface over the course of an NVT MD simulation. Thereafter, bonds were created between the “hydroxyl O” (of DABPA) and “nearest edge carbon atom” using an in-house script, also updating new topology information (angles, dihedrals, and new force-field parameter assignment, etc.). The full procedure for functionalization and updating topology is outlined in detail in [Supporting Information](#) section S2. A few representative functionalized DABPA monomers (surrounding matrix removed for clarification) are shown in [Figure 2d](#).

**2.3.2. Roughness.** The effect of carbon-fiber surface roughness on interfacial thermal transport was modeled by creating rough graphitic edges for a  $C_{90}$  graphitic system (Please see [Supporting Information](#) section S3 for specific details regarding generation of various roughness models). Here, nine carbon-surface models were created with varying sinusoidal roughness features (amplitude and wavelength) along both  $x$ - and  $y$ -directions. Specifically, roughness with three different amplitudes, i.e., 1, 2 and 3 nm, and 3 different wavelengths, i.e.,  $\sim 1.7$ ,  $\sim 2.5$ , and  $\sim 5$  nm, were modeled. A few schematic carbon-surface models with varying roughness features are shown in [Figure 2e](#).

**2.3.3. CNT Incorporation at the Interface.** In addition to functionalization and roughness, incorporating highly conductive nanofillers at the interface can also significantly modulate interfacial thermal transport. For example, CNTs grown directly in carbon fibers (also known as fuzzy carbon fibers) could provide additional surface area to interact with the matrix, potentially enhancing overall thermal transport characteristics. In order to mimic such an interface, several models were created by covalently bonding (10,10) end-capped single-wall CNTs of different lengths ( $\sim 3.8$ ,  $\sim 6$ , and  $\sim 9$  nm) to a  $C_{90}$  carbon-surface model. The end-capping of the CNTs was achieved using NanoCap software.<sup>47</sup> The details of the bonding, such as how the junction was created along with other specific details, are outlined in [Supporting Information](#) section S4. The schematic representations of all three CNT bonded carbon-surface models are shown in [Figure 2f](#).

**2.3.4. Interface Saturation.** From previous discussion, it should be noted that our graphitic carbon surface models ( $C_8$ – $C_{90}$ ) have unsaturated or undersaturated valence for the edge atoms. In order to estimate if saturation of such valence could have significant impact on interfacial thermal transport, we saturated four of the nine graphitic models, namely,  $C_{16}$ ,  $C_{33}$ ,  $C_{51}$ , and  $C_{90}$ , with hydrogen atoms for interface thermal conductance calculations. The visual differences between unsaturated and saturated surface-carbon atoms are shown in [Figure 2g](#) for the  $C_{33}$  graphitic model.

Afterward, each of the prepared carbon-surface models was subjected to equilibration in NVT, NPT, and NVE ensembles for

200, 2000, and 200 ps with time steps of 1, 1, and 0.5 fs, respectively, prior to combining with the matrix.

**2.4. Combined Preparation.** To calculate interface thermal conductance across the fiber/matrix interface, combined systems were created using relaxed BMI-matrix and separately equilibrated surface-carbon models (graphitic orientation, defects, fiber thickness, roughness, and interface saturation) to mimic the fiber/matrix interface (Figure 3a). We should point out that functionalized and CNT-

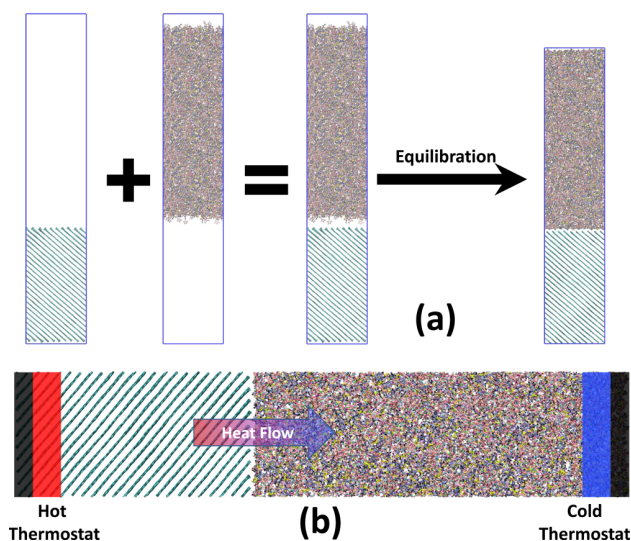


**Figure 3.** (a) Schematic representation of how the combined systems were prepared. It should be noted that the equilibrated structure (extreme left) has a lesser volume. (b) Schematic of nonequilibrium molecular dynamics simulations as employed in this investigation for a representative case. Color scheme: black, fixed atoms; red, hot thermostated atoms; blue, cold thermostated atoms. Thermal energy is directed from the graphitic carbon surface toward the matrix.

incorporated systems were combined during carbon-surface model preparations as discussed in Supporting Information sections S2 and S4, respectively. For the remaining cases, an in-house script was written to merge the two structures in order to generate the initial combined geometries. Within this code, the BMI matrix in the equilibrated slab-like geometry (4 times replication along the *z*-direction of the original system followed by its equilibration) was combined with the equilibrated carbon-surface models to generate initial coordinates for modeling matrix/fiber interface systems in LAMMPS format (Figure 3a) (~60,000 atoms in each simulation). While combining both structures, a 5 Å gap was purposely included to avoid overlap of atoms. Interaction between the matrix and fiber was evaluated using van der Waals interactions. Prior to thermal conductance simulations, all combined systems were equilibrated for 200, 2000, and 200 ps in *NVT*, *NPT*, and *NVE* ensembles, respectively, with respective time steps of 1, 1, and 0.5 fs. We should point out that, during equilibration, the orientation angle for  $C_{90}$  cases was eventually equilibrated to  $\sim 83^\circ$ , while orientation angles for other graphitic cases did not change to a noticeable degree.

**2.5. Interface Thermal Conductance Calculations.** The thermal conductance across BMI-matrix surface-carbon models' interfaces was calculated using nonequilibrium molecular dynamics (NEMD) simulations from a slab-like geometry based on Fourier law approach<sup>48</sup> and is also schematically depicted in Figure 3b. As seen from the figure, the outer edges of the elongated slab (1 nm) were fixed, while the adjacent 1.5 nm bins were employed as hot and cold thermostats, where a temperature rescaling algorithm was employed to keep the respective temperatures to 350 and 250 K. *NVE* ensemble was employed for nonthermostated regions. In order to keep the regions at their specified temperatures, energy was continuously added and taken off from the hot and cold regions, respectively. Our previous

studies on silicon and polymer composites have shown that thermal conductivity and interface thermal conductance prediction is not noticeably affected by choice of thermostats (Nose–Hoover, Berendsen, and temperature rescaling).<sup>49–51</sup>

By applying thermostats, a temperature gradient is established over time along the elongated slab direction, leading to a steady-state temperature profile. Furthermore, near the interface, a temperature discontinuity develops due to a mismatch between the vibrational properties of the two media. The temperature profile can then be calculated by dividing the slab into a predefined number of thin slabs with equal thickness (2 Å for our case) and calculating the temperature of each bin using the following equation.

$$T_i = \frac{1}{3N_i k_B} \sum_{k=1}^{N_i} m_k v_k^2 \quad (1)$$

where  $N_i$  is the number of atoms in the *i*th slab and  $m_k$  and  $v_k$  correspond to atomic mass and velocity of atom *k*, respectively. For the current study, each of the 2 Å bins contained  $\sim 500$  atoms. As an example, one such steady-state temperature profile for a representative case is shown in Supporting Information section S5 along with the calculation of temperature discontinuity,  $\Delta T$ . The interface thermal conductance was then calculated using the following equation.

$$\Lambda = \frac{Q}{A \Delta T} \quad (2)$$

where  $\Lambda$ , *A*, and *Q* respectively correspond to interface thermal conductance, cross-sectional area, and heat flux as estimated by the energy dumped into hot (taken out from cold) thermostats.<sup>52</sup> The heat flux calculation is further discussed in Supporting Information section S6 using the cumulative energy dumped (or taken out) estimates for a representative case. For all cases, initial simulations were run for about 1 ns in order to achieve steady-state. Following that, simulations were further run for 4 ns for data collection for temperature gradient and heat flux calculations.

### 3. RESULTS AND DISCUSSION

Next, we present and discuss the effect of various parameters on thermal transport across the carbon-fiber/matrix interface. Here, unlike the previous section, we have not divided the discussion between carbon-surface and interface models but have attempted to present the effect of different build models in a more coherent way. We wrap up this section with a few comments on possible modifications to interface thermal conductance due to matrix cross-linking, which is not investigated in this study.

**3.1. Effect of Functionalization.** We start this section with discussing the effect of surface functionalization density on interface thermal conductance as shown in Figure 4. The figure clearly shows that the interface functionalization significantly increases the thermal conductance across the interface with respect to unfunctionalized interface ( $C_{90}$ ), increasing up to 4-fold for surface functionalization density of 0.55 molecules/nm<sup>2</sup>. The increasing trend and relative increase is in excellent agreement with the previous literature.<sup>18,20,23,24,27,29,30</sup> Here, the increase in thermal conductance is attributed to the interface bonding which provides additional pathways via covalent bonds, in addition to van der Waals interactions, for better thermal energy transport across the interface.

The surface functionalization is expected to occur via “end atoms” of polymeric fragments, whose volumetric concentration for oligomeric or polymeric chains is expected to be  $\ll 1$  nm<sup>3</sup>. In this context, we believe that the largest modeled surface functionalization density of 0.55 molecules/nm<sup>2</sup> is noticeably higher than experimentally achievable surface functionalization densities of attaching amorphous polymeric fragments on

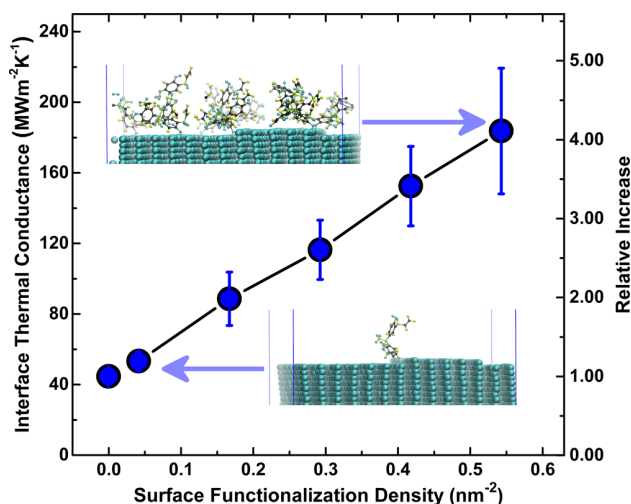


**Figure 4.** Plot of interface thermal conductance as a function of surface functionalization density for studied functionalized cases. Two schematics of functionalized interface are also shown. Relative increase in conductance with respect to unfunctionalized  $C_{90}$  case is plotted as well.

carbon-fiber surfaces. Thus, current study provides an estimate of conductance enhancement bounds, achievable in realistic experimental conditions.

**3.2. Effect of Interface Roughness.** Generally, when dealing with rough interfaces, there is an overlap region where both components (carbon-fiber surface and matrix in our case) are present. Estimating thermal transport across such cases introduces the concept of “interphase” as the definition of “interface” or a distinct “plane” becomes blurry. Such behavior is depicted in Figure 5 for one of our model systems which shows the presence of both graphitic carbon and matrix overlap over a 3 nm region. In principle, one could define various “planes” or “interfaces” (as depicted in Figure 5), but such a

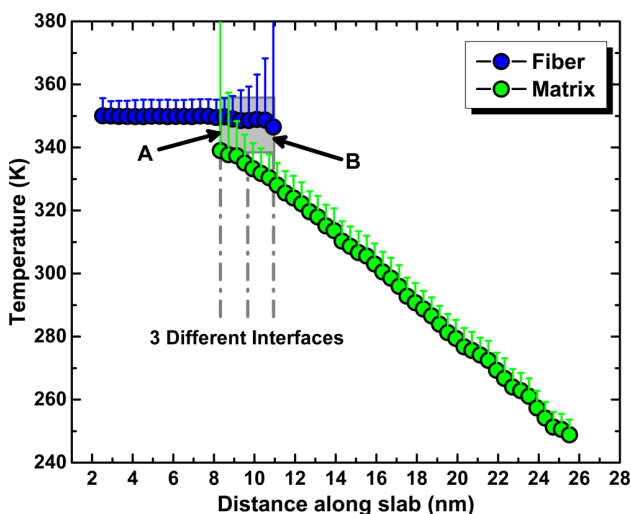


**Figure 5.** Plot of steady-state temperature profile across rough interfaces along the slab direction. Three different interfaces are depicted within the rough interphase with dashed–dotted lines and are discussed in Supporting Information section S7. “A” and “B” denote opposite boundaries of the interphase. Only the upper halves of the error bars are shown for clarity purposes.

definition is arbitrary and leads to different values of interface thermal conductance based on the chosen interface (please see Supporting Information section S7 for further discussion). In order to avoid that ambiguity, we calculate interphase thermal conductance between points A and B, which denote the boundaries of the interphase region, as shown in Figure 5. The resulting interphase thermal conductance is plotted in Figure 6

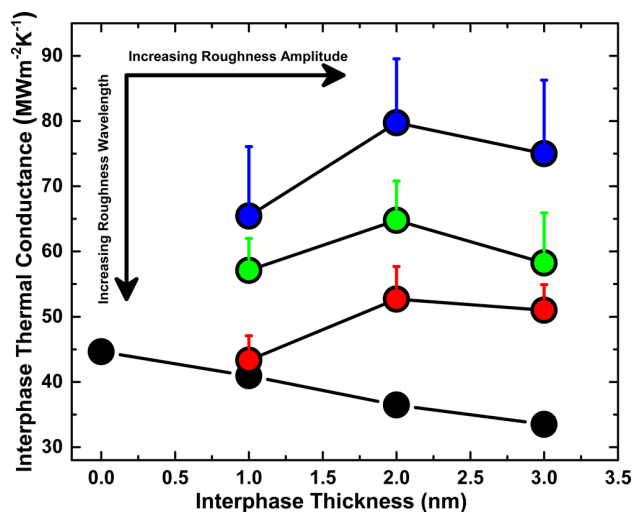


**Figure 6.** Plot of interphase thermal conductance as a function of interphase thickness for three different roughness wavelengths of 5 (red), 2.5 (green), and 1.7 nm (blue). Black data points show “effective” thermal conductance across the same width for the flat  $C_{90}$  graphitic model. Only the upper halves of the error bars are shown for clarity purposes.

as a function of interphase width for three different wavelength periodicities and compares the modulation with respect to the thermal conductance of a flat interface ( $C_{90}$ ) for similar width (black data points).

For a constant interface width, the data show that the thermal conductance increases with decreasing periodicity. This increase can be attributed to an increase in carbon-fiber surface area which interacts with the matrix, leading to enhanced thermal conduction. For modeled interface widths, our simulations show a relative increase by a factor of 2–3 in thermal conductance with respect to their flat counterpart. For a constant wavelength, however, the data show that the interphase thermal conductance does not alter significantly and does not show a clear trend with increase in interphase width (or roughness amplitude). While increase in interphase width increases total thermal energy exchange (increase in surface area), it also increases the width over which the thermal conductance is estimated. These two features compete against each other in interphase thermal conductance estimation (increase in both numerator and denominator), leading to an overall minor variation in Figure 6. Nevertheless, it is important to note the relative increase in thermal conductance with respect to flat interfaces as a function of roughness amplitude as well as periodicity of roughness undulation.

### 3.3. Effect of CNT Incorporation at the Interface.

Similar to roughness, incorporation of CNTs at the carbon-fiber/matrix interface reignites the conductance discussion in terms of interphase. In this context, Figure 7 (inset) shows the estimated thermal conductance across the interphase as depicted by points A (fused junction) and B (nanotube cap).



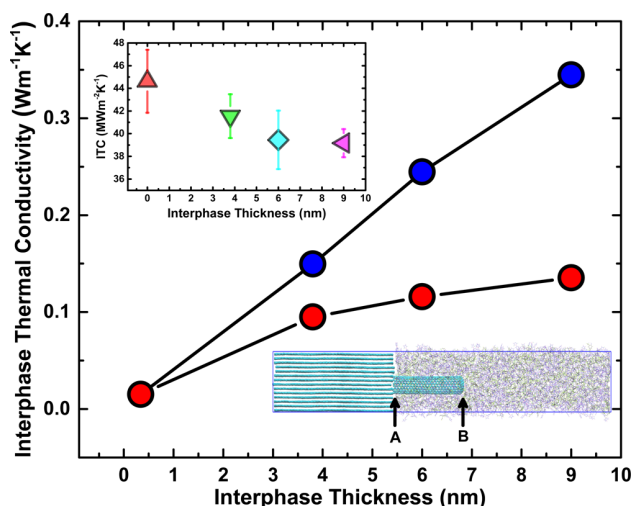


**Figure 7.** Plot of interphase thermal conductivity as a function of interphase thickness (or CNT length). Blue data points show thermal conductivity of CNT-bonded interphases for different widths while red data points show “effective” thermal conductivity for the same widths for the flat  $C_{90}$  graphitic model with no CNTs. Inset: Plot of interphase thermal conductance as a function of interphase thickness for four different studied cases: flat interface (red); 3.8 nm CNT (green); 6 nm CNT (cyan); 9 nm CNT (pink).

Over a length of 9 nm, only a slight decrease in conductance is observed which is indicative of a more conductive interphase and is attributed to an increase in effective surface area for thermal energy transport.<sup>53</sup> The ramifications of this slight decrease are further substantiated in Figure 7 (main) which plots the interphase thermal conductivity as a function of interphase thickness. Also shown in the same plot is the estimated thermal conductivity of the same region (including the interface) if only the matrix were present. In addition to the increase in effective thermal conductivity of the interface with CNT length, the figure shows that this increase is also noticeable (up to 2-fold for modeled cases) with respect to the effective thermal conductivity of the pure matrix in that region. Based on the observed trends, it is expected that higher surface density and a longer length of covalently bonded CNTs at carbon-fiber surfaces can greatly enhance thermal transport properties across the fiber/matrix interface.

**3.4. Effect of Fiber Surface Morphology Thickness.** For high thermal conductivity materials, such as CNTs and graphite, it has repeatedly been shown that the system size of MD simulations affects the prediction of thermal transport properties because of their extremely large phonon mean free paths.<sup>46,49,54,55</sup> For our system, modeled graphitic surfaces of 10 nm also present a similar scenario. In order to investigate if the thickness of graphitic surface models (equivalent to mimicking the thickness of carbon-fiber surface morphology) has a consequential effect on interfacial thermal transport, we modeled several graphitic lengths for the  $C_{33}$  model system. In this context, Figure 8 shows the calculated thermal conductance values for different studied lengths ranging from ~5 to ~17 nm. The figure clearly shows that interface thermal conductance does increase significantly with increasing graphitic length. The primary reason behind such an increase is attributed to the inclusion of longer wavelength phonons within the graphitic model with increasing thickness, which can couple with the BMI matrix when they propagate to the interface.

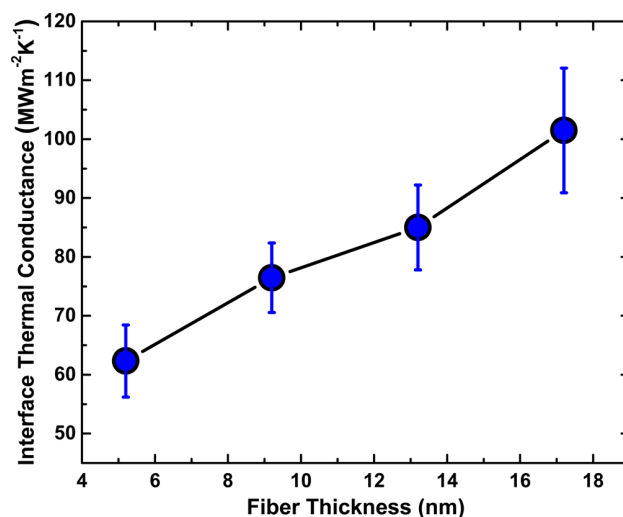


**Figure 8.** Plot of interface thermal conductance as a function of effective fiber thickness for the  $C_{33}$  graphitic model case.

While the simulations were performed for 10 s of nm of graphitic thickness, the conductance values are expected to saturate eventually, when fiber dimensions exceed characteristics mean free path of in-plane phonons in graphite ( $\sim \mu\text{m}$ ).

**3.5. Effect of Graphitic Orientation.** Next, we discuss how the orientation of graphitic layers can modulate the thermal energy transport across the interphase. In this context, Figure 9 plots and shows the monotonic decrease of the

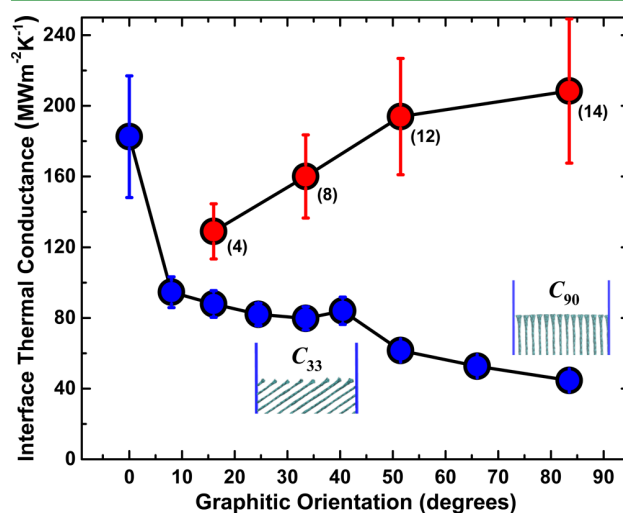


**Figure 9.** Plot of interface thermal conductance as a function of graphitic orientation for unsaturated (blue) and saturated (red) interface bonds. The numbers next to the red data points show the number of graphene layer edges at the interface. As the graphitic orientation angle increases, so do the number of graphene layer edges. Two schematics for  $C_{33}$  and  $C_{90}$  graphitic models demonstrate the said increase in graphene layer edges.

estimated interface thermal conductance as a function of graphitic orientation angle,  $\theta$ . For clearer interpretation, we separate our discussion into  $0^\circ$  ( $C_0$ ) and non- $0^\circ$  ( $C_8$ – $C_{90}$ ) graphitic orientation cases. The reason being that for  $C_8$ – $C_{90}$  cases, graphene layers interacting with the matrix are directly connected to the hot thermostat, while for the  $C_0$  case, energy



has to propagate from the hot thermostated graphene layers to the end-graphene surface directly interacting with the matrix through in-between mediating graphene layers via van der Waals interactions (See Supporting Information section S8 for better pictorial visualization).

First, the exceptionally large value ( $183 \text{ MWm}^{-2} \text{ K}^{-1}$ ) of interface thermal conductance for case  $C_0$  is attributed to soft low-frequency modes propagating across graphene layers. These low-frequency modes can couple to a greater extent with the low-frequency vibrational modes of the matrix leading to enhanced thermal transport. Recent experiments on radial thermal transport across large multiwall CNTs have suggested the phonon mean free path across the out-of-plane direction of graphite to be  $>100 \text{ nm}$ .<sup>56</sup> In view of that, it is expected that the predicted conductance, based on  $10 \text{ nm}$  graphitic thickness, is expected to increase notably for much thicker flat graphitic ( $\sim 0^\circ$ ) carbon-fiber surfaces.

On the other extreme, thermal conductance for perpendicular orientation ( $C_{90}$ ) was observed to be  $\sim 5$ -fold lower ( $\sim 40 \text{ MWm}^{-2} \text{ K}^{-1}$ ) for the same model thickness of  $\sim 10 \text{ nm}$ . The low value is attributed to the small thickness ( $10 \text{ nm}$ ) as well as relatively stiff (high-frequency) propagating modes. When such phonons reach the interface, the probability of their reflection at the interface is greater than soft out-of-plane modes of graphite (in the  $0^\circ$  case), leading to a lower value of thermal conductance. Figure 9 also shows that interface thermal conductance is increasing with decreasing  $\theta$  for  $C_8$ – $C_{90}$  cases. This increase in conductance is attributed to an increase in the “effective length” of the graphite ( $L/\sin(\theta)$ ). Please see Supporting Information section S8 for visualization of the “effective length”. In these cases, phonons predominantly propagate along graphitic planes (in-plane modes) due to the extremely high thermal anisotropy of graphite ( $>100$  times) before reaching graphene edges, which eventually dictate the thermal transport.

**3.6. Effect of Interface Bond Saturation.** Figure 9 also shows the interface thermal conductance for four different graphitic orientations ( $C_{16}$ ,  $C_{33}$ ,  $C_{55}$ , and  $C_{90}$ ) where we saturated the edge carbon atoms by hydrogen atoms (H atoms). First, for constant graphitic orientation, the figure shows that saturated models always show higher thermal conductance than their unsaturated counterpart. The added H atoms contribute toward enhancing van der Waals interactions, while taking minimal volume (small  $\sigma$  and short C–H bond length), resulting in a relative increase of conductance.

On the contrary, unlike unsaturated cases, we see an increase in conductance with increase in graphitic orientation angle. We attribute this increasing trend to the increasing number density of interacting atoms (H atoms) with the matrix near the interface. As noted in the figure, the number of interacting graphene layers' edges increase with an increase in orientation angle, which in turn also increases the surface number density of H atoms, leading to enhanced van der Waals interactions (the interactions scale as  $N^2$ ,  $N$  being the number of interacting atoms). Despite the shorter effective length for large  $\theta$  models, enhanced interactions dominate and lead to an increase in conductance, also increasing the respective gap between saturated and unsaturated cases. We should note that while this is a somewhat hypothetical set of simulations, it does provide important information on how the number density of surface interacting atoms can modulate interface thermal conductance.

**3.7. Effect of Graphitic Defects.** Similar to graphitic orientation, the defects within carbon-fiber surface models can also affect interface thermal conductance as shown in Figure 10.

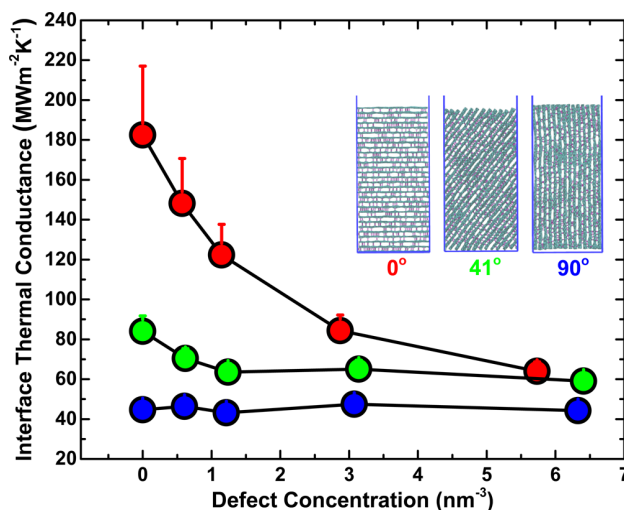


**Figure 10.** Plot of interface thermal conductance as a function of  $\text{sp}^3$  defect concentrations for three different studied graphitic models,  $C_0$ ,  $C_{41}$ , and  $C_{90}$ . Schematics of these models for  $\sim 3\%$  defect concentrations are shown for further visual clarity. Furthermore, only the upper halves of the error bars are shown for clarity purposes.

The figure shows significant decrease ( $\sim 60\%$ ) in conductance for the  $C_0$  model with respect to modeled defect concentrations, while the decrease is relatively minor for  $C_{41}$  ( $\sim 20\%$ ) and  $C_{90}$  ( $\sim 0\%$ ) graphitic models. For the former, the notable decrease is attributed to increased perturbation in coherency of out-of-plane modes with increased defect concentrations as these defects ( $\text{sp}^3$ ) significantly reduce the phonon mean free path along the out-of-plane direction. However, for latter models ( $C_{41}$  and  $C_{90}$ ), the minor or negligible decrease is associated with the observation that, in these cases,  $\text{sp}^3$  bonds are orientated perpendicular to the dominant thermal transport direction (along graphene direction), minimally perturbing the energy carrying propagating phonons.

**3.8. Effect of Matrix Cross-Linking on Interface Thermal Conductance.** Similar to intrinsic fiber properties and interface features, it is expected that matrix properties (cured vs uncured) would also affect interface thermal conductance. However, this parameter space, i.e., effect of curing, is not explored in this study. Unlike modeling of an epoxy-based matrix curing process, which often requires modeling a single amine–epoxy reaction,<sup>57</sup> modeling the curing process of BMI-5292 resin involves five separate reactions (ene reaction, maleimide homopolymerization, alternating maleimide–adduct co-polymerization, ene adduct homopolymerization via propenyl groups, and dehydration/etherification reaction) leading to a much more complex curing pathway.<sup>31,32</sup> The framework for the curing process involving all five reactions is currently being formulated using atomistic molecular dynamics simulations and would be reported in future studies. Nevertheless, based on our previous studies on interface thermal conductance across cured epoxy matrix and carbon nanotubes, we foresee that the curing process is expected to enhance the thermal conductance up to  $20\%$ .<sup>24</sup>

## 4. CONCLUSIONS

In a single comprehensive investigation, this study explores a series of carbon-fiber bulk and interface parameters in order to gauge their importance toward engineering thermal transport across carbon-fiber/matrix interfaces. Based on atomistic molecular dynamics simulations, it is suggested that the long-range graphitic nature of carbon-fibers near the interface, a higher number density of surface atoms, a larger degree of functionalization, molecular surface roughness, and incorporation of high-conductivity fillers (such as CNTs) can significantly augment the interface thermal conductance across the interface. On the contrary, defects within the carbon fiber, low number density of interacting atoms, and less effective area of interaction due to voids (not studied here) can lead to a noticeable decrease in thermal conductance. In summary, the presented results provide key insights into realistic bounds (degree of variation) to the interface thermal conductance values at fiber/matrix interfaces as a function of many different surface-carbon morphologies. In addition, we believe that this parametric study incorporating various key parameters has broader ramifications on modulating thermal conductance, not only across carbon-fiber/matrix interfaces but also in different types of thermal interface materials as well as different nanoscopic devices where thermal dissipation plays a crucial role in device performance.

## ■ ASSOCIATED CONTENT

### ■ Supporting Information

The Supporting Information is available free of charge on the ACS Publications website at DOI: 10.1021/acsami.5b08591.

Detailed specifics on the generation of different carbon-surface models, estimation of the heat flux and the temperature drop across the interface, consequences of using an arbitrary interface for interface thermal conductance calculations for rough interfaces, and visual representation of differences between  $C_0$  and  $C_8$ – $C_{90}$  graphitic orientation cases with respect to applied thermostats (PDF)

## ■ AUTHOR INFORMATION

### Corresponding Authors

\*(V.V.) E-mail: [vikas.varshney@wpafb.af.mil](mailto:vikas.varshney@wpafb.af.mil).

\*(J.W.B.) E-mail: [jeffery.baur@us.af.mil](mailto:jeffery.baur@us.af.mil).

### Notes

The authors declare no competing financial interest.

## ■ ACKNOWLEDGMENTS

We acknowledge the U.S. Air Force Office of Scientific Research (AFOSR) for financial support (Grant No. 13RXCOR; Program Manager, Dr. B. L. “Les” Lee) and the Department of Defense Supercomputing Research Center (AFRL-DSRC and ERDC-DSRC) for computational resources to carry out the simulations.

## ■ REFERENCES

- (1) El-Aneel, A.; Cohen, A.; Banoub, J. Mass Spectrometry, Review of the Basics: Electrospray, MALDI, and Commonly Used Mass Analyzers. *Appl. Spectrosc. Rev.* **2009**, *44*, 210–230.
- (2) Zhang, Y.-L.; Chen, Q.-D.; Xia, H.; Sun, H.-B. Designable 3D Nanofabrication by Femtosecond Laser Direct Writing. *Nano Today* **2010**, *5*, 435–448.

- (3) Kabashin, A.; Delaporte, P.; Pereira, A.; Grojo, D.; Torres, R.; Sarnet, T.; Sentis, M. Nanofabrication with Pulsed Lasers. *Nanoscale Res. Lett.* **2010**, *5*, 454–463.
- (4) Conforti, P. F.; Prasad, M.; Garrison, B. J. Elucidating the Thermal, Chemical, and Mechanical Mechanisms of Ultraviolet Ablation in Poly(methyl methacrylate) via Molecular Dynamics Simulations. *Acc. Chem. Res.* **2008**, *41*, 915–924.
- (5) Lippert, T.; Dickinson, J. T. Chemical and Spectroscopic Aspects of Polymer Ablation: Special Features and Novel Directions. *Chem. Rev.* **2003**, *103*, 453–86.
- (6) Han, Z.; Fina, A. Thermal Conductivity of Carbon Nanotubes and Their Polymer Nanocomposites: A Review. *Prog. Polym. Sci.* **2011**, *36*, 914–944.
- (7) McNamara, A. J.; Joshi, Y.; Zhang, Z. M. Characterization of Nanostructured Thermal Interface Materials – A Review. *Int. J. Therm. Sci.* **2012**, *62*, 2–11.
- (8) Hung, M. T.; Choi, O.; Ju, Y. S.; Hahn, H. T. Heat Conduction in Graphite-Nanoplatelet-Reinforced Polymer Nanocomposites. *Appl. Phys. Lett.* **2006**, *89*, 023117.
- (9) Huang, J.; Gao, M.; Pan, T.; Zhang, Y.; Lin, Y. Effective Thermal Conductivity of Epoxy Matrix Filled with Poly(ethyleneimine) Functionalized Carbon Nanotubes. *Compos. Sci. Technol.* **2014**, *95*, 16–20.
- (10) Zhang, P.; Li, Q.; Xuan, Y. Thermal Contact Resistance of Epoxy Composites Incorporated with Nano-Copper Particles and the Multi-Walled Carbon Nanotubes. *Composites, Part A* **2014**, *57*, 1–7.
- (11) Gharagozloo-Hubmann, K.; Boden, A.; Czempel, G. J. F.; Firkowska, I.; Reich, S. Filler Geometry and Interface Resistance of Carbon Nanofibres: Key Parameters in Thermally Conductive Polymer Composites. *Appl. Phys. Lett.* **2013**, *102*, 213103.
- (12) Lizundia, E.; Oleaga, A.; Salazar, A.; Sarasua, J. R. Nano- and Microstructural Effects on Thermal Properties of Poly (L-lactide)/ Multi-Wall Carbon Nanotube Composites. *Polymer* **2012**, *53*, 2412–2421.
- (13) Yu, J.; Tonpheng, B.; Gröbner, G.; Andersson, O. Thermal Properties and Transition Studies of Multi-Wall Carbon Nanotube/ Nylon-6 Composites. *Carbon* **2011**, *49*, 4858–4866.
- (14) Roy, A. K.; Farmer, B. L.; Varshney, V.; Sih, S.; Lee, J.; Ganguli, S. Importance of Interfaces in Governing Thermal Transport in Composite Materials: Modeling and Experimental Perspectives. *ACS Appl. Mater. Interfaces* **2012**, *4*, 545–563.
- (15) Frenkel, D.; Smit, B. *Understanding Molecular Simulation: From Algorithms to Applications*. Academic Press: London, 2001; Vol. 1.
- (16) Huxtable, S. T.; Cahill, D. G.; Shenogin, S.; Xue, L.; Ozisik, R.; Barone, P.; Usrey, M.; Strano, M. S.; Siddons, G.; Shim, M.; Keblinski, P. Interfacial Heat Flow in Carbon Nanotube Suspensions. *Nat. Mater.* **2003**, *2*, 731–734.
- (17) Shenogin, S.; Xue, L.; Ozisik, R.; Keblinski, P.; Cahill, D. G. Role of Thermal Boundary Resistance on the Heat Flow in Carbon-Nanotube Composites. *J. Appl. Phys.* **2004**, *95*, 8136–8144.
- (18) Shenogin, S.; Bodapati, A.; Xue, L.; Ozisik, R.; Keblinski, P. Effect of Chemical Functionalization on Thermal Transport of Carbon Nanotube Composites. *Appl. Phys. Lett.* **2004**, *85*, 2229–2232.
- (19) Unnikrishnan, V.; Reddy, J.; Banerjee, D.; Rostam-Abadi, F. Thermal Characteristics of Defective Carbon Nanotube-Polymer Nanocomposites. *Interact. Multiscale Mech.* **2008**, *1*, 397–409.
- (20) Konatham, D.; Striolo, A. Thermal Boundary Resistance at the Graphene-Oil Interface. *Appl. Phys. Lett.* **2009**, *95*, 163105.
- (21) Luo, T.; Lloyd, J. R. Enhancement of Thermal Energy Transport across Graphene/Graphite and Polymer Interfaces: A Molecular Dynamics Study. *Adv. Funct. Mater.* **2012**, *22*, 2495–2502.
- (22) Hida, S.; Hori, T.; Shiga, T.; Elliott, J.; Shiomi, J. Thermal Resistance and Phonon Scattering at the Interface between Carbon Nanotube and Amorphous Polyethylene. *Int. J. Heat Mass Transfer* **2013**, *67*, 1024–1029.
- (23) Lin, S.; Buehler, M. J. The Effect of Non-Covalent Functionalization on the Thermal Conductance of Graphene/Organic Interfaces. *Nanotechnology* **2013**, *24*, 165702.

- (24) Varshney, V.; Roy, A. K.; Michalak, T. J.; Lee, J.; Farmer, B. L. Effect of Curing and Functionalization on the Interface Thermal Conductance in Carbon Nanotube–Epoxy Composites. *JOM* **2013**, *65*, 140–146.
- (25) Merabia, S.; Termentzidis, K. Thermal Boundary Conductance across Rough Interfaces Probed by Molecular Dynamics. *Phys. Rev. B: Condens. Matter Mater. Phys.* **2014**, *89*, 054309.
- (26) Kuang, Y.; Huang, B. Effects of Covalent Functionalization on the Thermal Transport in Carbon Nanotube/Polymer Composites: A Multi-Scale Investigation. *Polymer* **2015**, *56*, S63–S71.
- (27) Wang, M.; Hu, N.; Zhou, L.; Yan, C. Enhanced Interfacial Thermal Transport across Graphene–Polymer Interfaces by Grafting Polymer Chains. *Carbon* **2015**, *85*, 414–421.
- (28) Liu, Y.; Hu, C.; Huang, J.; Sumpter, B. G.; Qiao, R. Tuning Interfacial Thermal Conductance of Graphene Embedded in Soft Materials by Vacancy Defects. *J. Chem. Phys.* **2015**, *142*, 244703.
- (29) Ni, Y.; Han, H.; Volz, S.; Dumitrică, T. Nanoscale Azide Polymer Functionalization: A Robust Solution for Suppressing the Carbon Nanotube–Polymer Matrix Thermal Interface Resistance. *J. Phys. Chem. C* **2015**, *119*, 12193–12198.
- (30) Wang, Y.; Zhan, H. F.; Xiang, Y.; Yang, C.; Wang, C. M.; Zhang, Y. Y. Effect of Covalent Functionalization on Thermal Transport across Graphene–Polymer Interfaces. *J. Phys. Chem. C* **2015**, *119*, 12731–12738.
- (31) Rozenberg, B. A.; Boiko, G. N.; Morgan, R. J.; Shin, E. E. The Cure Mechanism of the 4,4'-(N,N'-Bismaleimide)diphenylmethane-2,2'-diallylbisphenol A System. *Polym. Sci., Ser. A* **2001**, *43*, 630–645.
- (32) Rozenberg, B. A.; Dzhevadyan, E. A.; Morgan, R.; Shin, E. High-Performance Bismaleimide Matrices: Cure Kinetics and Mechanism. *Polym. Adv. Technol.* **2002**, *13*, 837–844.
- (33) Cho, D.; Drzal, L. T. Effect of Thermal Cure on the Fluorescence of Matrimid 5292 Bismaleimide Resin. *J. Mater. Sci. Lett.* **2003**, *22*, 459–461.
- (34) Lincoln, J. E.; Morgan, R. J.; Shin, E. E. Moisture Absorption-Network Structure Correlations in BMPM/DABPA Bismaleimide Composite Matrices. *J. Adv. Mater.* **2000**, *32*, 24–34.
- (35) *Materials Studio*; Accelrys Software: San Diego, CA, USA, 2012.
- (36) Dauber-Osguthorpe, P.; Roberts, V. A.; Osguthorpe, D. J.; Wolff, J.; Genest, M.; Hagler, A. T. Structure and Energetics of Ligand Binding to Proteins: Escherichia Coli Dihydrofolate Reductase-Trimethoprim, a Drug-Receptor System. *Proteins: Struct., Funct., Genet.* **1988**, *4*, 31–47.
- (37) Sun, H.; Mumby, S. J.; Maple, J. R.; Hagler, A. T. An Ab Initio CFF93 All-Atom Force Field for Polycarbonates. *J. Am. Chem. Soc.* **1994**, *116*, 2978–2987.
- (38) Wang, J.; Wolf, R. M.; Caldwell, J. W.; Kollman, P. A.; Case, D. A. Development and Testing of a General Amber Force Field. *J. Comput. Chem.* **2004**, *25*, 1157–1174.
- (39) Cornell, W. D.; Cieplak, P.; Bayly, C. I.; Gould, I. R.; Merz, K. M.; Ferguson, D. M.; Spellmeyer, D. C.; Fox, T.; Caldwell, J. W.; Kollman, P. A. A Second Generation Force Field for the Simulation of Proteins, Nucleic Acids, and Organic Molecules. *J. Am. Chem. Soc.* **1995**, *117*, 5179–5197.
- (40) Frisch, M. J.; Trucks, G. W.; Schlegel, H. B.; Scuseria, G. E.; Robb, M. A.; Cheeseman, J. R.; Scalmani, G.; Barone, V.; Mennucci, B.; Petersson, G. A.; Nakatsuji, H.; Caricato, M.; Li, X.; Hratchian, H. P.; Izmaylov, A. F.; Bloino, J.; Zheng, G.; Sonnenberg, J. L.; Hada, M.; Ehara, M.; Toyota, K.; Fukuda, R.; Hasegawa, J.; Ishida, M.; Nakajima, T.; Honda, Y.; Kitao, O.; Nakai, H.; Vreven, T.; Montgomery, J. A., Jr.; Peralta, J. E.; Ogliaro, F. O.; Bearpark, M. J.; Heyd, J.; Brothers, E. N.; Kudin, K. N.; Staroverov, V. N.; Kobayashi, R.; Normand, J.; Raghavachari, K.; Rendell, A. P.; Burant, J. C.; Iyengar, S. S.; Tomasi, J.; Cossi, M.; Rega, N.; Millam, N. J.; Klene, M.; Knox, J. E.; Cross, J. B.; Bakken, V.; Adamo, C.; Jaramillo, J.; Gomperts, R.; Stratmann, R. E.; Yazyev, O.; Austin, A. J.; Cammi, R.; Pomelli, C.; Ochterski, J. W.; Martin, R. L.; Morokuma, K.; Zakrzewski, V. G.; Voth, G. A.; Salvador, P.; Dannenberg, J. J.; Dapprich, S.; Daniels, A. D.; Farkas, A. d. n.; Foresman, J. B.; Ortiz, J. V.; Cioslowski, J.; Fox, D. J. *Gaussian 09*, Revision A.02; Gaussian: Wallingford, CT, USA, 2009.
- (41) Dupradeau, F.-Y.; Pigache, A.; Zaffran, T.; Savineau, C.; Lelong, R.; Grivel, N.; Lelong, D.; Rosanski, W.; Cieplak, P. The R.E.D. Tools: Advances in RESP and ESP Charge Derivation and Force Field Library Building. *Phys. Chem. Chem. Phys.* **2010**, *12*, 7821–7839.
- (42) Plimpton, S. Fast Parallel Algorithms for Short-Range Molecular Dynamics. *J. Comput. Phys.* **1995**, *117*, 1–19.
- (43) Varshney, V.; Roy, A. K.; Baur, J. Molecular Modeling of BMI Matrix, Its Thermo-Physical Properties, and Its Interface with Amorphous Carbon Fiber. In *Proceedings of the American Society for Composites 2014—Twenty-ninth Technical Conference on Composite Materials*, San Diego, CA, USA, Sep. 17, 2014; Kim, K., Whisler, D., Chen, Z. M., Bisagni, C., Kawai, M., Krueger, R., Eds.; DEStech Publications: San Diego, CA, USA, 2014.
- (44) Loh, G. C.; Baillargeat, D. Graphitization of Amorphous Carbon and Its Transformation Pathways. *J. Appl. Phys.* **2013**, *114*, 033534.
- (45) We tried different approaches using AIREBO and Tersoff potentials to create graphitic order from amorphous carbon as discussed by ref 44 but were not successful in repeatedly reproducing the graphitic order. Hence we chose to add defects in pristine graphite.
- (46) Pop, E.; Varshney, V.; Roy, A. K. Thermal Properties of Graphene: Fundamentals and Applications. *MRS Bull.* **2012**, *37*, 1273–1281.
- (47) Robinson, M.; Marks, N. A. NanoCap: A Framework for Generating Capped Carbon Nanotubes and Fullerenes. *Comput. Phys. Commun.* **2014**, *185*, 2519–2526.
- (48) Anderson, C. V. D. R.; Tamma, K. K. An Overview of Advances in Heat Conduction Models and Approaches for Prediction of Thermal Conductivity in Thin Dielectric Films. *Int. J. Numer. Methods Heat Fluid Flow* **2004**, *14*, 12–65.
- (49) Varshney, V.; Roy, A. K.; Froudakis, G.; Farmer, B. L. Molecular Dynamics Simulations of Thermal Transport in Porous Nanotube Network Structures. *Nanoscale* **2011**, *3*, 3679–3684.
- (50) Varshney, V.; Roy, A. K.; Dudis, D. S.; Lee, J.; Farmer, B. L. A Novel Nano-Configuration for Thermoelectrics: Helicity Induced Thermal Conductivity Reduction in Nanowires. *Nanoscale* **2012**, *4*, S009–S016.
- (51) Varshney, V.; Lee, J.; Farmer, B. L.; Voevodin, A. A.; Roy, A. K. Modeling of Cross-Plane Interface Thermal Conductance between Graphene Nano-Ribbons. *2D Mater.* **2014**, *1*, 025005.
- (52) After steady-state is reached, net heat flux is calculated by taking the slope of the cumulative energy output dumped by LAMMPS as discussed in [Supporting Information](#) section S6.
- (53) For a constant thermal conductivity interphase, thermal conductance decreases inversely with thickness. The observation that the decrease in thermal conductance is minimal over an ~10-fold increase in interphase thickness is indicative of an increasing thermally conductive interphase.
- (54) Marconnet, A. M.; Panzer, M. A.; Goodson, K. E. Thermal Conduction Phenomena in Carbon Nanotubes and Related Nano-structured Materials. *Rev. Mod. Phys.* **2013**, *85*, 1295–1326.
- (55) Varshney, V.; Patnaik, S. S.; Roy, A. K.; Froudakis, G.; Farmer, B. L. Modeling of Thermal Transport in Pillared-Graphene Architectures. *ACS Nano* **2010**, *4*, 1153–1161.
- (56) Yang, J.; Shen, M.; Yang, Y.; Evans, W. J.; Wei, Z.; Chen, W.; Zinn, A. A.; Chen, Y.; Prasher, R.; Xu, T. T.; Koblinski, P.; Li, D. Phonon Transport through Point Contacts between Graphitic Nanomaterials. *Phys. Rev. Lett.* **2014**, *112*, 205901.
- (57) Varshney, V.; Patnaik, S. S.; Roy, A. K.; Farmer, B. L. A Molecular Dynamics Study of Epoxy-Based Networks: Cross-Linking Procedure and Prediction of Molecular and Material Properties. *Macromolecules* **2008**, *41*, 6837–6842.

## **Supporting Information**

### **Modeling the Role of Bulk and Surface Characteristics of Carbon Fiber on Thermal Conductance across the Carbon-Fiber/Matrix Interface**

Vikas Varshney<sup>1,2</sup>, Ajit K. Roy<sup>1</sup>, and Jeffery W. Baur<sup>1</sup>

<sup>1</sup>Materials and Manufacturing Directorate, Air Force Research Laboratory, Wright-Patterson Air Force Base, Ohio 45433, USA

<sup>2</sup>Universal Technology Corporation, Dayton Ohio 45432, USA

#### **Corresponding Author(s) email addresses**

Vikas Varshney: [vikas.varshney@wpafb.af.mil](mailto:vikas.varshney@wpafb.af.mil)

Jeff Baur: [Jeffery.baur@us.af.mil](mailto:Jeffery.baur@us.af.mil)



## S1: Generation of carbon surface models with different graphitic orientations

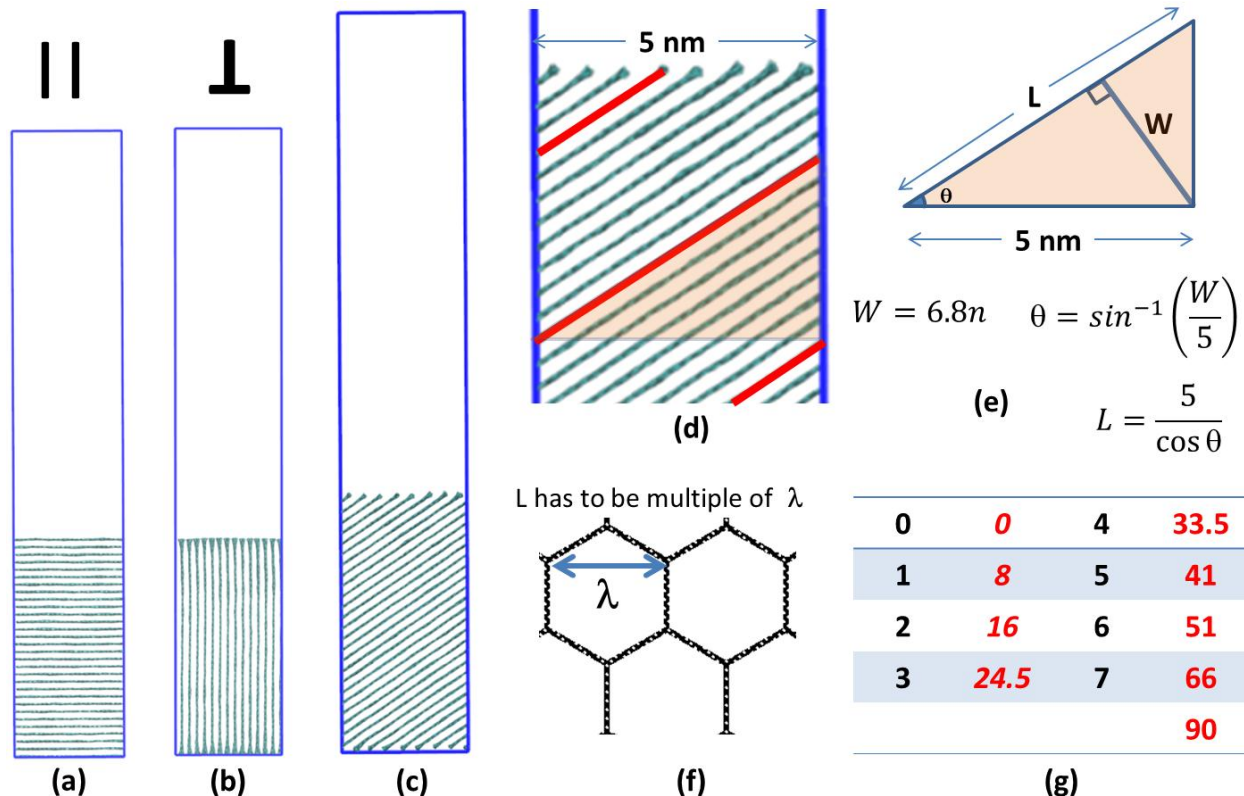


**Figure S1:** Carbon surface models with (a) 0° graphitic orientation; (b) 90° graphitic orientation; and (c) 33° graphitic orientation; (d) close-up view highlighting periodic nature of the tilted graphitic layer as wrapped red lines; (e and f) mathematical constraints applicable for generating periodic structures with non-0° and non-90° graphitic orientations; and (g) final graphitic tilt angles generated from the mathematical equations.

To investigate the effect of graphitic orientation on the interface thermal conductance, several models were created having different graphitic orientations with respect to the interface plane (horizontal plane in **Figure S1**). It is relatively easier to create parallel and perpendicular orientations of the graphitic periodic crystal, as shown in **Figures S1a** and **S1b** using graphitic unit cell. However, creating a ‘periodic structure’ with any other graphitic orientation (as shown in **Figure S1c**) is not trivial and certain constraints need to be satisfied towards their generation. These constraints are shown in **Figures S1d-S1f** and are discussed below.

Graphite is periodic along zigzag and armchair directions with periodic lengths of 2.46 and 4.26 Å, respectively. Towards the generation of graphitic orientations (as shown in **Figure S1c**), we chose to have armchair direction along the Y-axis (going into the plane) while the zigzag direction makes certain angle with the X-axis (horizontal axis in the plane). So, **Figure S1a** has the orientation angle of 0° while **Figure S1b** has the orientation angle of 90° with zigzag direction being horizontal and vertical (in plane of paper), respectively. We call them  $C_0$  and  $C_{90}$  systems respectively.

First, along y-direction, 12 periodic cells (along armchair) were used, rendering the y-dimension of ~ 5.1 nm. In addition, x-dimension length was set to be 5 nm approximately.

One constraint of creating non-0° and non-90° graphitic orientations is that since individual graphene layers are periodic, one graphene layer appears as several graphene layers (separated by a certain distance) when wrapped across the periodic box. Such wrapping behavior is shown in **Figure S1d** (red diagonal lines which are indicative of a single graphene layer wrapped around the periodic boundary). Another constraint that one might have is the AB stacking geometry of graphene layers within graphite. When we take both constraints into account, it can be realized that eventual graphitic orientation angles will be set by certain trigonometric equations and it is not possible to have any angle if we constrain X-dimension to be ~5 nm. These trigonometric equations are shown in **Figure S1e**.

Looking at the triangle in **Figure S1e** and setting its horizontal length to be 5 nm, angle  $\theta$  will be decided by how many different graphitic layers we have in between before the same layer repeats itself (i.e., layers between red lines).  $W$ , width perpendicular to the graphene plane will be given by  $0.68n$  for AB type of stacking, where  $n$  is number of AB repeat units perpendicular to the graphitic plane. Using these two constraints, we can find out angle  $\theta$ .

However, we have to fulfill one more constraint. The length  $L$  which is determined by  $5/\cos(\theta)$  cannot be any length. This length has to be a multiple of periodicity ( $2.46 \text{ \AA}$ ) along zigzag direction (shown as  $\lambda$ ). To have all constraints valid, we wrote a script to come up with different graphitic orientations. These orientations would have well-defined angles based on the value of  $n$  and horizontal distance (5 nm in our case) which we put into the script. These orientation angles are shown in the table form in **Figure S1g**.

Using these constraints, 7 additional graphitic models (in addition to 0 and 90) were created for  $n$  ranging from 1 to 7. In all cases towards studying the effect of graphitic orientation, the thickness of the carbon surface model was fixed to be 10 nm. Systems were equilibrated as discussed in the main text.

## S2: Generation of interface models with different functionalization

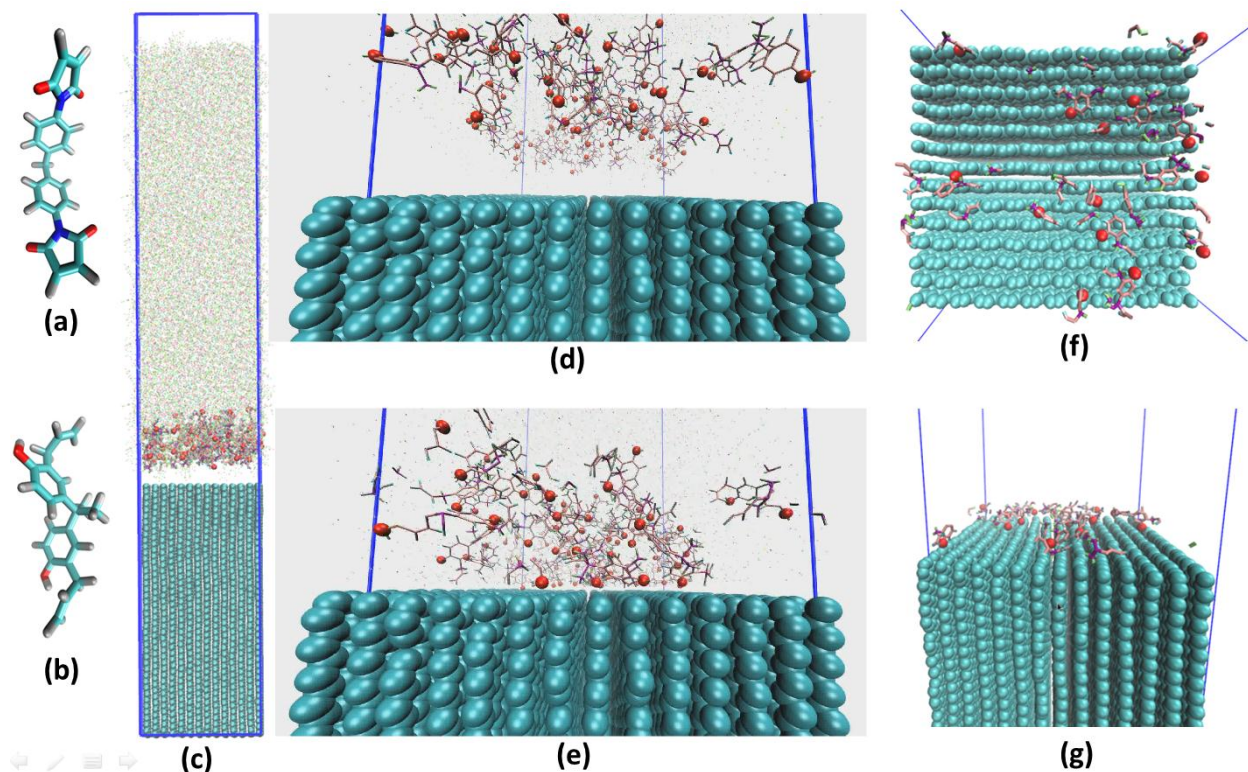


**Figure S2:** (a) BMI monomer: 4,4'-bismaleimidodiphenyl methane (BMPM); (b) BMI monomer: O,O' diallyl bisphenol A (DABPA); (c) combined starting system of  $C_{90}$  carbon surface model and equilibrated BMI monomeric matrix; (d) close-up view of starting confirmation of 2 nm region close to the interface; (e) close-up view of final confirmation of 2 nm region after dragging simulations; (f) top view of the interface 'O' atoms; (g) perspective view of interface 'O' atoms.

**Figure S2** shows the first phase of functionalization model that we used for functionalizing the surface of  $C_{90}$  graphitic model. **Figures S2a** and **S2b** show the monomeric units for the BMI matrix that we have used for modeling the matrix. First, the equilibrated matrix is combined with the  $C_{90}$  graphitic model as shown in **Figure S2c** using an in-house script in LAMMPS format. Moreover, 'O' atoms from hydroxyl groups of monomer DAPBA (red atoms in **Figure S2b**) in lower 2 nm region are selected and dragged towards the interface for subsequent bonding. These selected atoms are shown as red spheres in **Figure S2c-S2g**. The close-up view of a 2 nm region in the initial state is shown in **Figure S2d**. A MD simulation is subsequently run where a force of 1.0 Kcal/mole-Angstrom (LAMMPS units) is applied on each atom to drag them near the interface for 200 ps with a time-step of 0.5 fs. **Figure S2e** shows the final structure of the 2 nm region after the drag simulations. **Figures S2f** and **S2g**, respectively show the top and perspective view of the 'O' atoms which are very close to the surface.

Once the 'O' atoms are near the surface, the nearest carbon atoms (from  $C_{90}$  model) for each oxygen atom is identified for potential reaction (up to 13 atoms). These atoms are identified in a sequence for reaction such that functionalizing atoms are as far away as possible. This helps in maximizing the distribution of the functionalization groups. Towards this, an in-house script was written to identify the sequence of atoms for reactions which maximizes inter-particle distance for cases when we have only few functional-



ized atoms. This sequence is shown in **Figure S3** in part for 1, 4, 7, 10 and 13 functionalized carbon atoms leading to functionalization from  $0.05 \text{ nm}^{-2}$  to  $0.55 \text{ nm}^{-2}$ . Please note that the surface is in fact periodic in lateral X-Y dimensions.

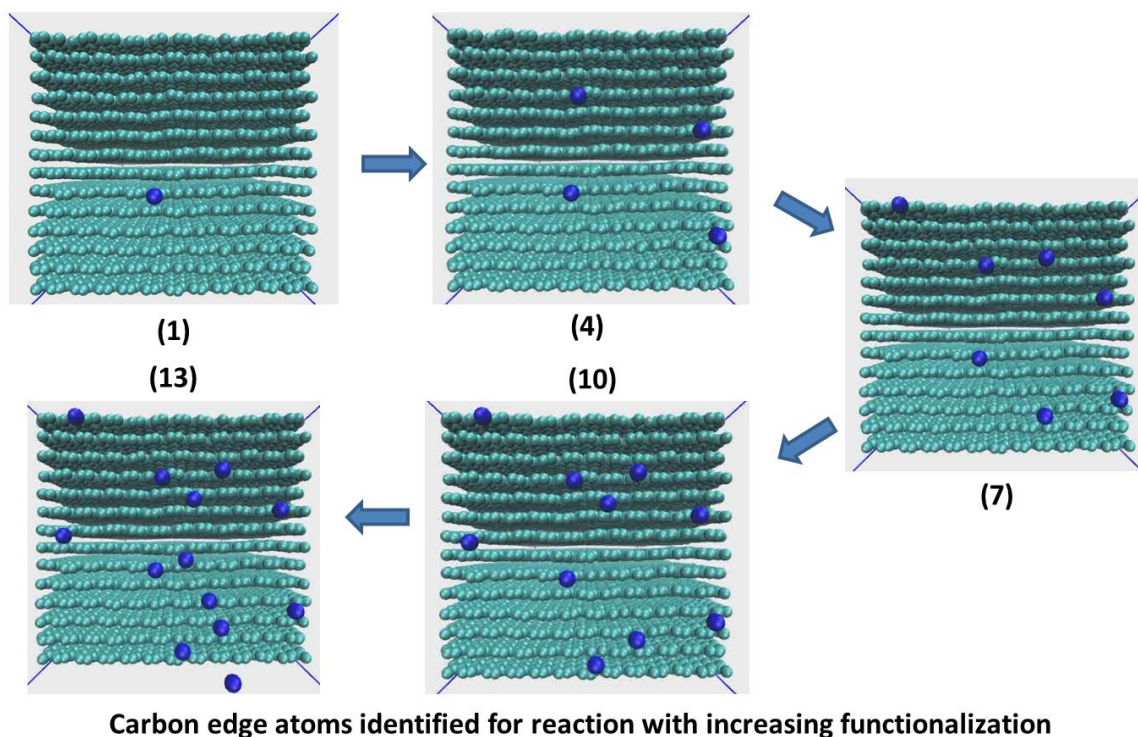


**Figure S3:** Schematic of 5 images showing the progression of selected carbon atoms for functionalization as we increase functionalization surface density, calculated using a script which maximizes distance between the bonded carbon atoms.

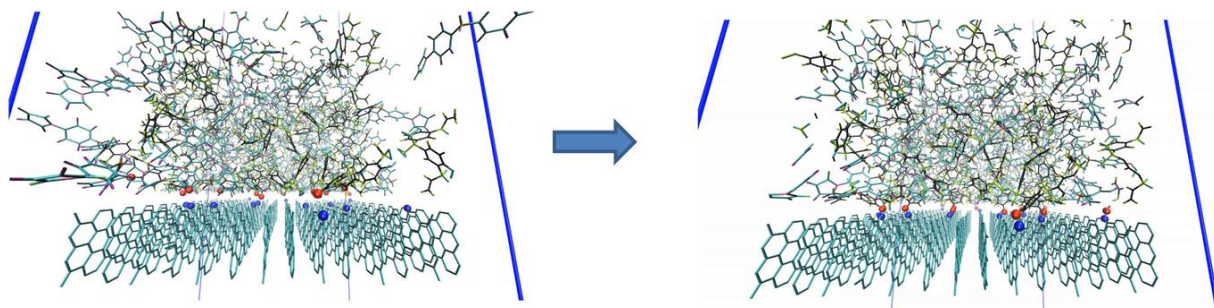


**Figure S4:** (Right) Initial structure of the interface before bonding; (Left) Final structure of the interface after bonding for 13 atom functionalization (functionalization surface density of  $0.55 \text{ nm}^{-2}$ ).

Once the atoms are identified, we create a bond between O (red) and C (blue) atoms and update the topology information of the LAMMPS datafile (new bonds, angles, dihedrals, impropers) and minimize the newly bonded structure. The initial and final geometry is shown in **Figure S4**.

Subsequent equilibration simulations are run as discussed in the main text, similar to other cases.



### S3: Generation of interface models with different surface roughness

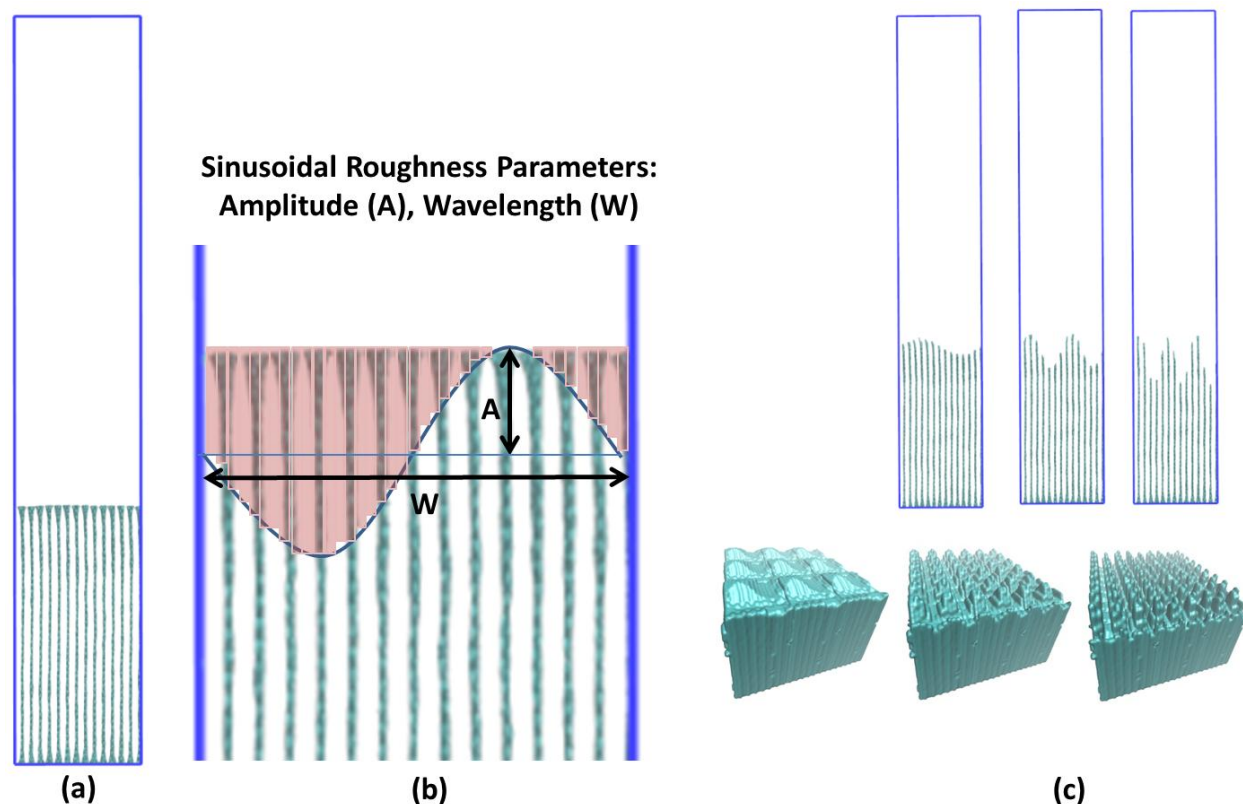


**Figure S5:** (a) Starting  $C_{90}$  carbon surface model; (b) Schematic of how the region is selected to delete atoms for creating roughness of amplitude  $A$  and wavelength  $W$ ; (c) Schematic representation of created rough  $C_{90}$  carbon surface models in side and perspective views (top and bottom images, respectively). Bottom images also include periodic images of the created rough surfaces (3X3 periodic boxes along X and Y direction) in initial configuration

**Figure S5** shows the steps for creating roughness in the modeled carbon surface models. For these set of simulations, we used a  $C_{90}$  model as shown in **Figure S5a**. The reasoning for using  $C_{90}$  is discussed later. In order to create roughness features of amplitude  $A$  and wavelength  $W$  (as shown in **Figure S5b**), we create a fictitious plane (parallel to X-Y plane)  $A$  Å (amplitude) underneath the surface as shown by the horizontal double sided arrow. Then, we create 10000 (100 bins X 100 bins) rectangular slabs of different heights (based on 2D sinusoidal curve) using the following script in LAMMPS (using lammps region module) as shown in partially shaded orange region in **Figure S5b**.

```
-----in.cut-----
.....
.....
variable      zmax equal bound(all,zmax)
variable      center equal ${zmax}-0.5*${amp}
variable      lowx equal xlo
variable      xd equal lx
variable      binlength equal ${xd}/${bin}*1.0

label         loop
variable      a loop ${bin}
variable      tempx equal ${lowx}+((${a}*1.0-0.5)*${binlength})
```

```

variable      x1 equal  ${lowx}+((${a}*1.0-1.0)*${binlength})
variable      x2 equal  ${lowx}+((${a}*1.0)*${binlength})
variable      xx equal  2*4*atan(1.0)*${temp}/${xd}
variable      z1 equal  ${center}+0.5*${amp}*sin(${period}*${xx})
print         "$a ${z1} ${zmax}"
if "${zmax} > ${z1}" then &
"region      temp block ${x1} ${x2} EDGE EDGE ${z1} ${zmax} units box" &
"delete_atoms region temp" &
"region      temp delete"
variable      temp delete
variable      x1 delete
variable      x2 delete
variable      xx delete
variable      z1 delete
next          a
jump          in.cut loop
.....
.....
-----

```

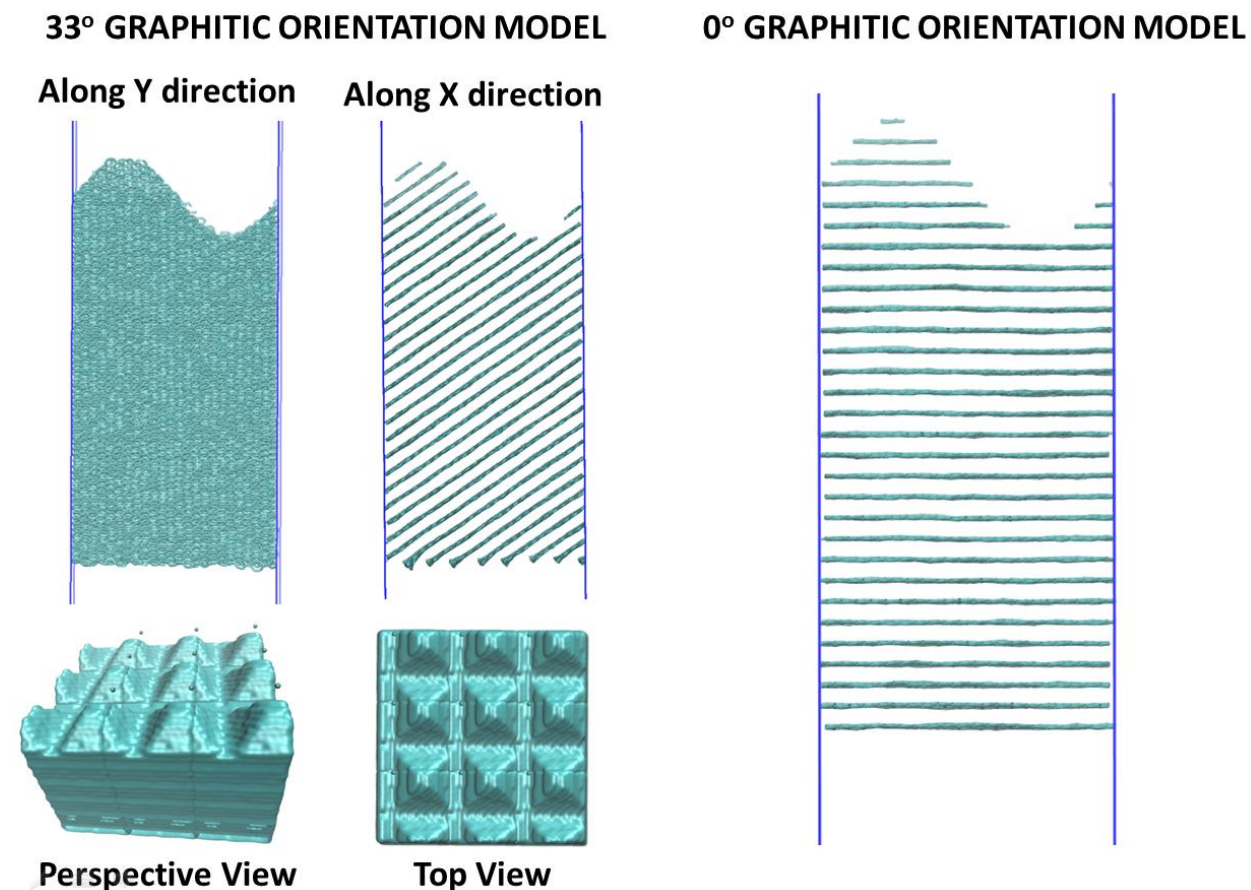


**Figure S6: Right:  $C_{33}$  carbon surface model showing roughness features as viewed along x- and y-direction. The bottom images show the perspective and top view of the rough  $C_{33}$  interface; Left:  $C_0$  carbon surface model as viewed along y-direction (into the plane).**

Here, the top z-coordinate ( $z_{max}$ ) of the individual slab is constant while the bottom z-coordinate ( $z_1$ ) varies based on the equations above. Moreover, slab bins along x- and y-directions are determined by overall box length along the respective directions, divided by 100. Once we have all regions defined, we delete

the atoms in these regions, resulting in sinoduidal roughness features on the surface as shown in **Figure S5c** for different amplitude and wavelengths. Thereafter, we further delete a few more atoms which have only 1 atom connected resulting from the previously deleted atoms. After that, we update the topology information (removing corresponding bonds, angles, dihedrals and improper angles) to generate a final LAMMPS data file for rough  $C_{90}$  carbon surface models, followed by their subsequent equilibration as discussed in the main text.

**Figure S6** depicts the reason for using only  $C_{90}$  model for roughness simulations. The figure shows 2 carbon surface models ( $C_{33}$  and  $C_0$ ) with created roughness features. As can be seen from the figure, the generated roughness features also lead to generation of small un-connected fragments (top region). It is expected that these un-connected fragments would diffuse into the matrix during the combined system's equilibration, thus defying the sole purpose of studying the effect of surface roughness on interface thermal transport. Hence, for investigating rough systems, other orientations except  $C_{90}$  were not considered.

## S4: Generation of interface models with CNTs incorporated at the interface

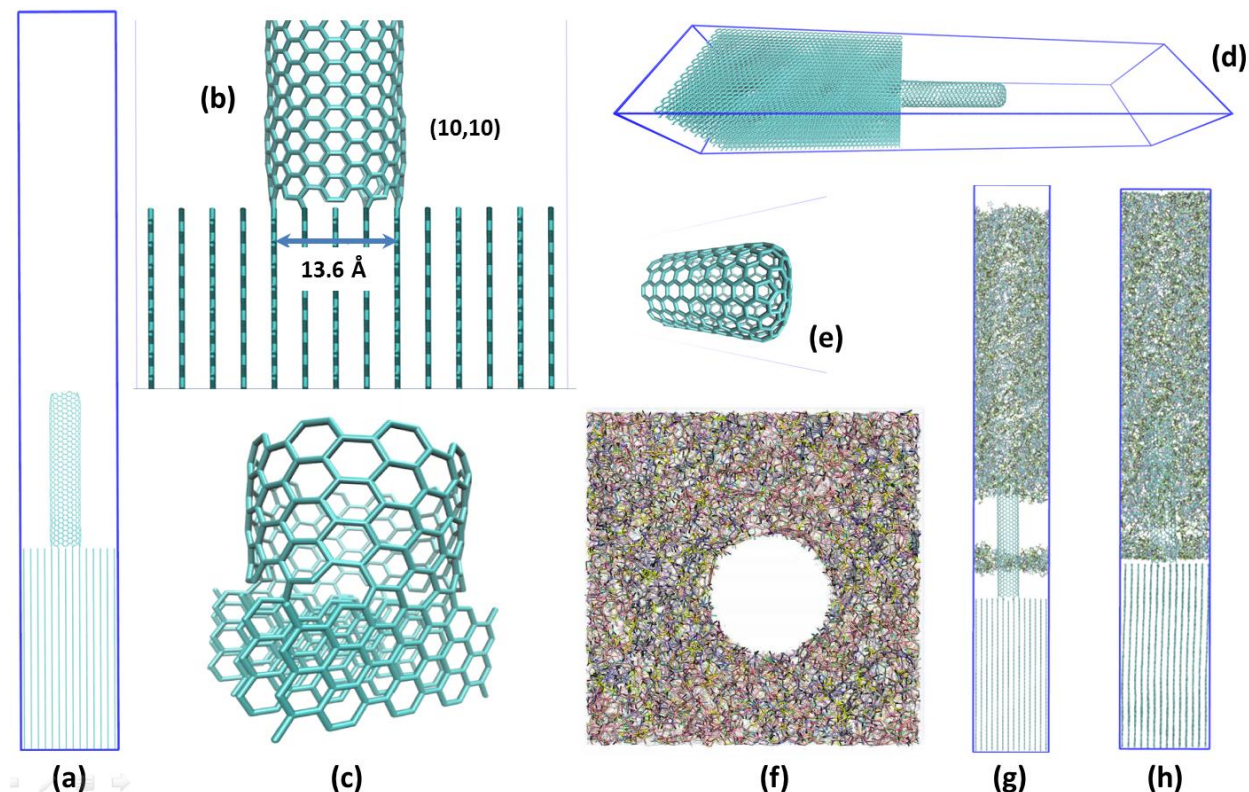


**Figure S7:** (a) Schematic of (10,10) SWCNT fused into  $C_{90}$  graphitic surface carbon model; (b) close-up view of the interface; (c) perspective view of the close-up interface; (d) perspective view of the capped (10,10) SWCNT; (e) close-up view of the SWCNT cap in equilibrium state; (f) schematic of BMI matrix, showing a cylindrical hole in the BMI matrix for SWCNT inclusion; (g) starting geometry of the combined matrix and fused-SWCNT carbon surface model; and (h) snapshot of the combined system after 100 ps NPT simulation showcasing that most of the empty space is disappeared.

In order to create a fused junction of carbon nanotube (CNT) with graphitic carbon surface model, the  $C_{90}$  surface model was chosen. This model was primarily chosen for the reason that CNTs could be fused perpendicular to the interface with the most connectivity (most CNT atoms connected to the  $C_{90}$  surface atoms). One such overall junction is shown in **Figure S7a** (junctions with different CNT lengths were created). The close-up version of the interface is shown in **Figure S7b**. This sub-figure also depicts why (10,10) CNT was chosen to fuse with the  $C_{90}$  graphitic model. As seen from the figure, the diameter of (10,10) is 13.6 Å, which is very similar to the distance between 4 graphitic layers. This matching resulted in 12 of the 20 atoms getting connected to 4 graphitic layers. Also, the symmetry of the nanotube (along  $C_{2v}$  axis) as well as its arm-chair nature resulted in perfect connectivity at both ends of the CNT. This smooth transition of connectivity is shown in **Figure S7c**, where 6 benzene rings (3 on each side) are smoothly transitioned from the graphite layers to CNT. Once the bonds were created, the new topology information (new bond angles, new dihedrals, new improper angles) was incorporated in the updated LAMMPS data file using an in-house script.

During the preparation it also occurred to us that because of the large diameter of fused CNTs (> 1nm), BMI matrix molecules might get trapped inside the CNTs because of its open nature on one end (end

away from the graphitic interface). In order to circumvent the problem, (10,10) capped SWCNTs (on one end) were created and fused at the open end using the methodology discussed above. **Figure S7d** shows the graphitic carbon surface model with a fused-capped-SWCNT while **Figure S7e** shows the close-up of the equilibrated nanotube cap.

In order to combine the CNT incorporated carbon surface  $C_{90}$  model into the BMI matrix, a 20 Å diameter hole was created within the BMI matrix along the  $z$ -direction as shown in **Figure S7f**. This was done using “fix indent” module of LAMMPS MD software. The hole was radially grown from a radius of 0 to 10 Å over 100 ps MD run to avoid sudden changes in the geometry of the BMI matrix molecules. Once the hole was created, both systems were combined in a single LAMMPS data file using an in-house script as depicted in **Figure S7g** and were equilibrated for several nanoseconds (**Figure S7h**).

Using this methodology, 4 different systems with CNT length ranging from 3 nm to 9 nm were created to understand the effect of CNT length (and thus effective surface area) on interfacial thermal transport across BMI-matrix carbon-fiber interface.

**S5: Estimation of temperature gradient across the interface using steady-state temperature profile.**

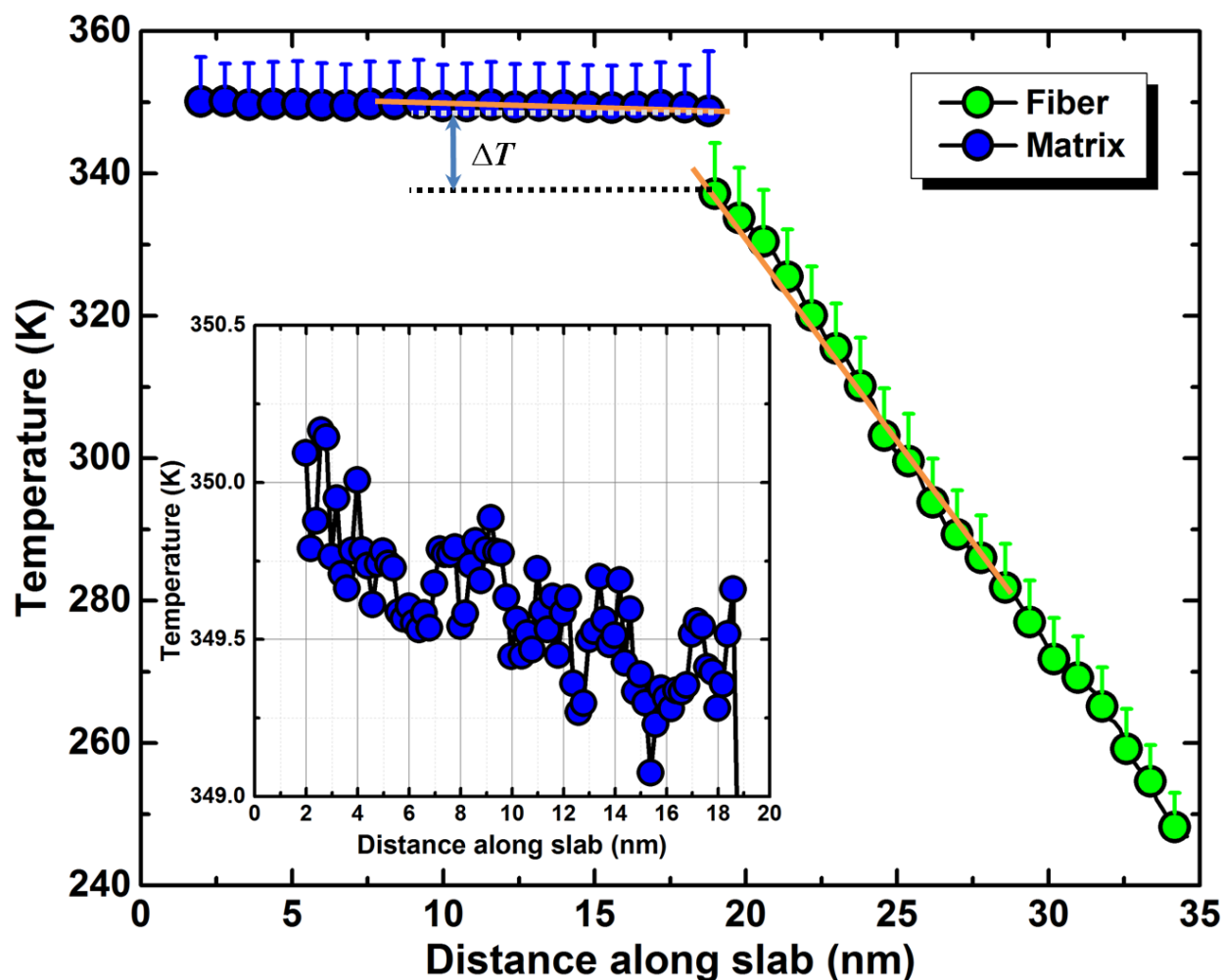


**Figure S8: (Main) Steady-state temperature profile of a representative case showcasing the temperature drop across the interface of carbon-fiber and matrix; (Inset) Steady-state temperature profile of the carbon-fiber.**

**Figure S8** shows the steady-state temperature profile as well as the temperature drop across the interface. The inset also shows that the monotonic temperature drop (amid fluctuations) across the carbon fiber is very small since the thermal conductivity of the graphitic carbon fiber is significantly higher than that of matrix. In order to calculate the temperature drop, the data from both side of the interface was fitted to a linear fit as shown in the figure. Then, based on the fitting,  $\Delta T$  at the interface was calculated as depicted in the figure for thermal conductance estimation.



## S6: Estimation of heat flux using LAMMPS output data

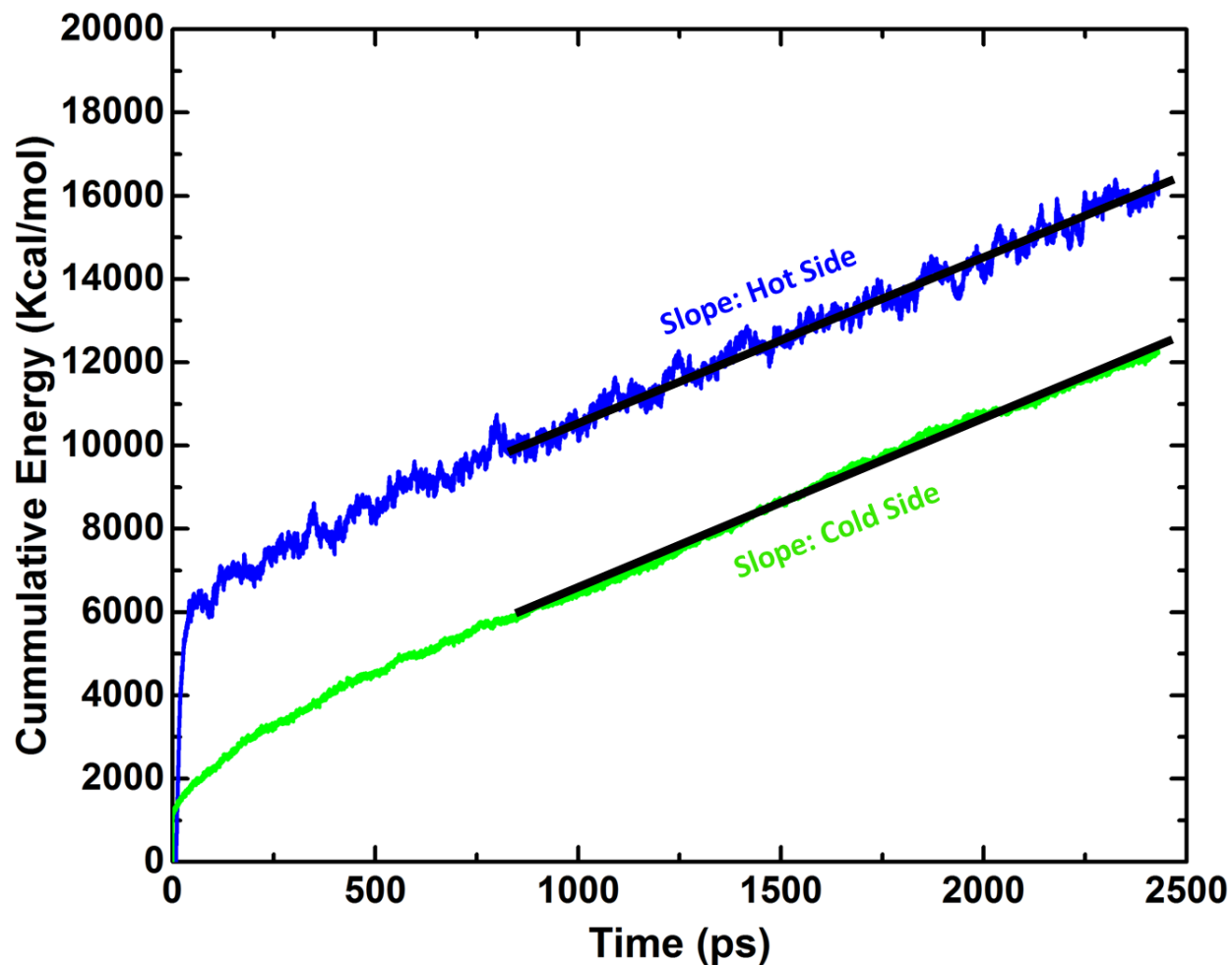
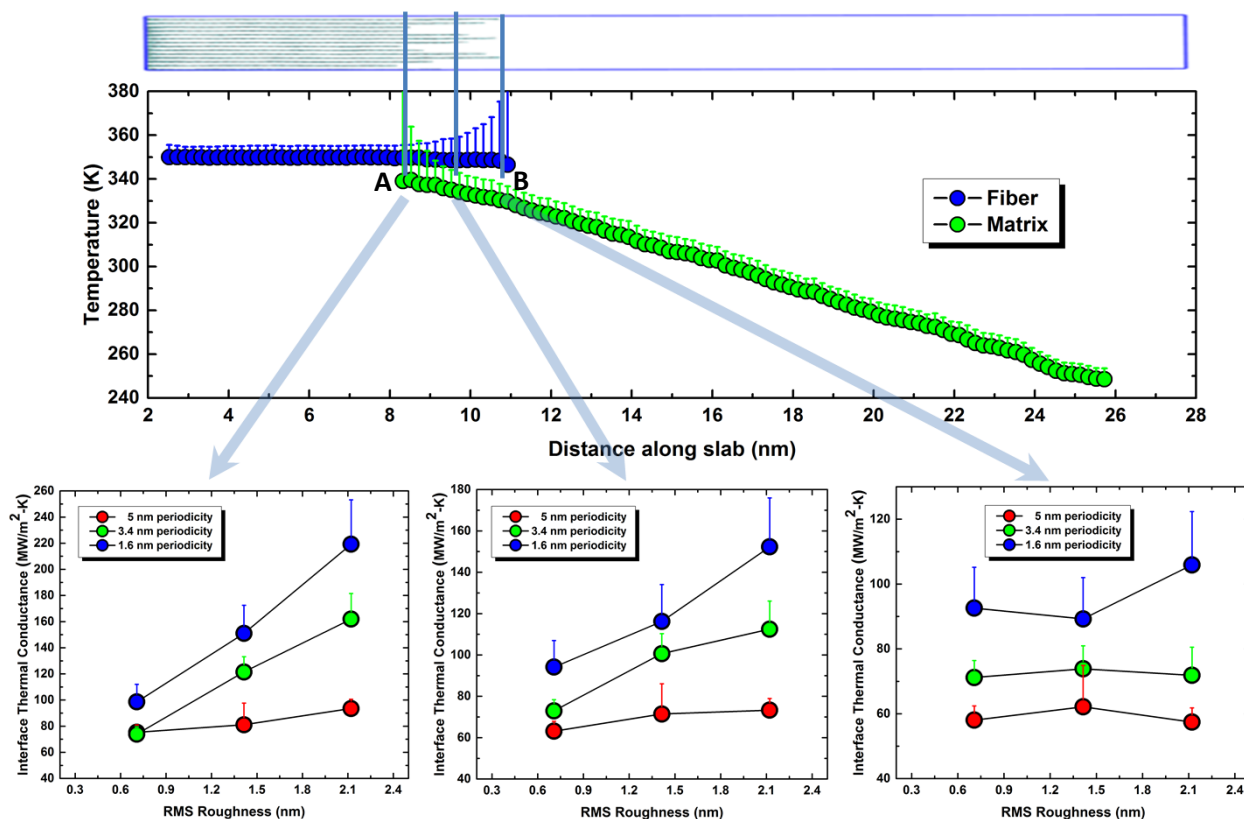


Figure S9: Plot of cumulative energy added (blue) and taken out (green) from hot and cold thermostats, respectively, as a function of simulation time for a representative case. The slopes are linear fit to data.

**Figure S9** shows the LAMMPS output cumulative energy as a function of simulation time. The heat flux is calculated from the slope by fitting the data to a linear fit, followed by its division by the perpendicular surface area (along X-Y plane), thus giving the units of kcal/mol/Å<sup>2</sup>/ps, which was subsequently converted to W/m<sup>2</sup>.

## S7: Effect of using various interfaces for interface thermal conductance calculations for rough interfaces



**Figure S10:** (Top) Figure showing the overlap region of the rough interface in terms of its temperature calculations. (Bottom) Plots of interface thermal conductance as a function of RMS roughness for different periodic roughness values, calculated at directed interfaces.

**Figure S10** clearly depicts the ambiguity of calculating ‘interface’ thermal conductance across rough interfaces. As seen from the figure, the calculations provide very different quantitative values as well as qualitative trends depending upon the chosen interface. The reason being that although, the heat flux and cross-sectional area are constant,  $\Delta T$  is noticeably different at selected interfaces. In such cases, it becomes ambiguous as to which interface should be chosen. To avoid that ambiguity, we calculated ‘inter-phase’ thermal conductance between points A and B as discussed in the main text.



**S8: Visual differences between  $C_0$  and  $C_8$ - $C_{90}$  graphitic orientation cases with respect to applied thermostats**

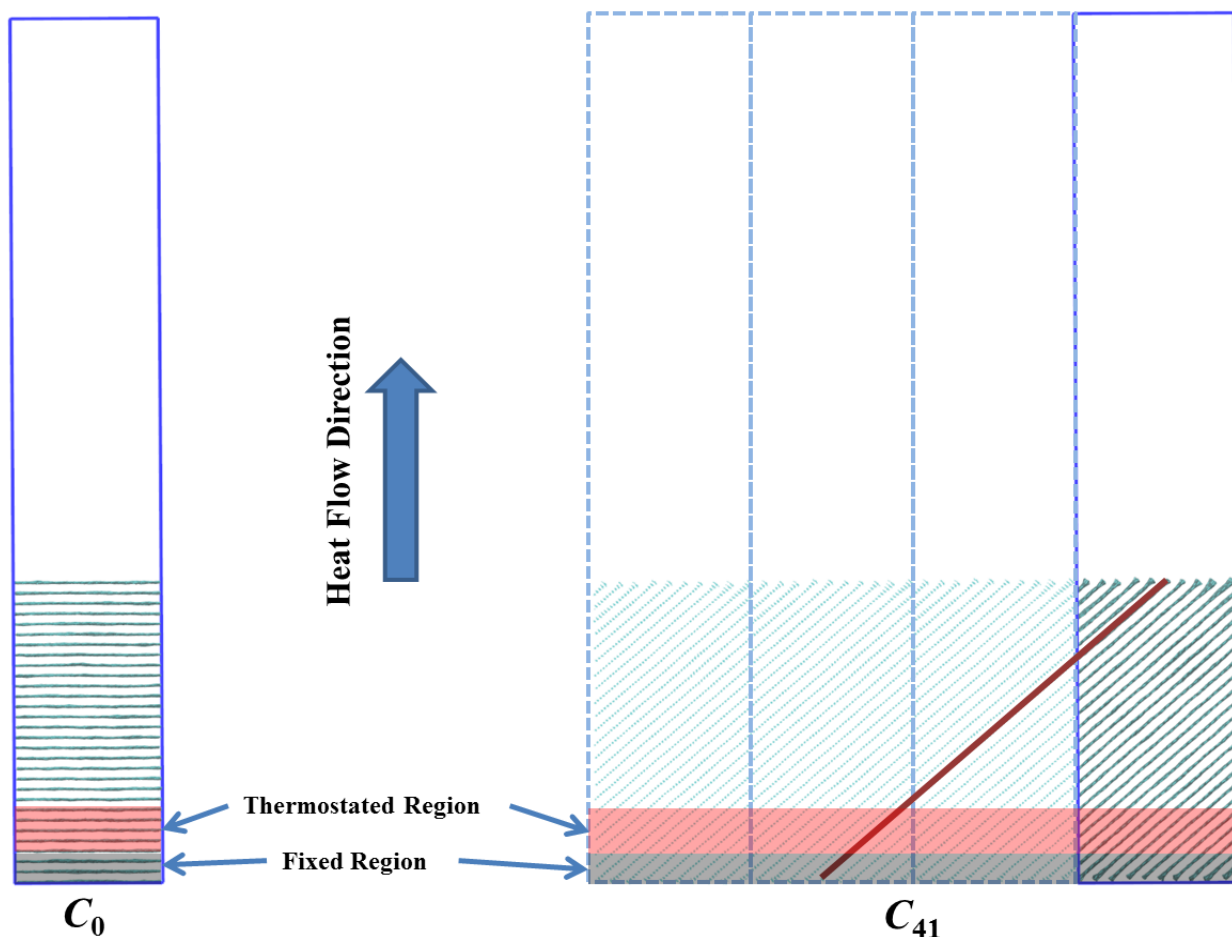


**Figure S11: (Right)  $C_0$  graphitic orientation model; (Left)  $C_{41}$  graphitic orientation model. Here, 3 periodic images (with periodic boxes) of the graphitic layers are also shown to further clarify the periodically wrapped graphene connectivity.**

**Figure S11** visually shows the difference of how heat is transported from hot thermostats to graphitic interface region in  $C_0$  vs  $C_{41}$  graphitic orientation cases. For the  $C_0$  model, heat propagates along the out-of-plane direction of graphitic layers before reaching the interface. On the other hand, for  $C_{41}$  model, heat propagates parallel to the graphitic plane and reaches the interface due to the huge thermal anisotropy of graphite (thermal conductivity along graphite plane is  $>100$  times higher than out-of-plane direction). We should also point out that the effective length of heat propagation here is significantly longer than 10 nm and is determined by the orientation angle.

## COVER SHEET

Paper Number: **803**

Title: **Molecular Modeling of Thermo-Physical Properties of BMI Matrix and its Interface with Amorphous Carbon Fiber**

Authors:     Vikas Varshney  
               Ajit K. Roy  
               Jeff Baur

## ABSTRACT

Very rapid heating of composite material leads to matrix thermal decomposition, amorphous char formation, ablation, etc. and results in the variability of local thermo-physical properties. It is desired to delay the onset of matrix degradation by incorporating/tailoring the fiber-matrix interface for efficient thermal energy transfer and helping in faster dispersion/distribution of supplied thermal energy and thus, necessitates the understanding of the interface as well as interfacial thermal transfer across the fiber/matrix interface. Within the context of modeling laser irradiation based rapid heating of nanocomposites, i.e., modeling of thermal energy transfer across the composite's interfaces and subsequent polymeric ablation, this study focuses on building a model and investigating physical and thermal properties of high-temperature imide-based resin (BMI-5292) matrix using molecular dynamics simulations. A molecular model of BMI-5292 based on AMBER force field and GAUSSIAN-derived RESP charges is developed and validated against several experimentally measured thermo-physical properties such as density, glass transition, thermal conductivity, etc. In parallel, to mimic the carbon fiber surface, a model of amorphous carbon is developed using the Tersoff (bond-order) potential. Subsequently, using non-equilibrium molecular dynamics simulations, interfacial thermal energy exchange is investigated in terms of thermal conductance at carbon fiber-matrix interfaces for different degrees of crystallinity within the carbonaceous region. The obtained thermo-physical results are found to be in good agreement with available literature, thus providing an accurate and reliable foundation of the molecular force-field to tackle more complex phenomenon (such as polymeric ablation) from molecular dynamics simulations with respect to high-temperature resins.

---

Vikas Varshney, Materials Scientist  
Ajit K. Roy, Principal Materials Research Engineer  
Jeff Baur, Principal Materials Research Engineer  
Materials and Manufacturing Directorate, Wright Patterson Air Force Base, Air Force  
Research Laboratory, Dayton, OH 45433

## INTRODUCTION

Today, laser technology is being used in a wide variety of fields including communications, industrial and environmental applications, medicine, and materials' research and development (R&D). Some of the key areas in materials' R&D include mass spectral analysis using matrix-assisted laser desorption/ionization (MALDI) and fabrication of micro-/nano-patterned surfaces and thin films using pulsed or continuous lasers (such as micro-fabrication of electronic devices and micro-patterning of polymeric composites). Our specific interest lies in how the different lasers interact with polymeric composite materials; what parameters are of important significance which governs their mutual interaction; and how such interaction leads to matrix thermal decomposition, amorphous char formation, and polymeric ablation.

The basic mechanism of laser interaction with materials incurs many non-equilibrium photo-processes (thermal, mechanical, chemical, physical) caused by fast deposition of laser energy and its dissipation in various forms [1, 2]. Because of the rapid heating rate, these non-equilibrium processes cause spatial variability in thermo-physical properties of the matrix of interest such as local heating, local matrix degradation due to sudden local increase in temperature, pressure wave formation, etc. [1, 2]. It is often desired to delay the onset of ablation and keep the composite intact by tailoring the interfaces of matrix and fillers (such as carbon fibers, carbon nanotubes, etc.) by modulating interactions between the two constituents. To better understand how lasers interact with composites, one needs to investigate the correlation between experimental laser parameters, i.e., type of laser (pulsed or continuous), its fluence and incident angle, penetration depth, and composite materials parameters, i.e., molecular chemistry, cohesive energy, thermo-physical properties, mechanical properties, matrix-filler interfacial interactions, etc.

Figure 1 shows the occurrence of different physical and chemical events after laser absorption along with their respective timeframe [1]. As these events span over several orders of magnitude in time, it is impossible to provide a consistent analytical description of all processes and address all relevant physics and chemistry within a single computational framework. It can be seen from the figure that a multitude of interesting molecular events occur at the picosecond (ps) to nanosecond (ns) time scales, investigations and understanding of which is best suited using molecular dynamics (MD) simulations [3] as it operates at these timescales. In these simulations, only the details of microscopic interactions need to be specified (often extracted using quantum chemical calculations) and no further assumptions need to be made in order to investigate the equilibrium and non-equilibrium phenomenon happening at these timescales.

With our specific interest in Matrimid™ BMI-5292 matrix based carbon-fiber composites and to understand how laser absorption leads to the heat dissipation, matrix degradation and the eventual ablation within our system of interest, this study provides an initial framework along the specified questions. Specifically, in this study, we built a full-atomistic model of BMI-5292 resin monomer mixtures and calculate their thermo-physical properties (density, glass transition temperature, thermal conductivity, coefficient of linear thermal expansion) using MD simulations and compare the results with reported experimental values. Furthermore, we investigate the thermal energy exchange across the carbon fiber (amorphous)—BMI-matrix interface. We believe that this initial investigation provides a foundation for the

validity and accuracy of the employed MD force-field and can be built upon further to investigate more complex issues of interests such as polymeric ablation with molecular precision.

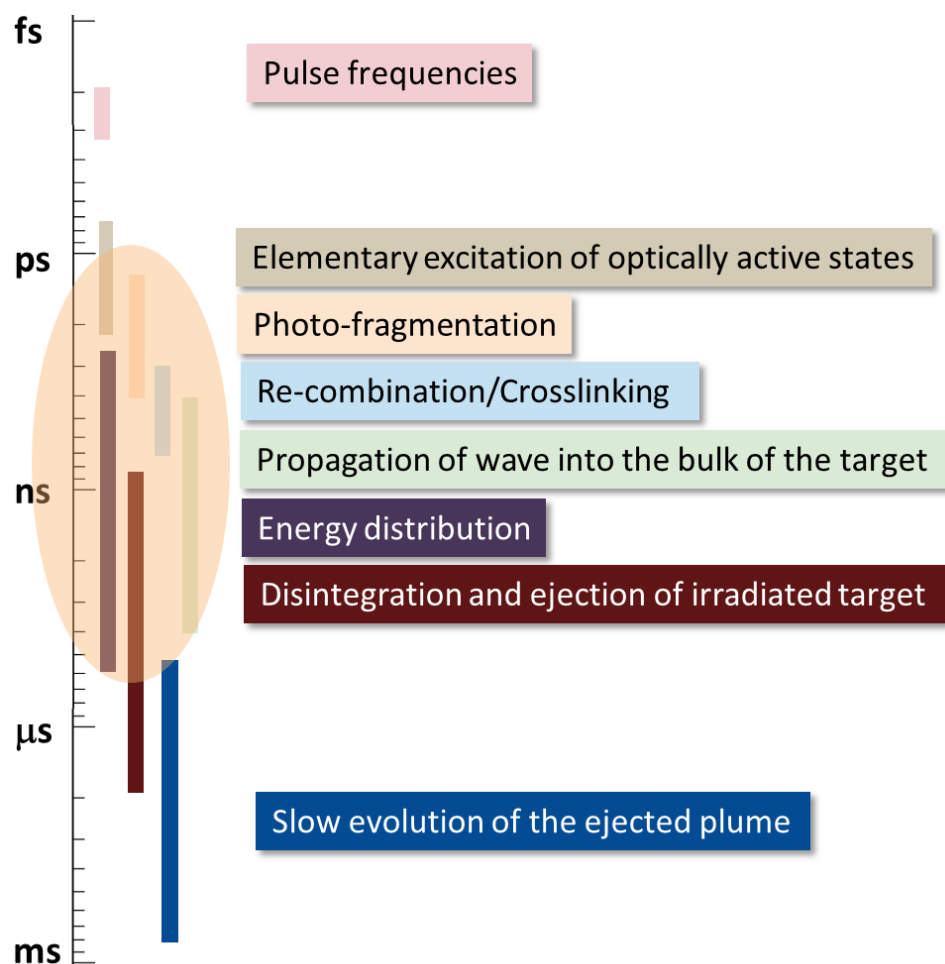


Figure 1. A schematic flow of events that occur after absorption of laser energy along with their respective timeframes. The partially transparent shaded region (~1 ps -10s of ns) is the timeframe that is best suited for MD simulations.

## SIMULATION METHODOLOGY

### Simulation Setup and Methodology: BMI Matrix

The BMI resin (Matrimid™ BMI-5292) is a copolymer composed of 4,4'-bismaleimidodiphenyl methane (BMPM) and *O,O'* diallyl bisphenol A (DABPA) monomers in a 1:1 molar ratio [4]. The schematic representations of these monomers are shown in Figure 2. As a part of simulation set-up, these monomers were constructed in Materials Studio® Visualizer [5]. Several force-fields (CVFF [6], PCFF [7], AMBER [8, 9]) were tested for successful generation of bonded and non-bonded parameters. However, only the general amber force field (GAFF) was able to generate all required parameter sets among the tested force fields [8]. Hence, the GAFF force-

field was employed for testing its accuracy and to model BMI matrix monomers for this study.

It is often reported that when using the GAFF force-field, restrained electrostatic potential (RESP) charges are best suited to model organic and bio-molecules [8, 9]. For our simulations, RESP charge estimations and fittings were performed using GAUSSIAN09 software [10] and RESP code within the framework of the R.E.D. program [11]. Further details on the charge estimation will be provided later in the results and discussion section. Once all the required parameterization was done, the GAFF force-field and the coordinates of the BMI matrix components were imported into LAMMPS molecular dynamics package to carry out molecular dynamics (MD) simulations [12]. A cutoff of 12 Å was used for van-der Waals interactions and short range electrostatics, while long range electrostatics was treated using the PPPM methodology [13] as implemented in LAMMPS. Visual molecular dynamics (VMD) software was employed to visualize the trajectories and create representative schematic visualizations that are reported in this study [14].

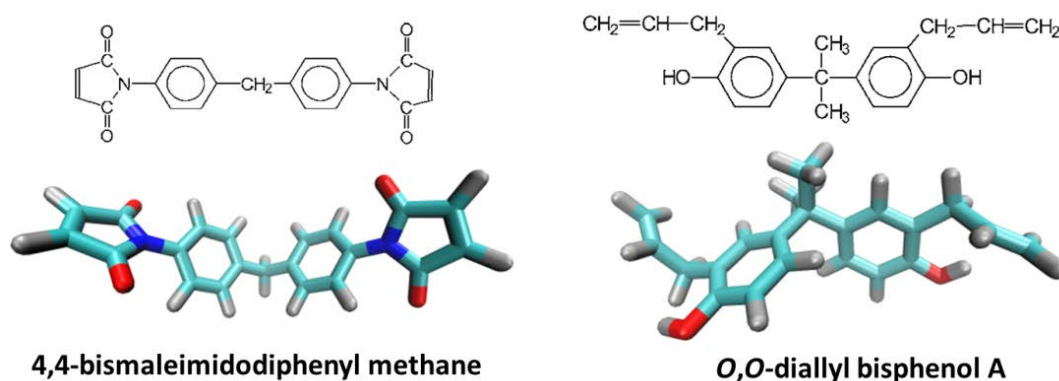


Figure 2. Molecular representation of the two monomer components of the Matrimid™ BMI-5292 resin. Color Scheme: cyan-carbon; blue-nitrogen; red-oxygen; silver-hydrogen.

First, a system of ~9500 atoms was created by replicating both BMI monomers 108 times (total) along  $x$ -,  $y$ -, and  $z$ -directions as shown in Figure 3(a). Then, MD simulations were carried out in NVT (canonical) ensemble to equilibrate the temperature, followed by NPT (isothermal-isobaric) ensemble to equilibrate the density (and pressure). Periodic boundary conditions were employed in all 3 orthogonal directions to mimic bulk-like behavior. While the successful temperature equilibration (NVT simulations) was achieved within 200 ps, the equilibration of density (NPT simulations) required significantly longer simulations. In total, ~10 ns of NPT simulations with independent barostats along the 3 directions were performed for successful equilibration of density. Afterwards, a relatively shorter run of 200 ps was performed in NVE (micro-canonical) ensemble to confirm the energy conservation of the system. A timestep of 1.0 femtosecond (fs) was used for these set of simulations during the equilibrium phase. The representative equilibrated snapshot is shown in Figure 3(b). After successful equilibration, the system was subjected to a series of additional simulations for estimation of glass transition temperature ( $T_g$ ), density variations with temperature, coefficient of linear thermal expansion (CLTE) and

thermal conductivity ( $\lambda$ ). For the sake of continuity of discussion, the methodology for the specific simulations will be summarized in appropriate sections later on.

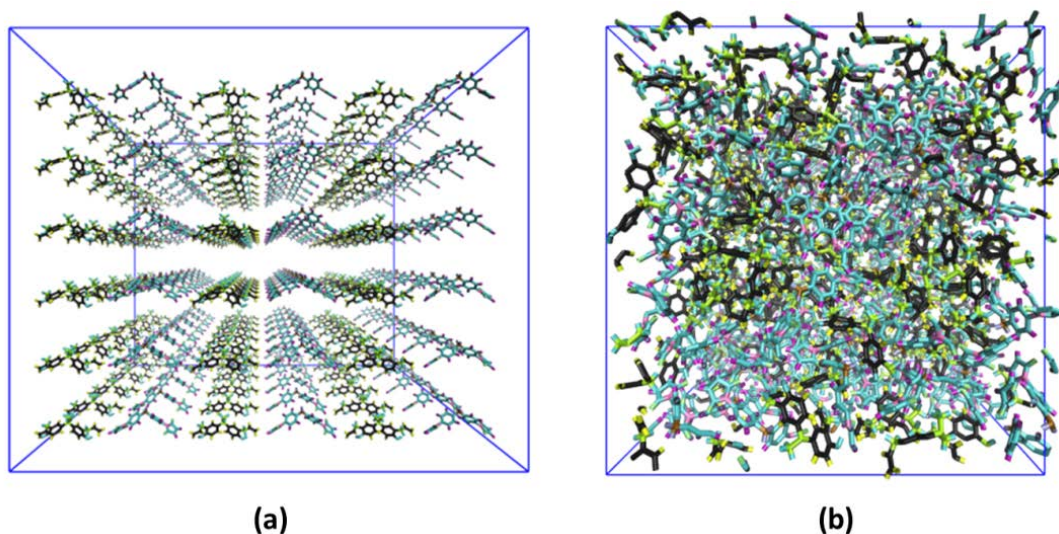


Figure 3. Schematic representation of the (a) initial and (b) equilibrated geometry of the BMI-5292 component mixture (~9500 atoms) as discussed in the text. Visually, the red-bluish and green-blackish molecules represent BMPM and DABPA, respectively.

### Simulation Setup and Methodology: Carbon Fiber Surface

Initially, a diamond lattice of dimensions  $\sim 5 \times 5 \times 5 \text{ nm}^3$  was generated using Materials Studio® Visualizer. The structure was then rapidly heated to 12000 K in NVT ensemble using the Tersoff potential [15] as implemented in LAMMPS MD package. Periodic boundary conditions were used in all 3 directions at this stage. Due to the short-range nature of the Tersoff potential, the large temperature fluctuations at elevated temperatures led to randomization of the lattice, and thus, the generation of the amorphous structure. This amorphous structure was then allowed to cool down to room temperature at three different cooling rates (1K/ps, 10K/ps and 100K/ps) in NPT ensemble with independent barostats in all 3 periodic directions. During cooling, nano-crystalline diamond domains were formed for the low cooling rate (1K/ps), while a fully amorphous structure evolved for higher cooling rates. Afterwards, the cooled structures were further relaxed under NPT and NVE ensembles for  $\sim 500 \text{ ps}$  at room temperature for density and energy conservation, respectively. The flow of the carbonaceous system simulations is better represented in Figure 4, along with representative snapshots of annealed and equilibrated bulk structures. Here, we should point out that since the Tersoff potential does not have a dispersion interaction component to it, graphitic order (enhanced  $\text{sp}^2$  order and graphene layers) was not observed in nano-crystalline domains. Once the fully relaxed amorphous bulk-like carbon structures were realized, two surfaces (for each case of annealed carbon structure) were generated by increasing the  $z$ -dimension of the box. The structure was further relaxed in NPT ensemble at room temperature to relax the stresses of the newly-generated surfaces. A time step of 0.5 fs was employed throughout the



equilibrium stage. We should point out that another bond-breaking potential, namely AIREBO [16], was also tried to generate equilibrated structures of the matrix. However, none the simulations were successfully finished and were crashed during the initial heating stage of the process.

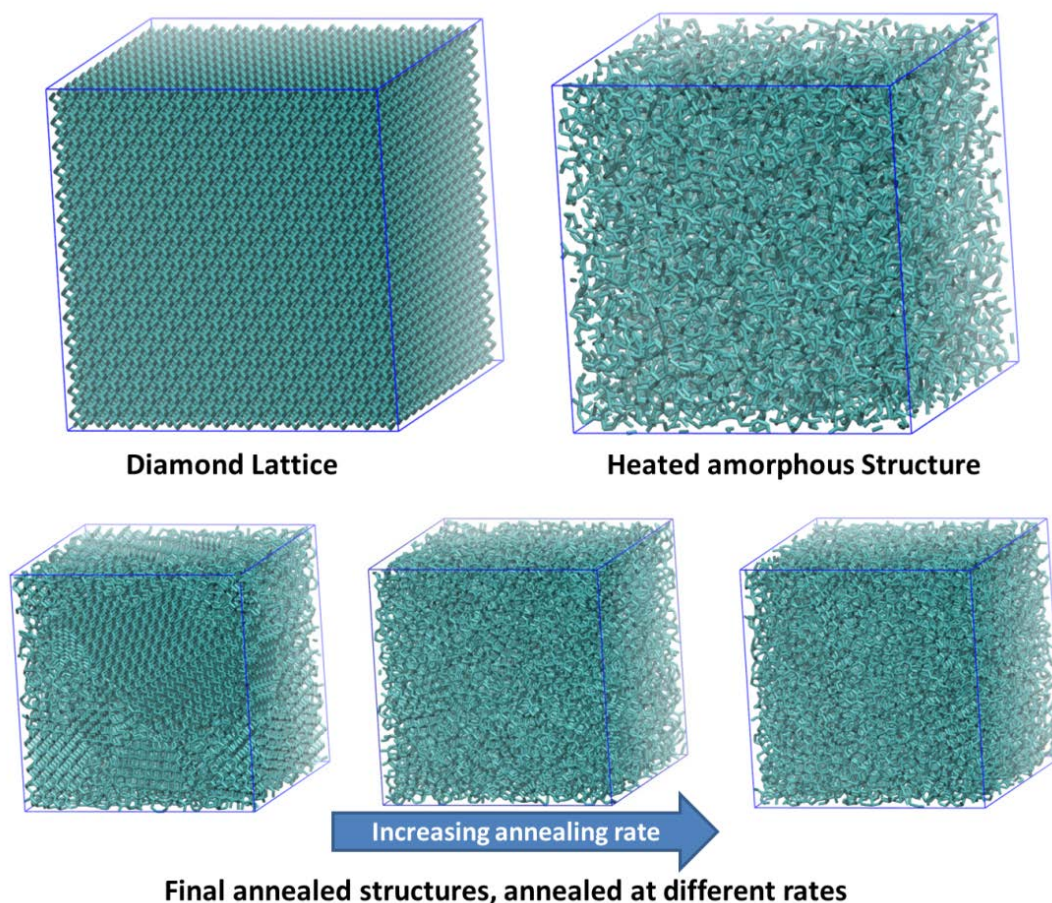


Figure 4. (Top Left) Initial diamond lattice; (Top Right) Heated amorphous structure @6000 K; (Bottom) Equilibrated bulk structures, obtained by cooling down the top-right structure with different rates. It is clear the fast cooling leads to amorphous structure while slower cooling lead to the formation of nano-crystalline diamond domains.

## Simulation Setup and Methodology: BMI and Carbon Fiber Interface

To calculate the interface thermal conductance (ITC) across fiber-matrix interfaces, three combined systems were created using the relaxed BMI matrix and different equilibrated amorphous carbon structures to mimic the fiber-matrix interface. A home-grown code was written in C++ in order to generate initial combined geometries (see Figure 5(a)). Within this code, the BMI matrix was replicated along the  $z$ -dimension 4 times to create a slab-like geometry, and was then combined with the equilibrated carbon surface structure to generate initial coordinates for modeling the matrix-fiber interface. Interaction between the matrix and fiber was evaluated using short-range van der Waals interactions. Here,  $\varepsilon$  and  $\sigma$  parameters for carbon of



the fiber-surface were employed to be 0.086 kcal/mol and 3.4 Å, respectively, while GAFF force-field parameters were used for the matrix. A cut-off of 12 Å was used for van der Waals interactions. The van der Waals interaction parameter cross-terms between the matrix components and the fiber surface were calculated using Lorentz-Berthelot mixing rule [17].

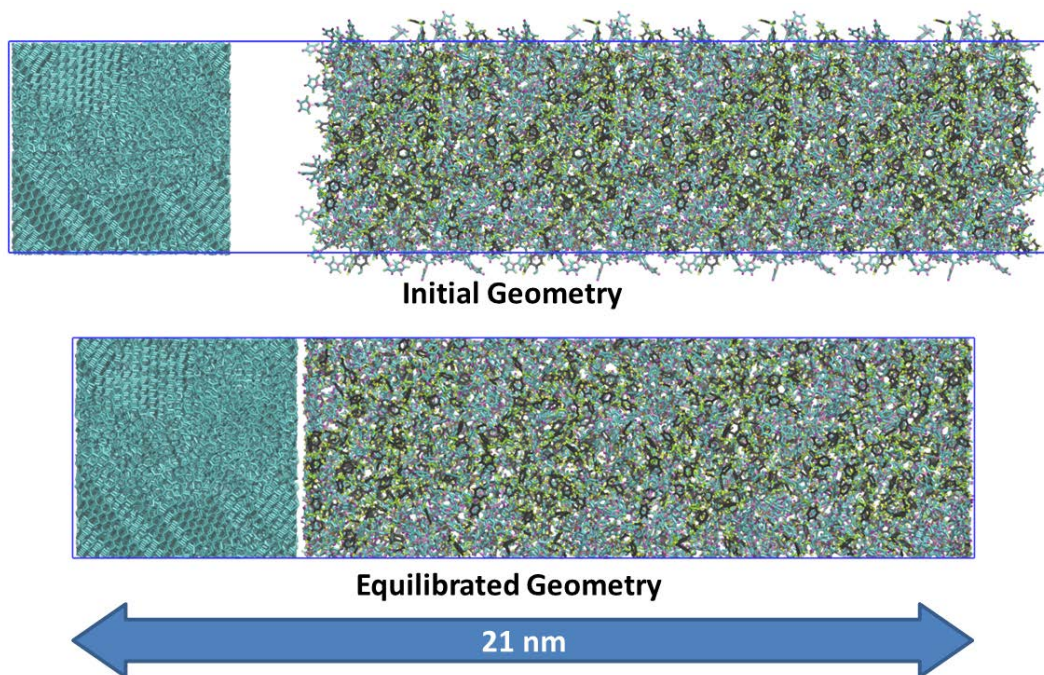


Figure 5. Representative snapshot of the (a) initial generated geometry and (b) final equilibrated geometry. The color scheme for this figure is same as Figure 3 and Figure 4.

Once the combined initial geometry was finalized, NVT and NPT simulations were ran in succession to equilibrate the temperature and pressure of the combined system, respectively. Similar to the previous BMI discussion, while the temperature was equilibrated within 200 ps, all the pressure components reached equilibration after 4 ns of simulation. The testing for equilibration of NPT simulations was evaluated by confirming that all 3 box dimensions were equilibrated and were not changing with time. After equilibration, non-equilibrium MD (NEMD) simulations were performed to calculate interface thermal conductance. The details of the conductance simulations will be discussed in an appropriate section for the sake of continuity of discussion.

## RESULTS AND DISCUSSION

### Atomic Partial Charge Calculations using R.E.D.

RESP charge calculations were performed using RESP-ESP charge Derive (R.E.D.) program as briefly mentioned above. We should point out that RESP atomic charges are often preferred when employing GAFF force field (AMBER) for MD

simulations. First, Materials Studio® Visualizer was used to build 4 different molecular conformations (models) of each of the two matrix components. Then, all the models were optimized using HF/6-31G\* level with tight convergence criteria in GAUSSIAN09 program, followed by molecular electrostatic potential (MEP) computations at HF/6-31G\* level. Merz Singh Kollman [18] method was used during the calculation of atomic point charges in Gaussian09. The final electrostatic charge fitting was performed using resp2.2 code as provided with R.E.D. program [11]. The output charges of each component were compared for different starting conformations and were averaged out to get final charges. We should point out that for both monomers, negligible differences were found in the final estimated charges. Finally, the charge output along with GAFF force-field (for bonded and van der Waals interactions) was imported into LAMMPS format using AMBER's *xleap* program and *amber2lammps* python script as provided with LAMMPS [12].

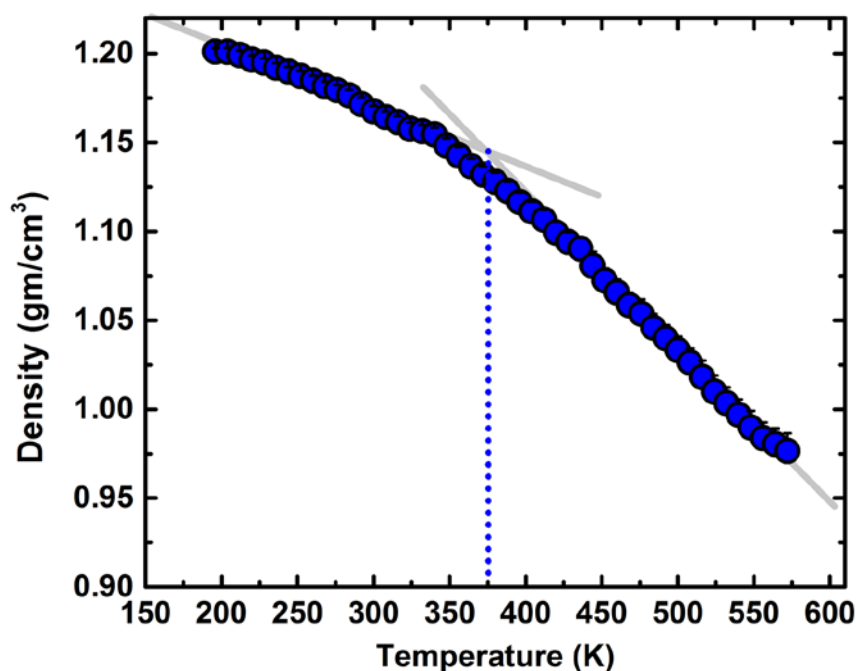


Figure 6. Plot of BMI matrix density as a function of temperature, calculated using equilibrium volume simulations (second set of simulations; see text). The gray lines are fitted to the low and high temperature profiles to estimate  $T_g$ .

### Thermo-Physical Properties of BMI Matrix

To evaluate thermo-physical properties and their variation with temperature, the previously equilibrated BMI matrix (~9500 atoms) was heated to 560 K in NPT ensemble for 200 ps. Thereafter, two sets of simulations were performed to model the temperature behavior of different thermo-physical properties. In the first case, the matrix was annealed to 200 K at two different rates (0.01 K/ps and 0.25 K/ps) from 560 K. This was done to investigate how the cooling rate affects the glass transition temperature of the matrix. For the second set of simulations, the room temperature matrix was ramped up or down to a desired temperature (between 200 K and 560 K

with steps of 40 K) over 200 ps, followed by 1 ns of equilibrium simulations in NPT ensemble. In these simulations, the last 200 ps of data were used to calculate equilibrium volume/density at that temperature.

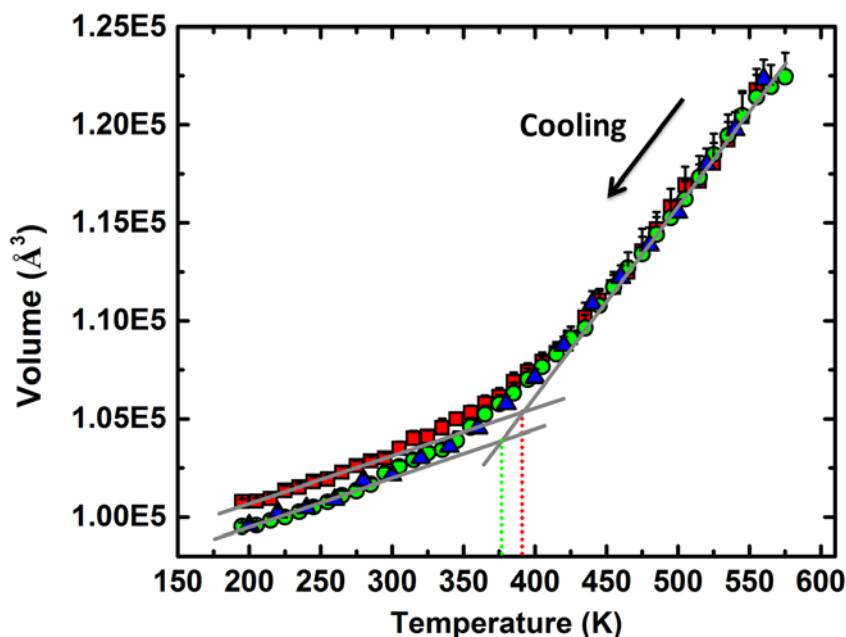


Figure 7: (Right) Plot of matrix volume as a function of temperature for fast annealing simulations (red squares), slow annealing simulations (green circles) and equilibrium simulations at each temperature (blue triangles). The gray lines are fitted to the low and high temperature profiles to estimate  $T_g$ . The green and red vertical lines are shown to highlight the differences in predicted  $T_g$  due to differences in cooling rates.

Figure 6 shows the variation of density with respect to the temperature as calculated from the slowest annealing simulation study (0.01K/ps). Based on the results, the room temperature density was observed to be  $\sim 1.17 \text{ gm/cm}^3$  and matches with the one estimated using simulations performed on the initial BMI structure (Figure 3(b)). Given the reported densities of the individual monomers at room temperature ( $1.07 \text{ g/cm}^3$  for *O,O'* diallyl bisphenol A [19] and  $1.34 \text{ g/cm}^3$  for 4,4'-bismaleimidodiphenyl methane [20]), In addition, it is expected that the overall system density should increase with curing (cross-linking) due to volume shrinkage, as seen in other studies as well [21], and will be investigated in the future. Thus, the value of  $1.17 \text{ gm/cm}^3$  for un-crosslinked mixture is in excellent agreement with the reported value of  $1.23 \text{ gm/cm}^3$  for cured matrix based on BMPM and DABPA [22], assuming the potential volume shrinkage of the matrix during curing.

Figure 7 plots the volume as a function of temperature and identifies the importance of cooling rates on the structural relaxation of the molecules. Here, the average volume for each plotted data point was calculated using histogram binning method with  $\Delta T$  of 5 Kelvin for annealing simulations. The volume calculation strategy for equilibrium simulations has been mentioned in a previous sub-section (refer to second set of simulations). From the figure, it is clear that a higher cooling rate (0.25K/ps; red squares) results in larger system volume at low temperature and

leads to a higher value of fitted glass transition temperature ( $T_g \sim 490$  K). At higher rates, the system has lower chances to respond to the non-equilibrium surrounding changes (such as continuous cooling) and thus leads to *frustration* in molecular relaxation [23]. In such cases, the volume further reduces at low temperatures due to reduction in free volume and physical aging. On the contrary, relatively lower cooling rates (0.01 K/ps; green circles) lead to better equilibrated structures and matches well with the data from equilibrium simulations (blue triangles).

It should be pointed out that the reported results for volume variation with temperature and the predicted glass transition temperatures are for studied BMI-monomer mixtures. It is expected that after curing, the cross-linked structure will exhibit significantly slower response to cooling rate due to chain connectivity and large molecular weight, and thus is expected to exhibit significantly higher glass transition temperatures and provide better comparison between simulations and experimental results ( $T_g \sim 525$  K) [22].

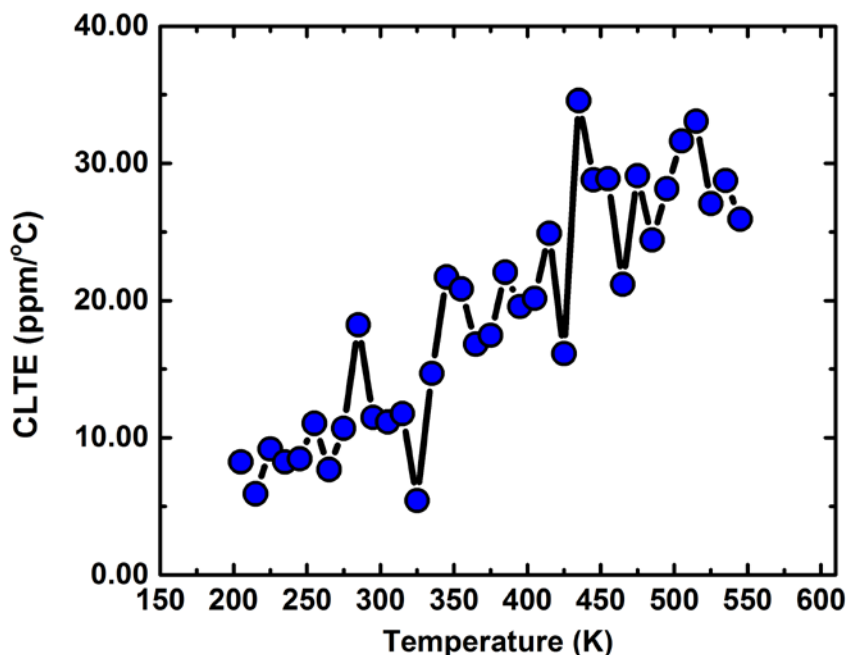


Figure 8: Plot of coefficient of linear thermal expansion (in ppm/°C) as a function of temperature for the BMI matrix components, as calculated from slow annealing simulation run.

The coefficient of thermal expansion is one of many important thermodynamic properties in composite materials which finds its use in several problems of practical importance, such as lattice mismatch issues at interfaces between layers (films) of different materials (composites, hybrids, metals, etc.). The coefficient of volume thermal expansion (CVTE) is defined as [24]

$$\alpha_i = \frac{1}{V} \left( \frac{\partial V}{\partial T} \right)_p \quad (1)$$

where  $V$ ,  $T$ , and  $P$ , are the volume, temperature, and pressure of the system, respectively. For isotropic materials, the coefficient of linear thermal expansion (CLTE),  $\beta$ , is related to  $\alpha$  as

$$\beta = \frac{\alpha}{3} \quad (2)$$

Figure 8 shows the CLTE as a function of temperature for the studied BMI-5292 matrix, as calculated from volume-temperature data from slower annealing simulations. Here, a finite difference method was used to evaluate  $\beta$  at each temperature  $T$  using following equation.

$$\beta_T = \frac{V_{T'} - V_T}{3 \times V_T \times (T' - T)} \quad (3)$$

where,  $T' > T$  and  $T' - T$  was fixed to be 5 Kelvin (similar to volume vs. temperature estimation as reported above).

First, the figure shows that CLTE is not constant with temperature but seems to be increasing linearly (with fluctuations) over the range of 300 K from 10—30 ppm/°C, although one could argue the validity of its linearity dependence. Additional independent runs are required to decrease the statistical fluctuations and verify the linear behavior. While these reported values are smaller than reported values for EPON based resins [21], the estimated values are in fair agreement with CLTEs of other bismaleimide resins based systems (Unpublished work; please visit cited URLs for comparison purposes) [22, 25].

### Thermal Conductivity of BMI Matrix

The thermal conductivity of the BMI matrix was calculated using NEMD simulations from a slab-like geometry based on Fourier law approach [26]. First, an elongated slab was created by replicating the equilibrated BMI-5292 matrix 6 times along  $z$ -direction, followed by further equilibration in NPT ensemble for 500 ps. The schematic as well as the associated nomenclature of NEMD simulations for the equilibrated elongated slab is shown in Figure 9.

As seen from the figure, the outer edges of the elongated slab (1 nm) were fixed and the adjacent  $\sim 2$  nm bins were employed as hot and cold thermostats, respectively. Two methodologies, based on constant temperature and constant energy flux, were employed to calculate the thermal conductivity as well as investigate their potential variation in predicted  $\lambda$  values. For constant temperature techniques (i.e., keeping the hot and cold regions at a certain temperature), several different heating/cooling mechanisms were used, such as Nose-Hoover thermostat, Berendsen thermostat and temperature (velocity) rescaling thermostat as implemented in LAMMPS package. For these techniques, the hot region was kept at 350 K while the cold region was kept at 250 K during the course of NEMD simulations. In order to keep the regions at their specified temperatures, energy was continuously added and taken off from the hot and cold regions, respectively. NVE ensemble was employed for un-thermostated regions



(see Figure 9). For constant energy flux simulations, a flux of 3 kcal/mol/ps was added to hot (subtracted from cold) thermostats.

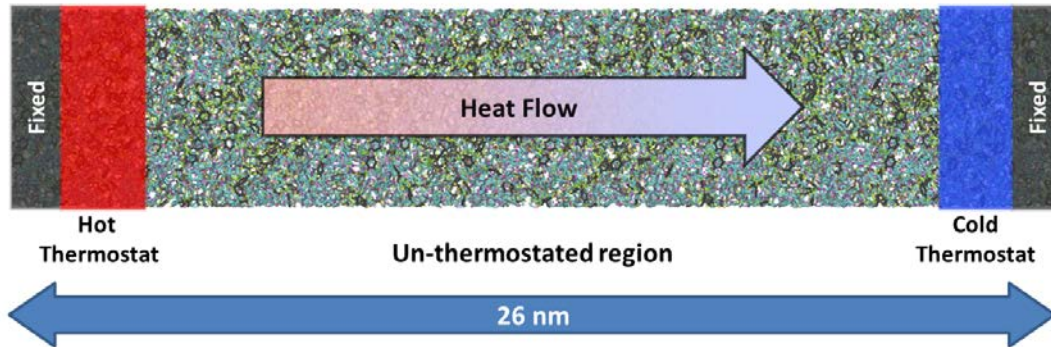


Figure 9. Schematic of NEMD simulations performed on BMI-matrix to calculate its thermal conductivity using different constant temperature and constant energy flux schemes as discussed in text.

Irrespective of the applied methodology, a temperature gradient profile is established along the elongated slab direction in steady-state. The temperature gradient can then be calculated by dividing the slab into pre-defined number of small slabs with equal thickness (4 Å for our case) and calculating the temperature of each bin using the following equation.

$$T_i = \frac{1}{3N_i k_B} \sum_{k=1}^{N_i} m_k v_k^2 \quad (4)$$

where,  $N_i$  is number of atoms in  $i^{\text{th}}$  slab; and  $m_k$  and  $v_k$  correspond to atomic mass and velocity of atom  $k$ , respectively.

For all cases, initial simulations were run for about 1 ns in order to achieve steady state for heat flow. Once the steady-state was achieved, further simulations were run for 1.5 ns for data collection. The thermal conductivity was then calculated using the following equation

$$\lambda = \frac{Q/A\Delta t}{dT/dz} \quad (5)$$

where,  $Q/A\Delta t$  is the heat flux across the slab and  $dT/dz$  is the temperature gradient in steady-state.

Figure 10 shows the cumulative heat as a function of simulation time for different investigated thermostats. The initial non-linearity is suggestive of the temperature evolution within the system of interest. Once steady-state is reached (~1ns), the cumulative heat input becomes linearly proportional to the simulation time. From the overlapping data, the figure clearly suggests that there was no noticeable difference (< 5-8%) in heat flux because of different applied thermostats. The total heat flux values (as obtained from the slope) are also tabulated in Table I for relative comparison.



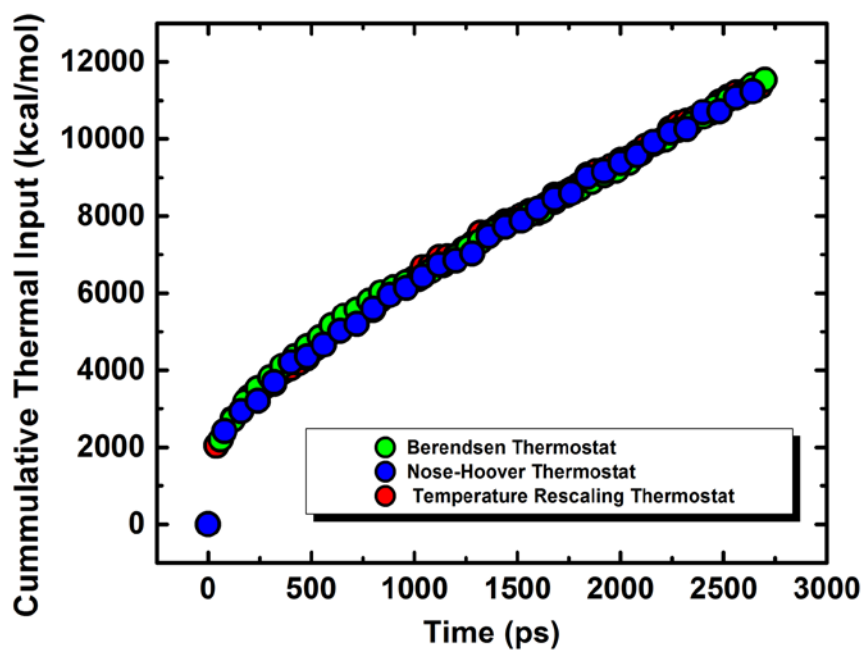


Figure 10. Plot of cumulative heat added into hot thermostat as function of time for different studied thermostats. The color scheme for different simulations is shown in legends.

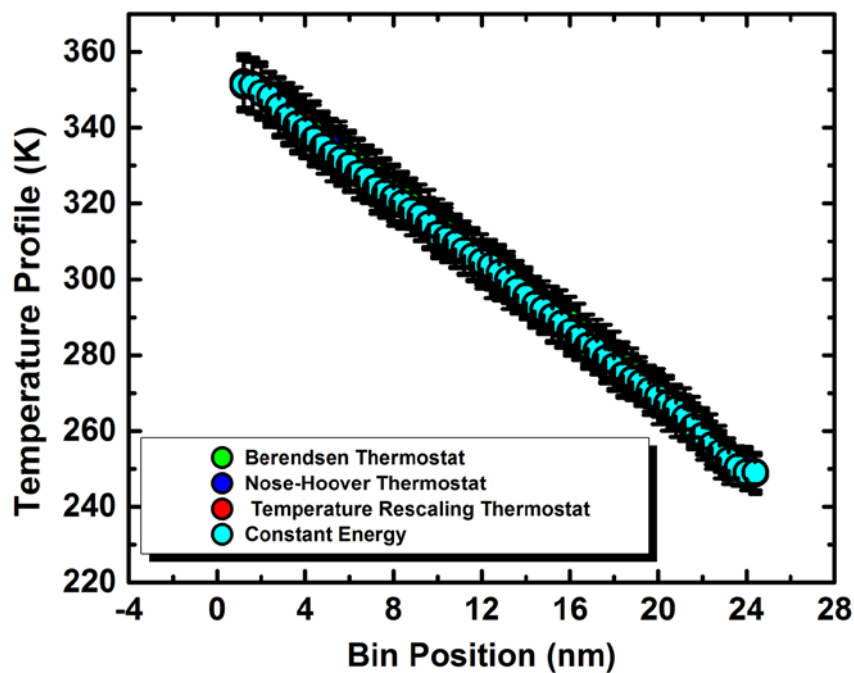


Figure 11. Plot of steady-state temperature profile along elongated slab direction within un-thermostated region (See Figure 9 for the schematic representation). The color scheme for different simulations is shown in legends. All colors but cyan are not readily visible due to overlapping of the data points as well due to the linear temperature profile trend.

TABLE I: COMPARISON OF THERMAL CONDUCTIVITY AS CALCULATED FROM DIFFERENT INVESTIGATED METHODS

Thermostat Scheme	Heat Flux (kcal/mol/ps)	Area (Å <sup>2</sup> )	$dT/dz$ (K/Å)	Thermal Conductivity ( $\lambda$ ) (W/m-K)
Berendsen	2.88	2359.4	0.46	0.187±0.002
Nose-Hoover	3.12	2359.4	0.46	0.206±0.002
Temp. Rescaling	2.93	2359.4	0.44	0.195±0.002
Constant Energy	3.00	2359.4	0.43	0.203±0.002

Figure 11 plots the steady-state temperature profile of the BMI-5292 matrix along the heat flux direction. In addition to the different investigated thermostats, a temperature profile from constant energy NEMD simulations is also plotted. Similar to Figure 10, the estimated temperature gradients (see Table I) were found to be indifferent to applied thermostats (under same boundary conditions of 250 K and 350 K). Table I also shows the estimated values of thermal conductivity (using eq. 2) for BMI-matrix monomer systems. All the estimated values are within ~7% of each other. The indifferences in estimated values due to thermostats are reflective of the fact that thermostats at the boundaries do not play a significant role in determining thermal conductivity of the system. Such observations have been reported before as well for silicon nanowires, where a detailed investigation was carried out to specifically observe these differences [27]. It should be noted that the reported values are in good agreement with simulations performed on other ‘amorphous’ epoxy monomers mixtures; EPON-862 and DETDA [28].

While it is not pertinent to compare the estimated  $\lambda$  values for monomer mixture with  $\lambda$  of the ‘cross-linked’ BMI-5292 matrix [29], it is imperative to put the estimated values in perspective. Previously, we have estimated that ~90% crosslinking of amorphous and disordered epoxy matrix based on EPON-862 and DETDA increased the thermal conductivity by ~50% from their amorphous un-cross-linked counterparts [28]. Recently, it has been reported that thermal conductivity of amorphous polymers (polythiophenes) can be significantly tuned (up to ~4.4 W/m-K) by increasing the orientational order, even without order crystallinity [30]. Given the planar nature of both the monomers and the observation that one of the monomers (BMPPM) exhibit crystallinity (melting point 156 °C) [31], a similar increase could potentially be possible for the matrix of interest. The modeling of crosslinking and the effect of orientational order on thermal conductivity will be undertaken in the future.

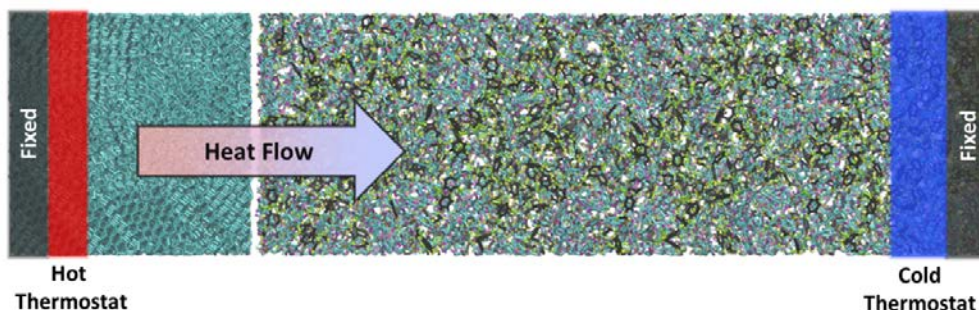


Figure 12: Schematic of NEMD simulations performed to model and predict interface thermal conductance at matrix-fiber interface as discussed in text.

## Interface Thermal Resistance across Carbon-Fiber/Matrix Interface

Figure 12 shows the representative schematic for NEMD simulations employed for the calculation of interface thermal conductance across the BMI-matrix fiber interface. Three different amorphous forms (as retrieved from equilibrium simulations of amorphous carbon) of carbon fiber were used to model the matrix-fiber interface. We will refer to them as E0, E2 and E2, corresponding to cooling rates of 1E0 K/ps, 1E1 K/ps and 1E2 K/ps, respectively. Similar to previous discussion and as seen in Figure 12, the outside edges were fixed for these calculations as well. The adjacent 1.5 nm near both edges were used as hot and cold thermostat regions. Similar to the BMI thermal conductivity simulations, three difference thermostats (Nose-Hoover, Berendsen, and temperature (velocity) rescaling) were used in hot and cold regions to control the temperatures of 350K and 250K, respectively. As discussed prior, when the energy is dumped in (or taken out) into hot (from cold) thermostat, a steady-state temperature profile is generated over time within the system of interest. In addition, near the interface, a temperature discontinuity develops due to mismatch in vibrational properties of the two media. For our system of interest, steady state was reached  $\sim 1$ ns after which production runs of 2 ns were run to estimate the temperature profile as well as temperature discontinuity at the interface using the binning method discussed above.

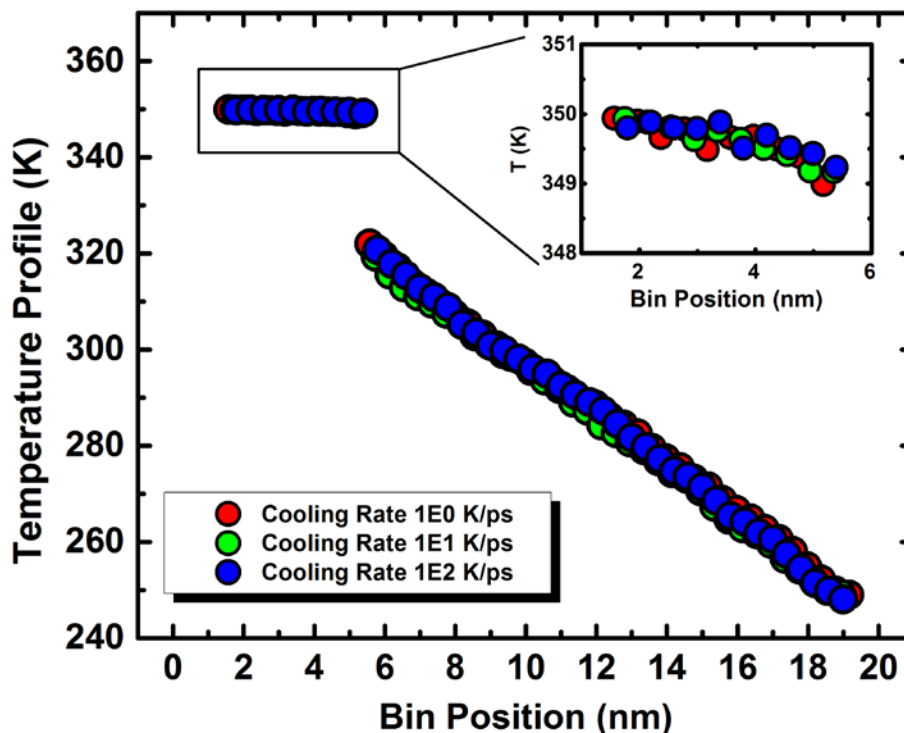


Figure 13: Plot of steady-state temperature profiles for fiber-matrix composite systems (corresponding to different cooling rates), as employed for interface thermal conductance calculations. The plot shows the cases for Berendsen thermostat simulation cases. Other cases are not shown for the sake of clarity. The inset highlights the temperature decay in amorphous carbon region for better clarity.

The interface thermal conductance was then calculated using following equation.

$$\Lambda = \frac{Q}{A\Delta T} \quad (6)$$

where  $\Lambda$ ,  $A$ , and  $\Delta T$  correspond to interface thermal conductance, cross-sectional area, and temperature discontinuity at the matrix fiber-interface. In these simulations, a timestep of 0.2 fs was employed to keep the total energy of the system conserved during the course of the simulation.

Figure 13 shows the steady-state temperature gradient profiles for three of the nine studied systems. It can be observed clearly that: a) temperature gradients are linear in matrix region; b) they are relatively less within the carbonaceous region; and c) there exists a clear temperature discontinuity at the interface of the matrix and carbonaceous region, as discussed previously.

The large temperature gradient within the matrix is indicative of its low thermal conductivity and matches with the calculations performed on the pristine matrix as discussed before in detail (please refer to Table I). On the other hand, the relatively lower slope (for the same amount of heat flux; please see Table II for heat flux values) as seen from inset of Figure 13 suggests a relatively larger thermal conductivity of the amorphous matrix. Based on a linear fit to the amorphous carbon data, the thermal conductivity within the carbonaceous region can be estimated to be ~3-4 W/m-K. We should point out that the value range is rather qualitative due to less number of data points in the linear fitting within the amorphous carbon region.

TABLE II: OBSERVED HEAT FLUX AND ASSOCIATED TEMPERATURE DROP VALUES AS STUDIED FOR DIFFERENT COMBINED FIBER-MATRIX SYSTEMS WITH DIFFERENT THERMOSTATS

Thermostat Scheme	Heat Flux (kcal/mol/ps)	Area (Å <sup>2</sup> )	$\Delta T$ (K)
<b>Cooling Rate 1 K/ps</b>			
Nose-Hoover	3.38	2728.921	29.19
Berendsen	3.22	2728.921	28.22
Velocity Rescaling	3.22	2728.921	29.95
<b>Cooling Rate 10 K/ps</b>			
Nose-Hoover	3.28	2728.921	30.55
Berendsen	3.15	2728.921	30.40
Velocity Rescaling	3.46	2728.921	31.71
<b>Cooling Rate 100 K/ps</b>			
Nose-Hoover	3.39	2728.921	29.65
Berendsen	3.31	2728.921	29.07
Velocity Rescaling	3.31	2728.921	31.01

Based on the data in Figure 13, the linear region was fit to calculate the temperature drop at the interface. The temperature gradients were estimated to be  $\sim 30 \pm 2$  K for all studied cases (irrespective of applied thermostat and nature of carbonaceous region). These values are reported in Table II along with the estimated heat flux and cross-sectional area of the interface. The similar values of temperature drop are indicative of the observation that thermostats do not play an important role towards determination of thermal energy exchange at the interface. Furthermore, it also suggests that the energy exchange is predominantly governed by dispersive van der Waals interactions. As the local atomic structure of the amorphous/nano-crystalline carbonaceous region is not of noticeable significance towards thermal energy exchange, as it is the interface which serves as a bottleneck for efficient thermal conduction.

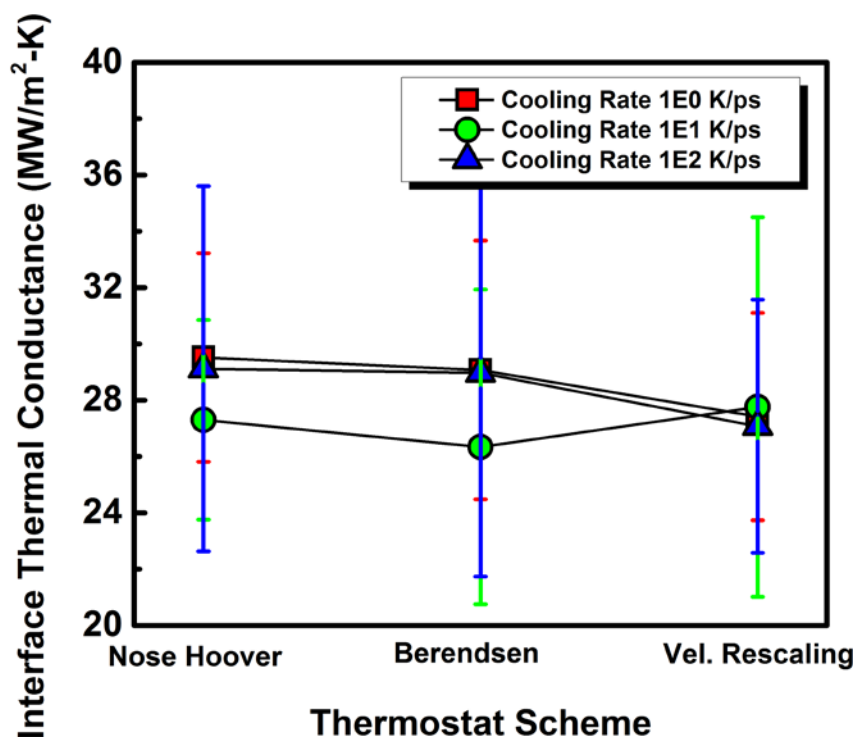


Figure 14. Predicted values of interface thermal conductance in units of  $\text{MW/m}^2\text{-K}$  for all studied combined matrix-fiber systems with respect to different applied thermostats. Color scheme is shown in legends within the figure.

The calculated interface thermal conductance values (as calculated from eq. 6) are shown in Figure 14 for different studied cases. As seen from the figure, for all cases, the interface conductance values were found to be in a narrow range of  $\sim 26.5$ – $29.5$   $\text{MW/m}^2\text{-K}$  with a relative average error of  $\sim 4$   $\text{MW/m}^2\text{-K}$ . The primary source of error in the investigated values arose from the error in heat flux calculations and is expected to be reduced by running longer simulations [32]. We should note that the observed values are in good agreement with other reported studies involving carbon (CNTs)-

matrix (epoxy, octane, polymers) interfaces which interact through van der Waals interactions [33-38].

## SUMMARY AND CONCLUSIONS

Using molecular dynamics simulations, we have investigated the thermo-physical properties of BMI-5292 matrix monomer mixtures and its interface properties with amorphous carbon fiber. To the best of authors' knowledge, this is the first investigation to focus on BMI-5292 matrix system using full atomistic resolution and is modeled using general amber force field. To validate the force-field, several thermo-physical property values were estimated and were found to be in good agreement with the available experimental literature.

Future research will build on this study and will model and investigate crosslinking phenomenon in this matrix system and how different thermal and mechanical properties are affected by the degree of crosslinking. In parallel, graphitized carbon interfaces will be created to model the effect of degree of graphitization and its orientation on the interface thermal conductance with cross-linked BMI-5292 matrix.

## ACKNOWLEDGEMENTS

VV acknowledges US Air Force Office of Scientific Research (AFOSR) for the financial support (LabTask: 3002BR3P, Program Manager: Dr. B. L. Lee) and Department of Defense Supercomputing Research Center (ERDC-DSRC) for computational resources to carry out the simulations. VV also thanks Dr. Gregory Ehlert and Dr. Keith Slinker for their insightful discussions during the course of the study.

## REFERENCES

1. Conforti, P. F., M. Prasad, and B. J. Garrison. 2008. "Elucidating the Thermal, Chemical, and Mechanical Mechanisms of Ultraviolet Ablation in Poly(Methyl Methacrylate) Via Molecular Dynamics Simulations." *Acc. Chem. Res.*, 41(8): 915-924.
2. Lippert, T., and J. T. Dickinson. 2003. "Chemical and Spectroscopic Aspects of Polymer Ablation: Special Features and Novel Directions." *Chem. Rev.*, 103(2): 453-486.
3. Frenkel, D., and B. Smit. 2001. *Understanding Molecular Simulation: From Algorithms to Applications*. London: Academic press.
4. Cho, D., and L. T. Drzal. 2003. "Effect of Thermal Cure on the Fluorescence of Matrimid™ 5292 Bismaleimide Resin." *J. Mater. Sci. Lett.*, 22(6): 459-461.
5. "Materials Studio," San Diego: Accelrys Software Inc.,
6. Dauber-Osguthorpe, P., V. A. Roberts, D. J. Osguthorpe, J. Wolff, M. Genest, and A. T. Hagler. 1988. "Structure and Energetics of Ligand Binding to Proteins: Escherichia Coli Dihydrofolate Reductase-Trimethoprim, a Drug-Receptor System." *Proteins: Struct. Funct. Bioinform.*, 4(1): 31-47.
7. Sun, H., S. J. Mumby, J. R. Maple, and A. T. Hagler. 1994. "An Ab Initio Cff93 All-Atom Force Field for Polycarbonates." *J. Am. Chem. Soc.*, 116(7): 2978-2987.



8. Wang, J., R. M. Wolf, J. W. Caldwell, P. A. Kollman, and D. A. Case. 2004. "Development and Testing of a General Amber Force Field." *J. Comput. Chem.*, 25(9): 1157-1174.
9. Cornell, W. D., P. Cieplak, C. I. Bayly, I. R. Gould, K. M. Merz, D. M. Ferguson, D. C. Spellmeyer, T. Fox, J. W. Caldwell, and P. A. Kollman. 1995. "A Second Generation Force Field for the Simulation of Proteins, Nucleic Acids, and Organic Molecules." *J. Am. Chem. Soc.*, 117(19): 5179-5197.
10. Frisch, M., G. Trucks, H. B. Schlegel, G. Scuseria, M. Robb, J. Cheeseman, G. Scalmani, V. Barone, B. Mennucci, and G. Petersson. 2009. "Gaussian 09, Revision A. 02, Gaussian Inc.," Wallingford, CT.
11. Dupradeau, F.-Y., A. Pigache, T. Zaffran, C. Savineau, R. Lelong, N. Grivel, D. Lelong, W. Rosanski, and P. Cieplak. 2010. "The Red Tools: Advances in Resp and Esp Charge Derivation and Force Field Library Building." *Phys. Chem. Chem. Phys.*, 12(28): 7821-7839.
12. Plimpton, S. 1995. "Fast Parallel Algorithms for Short-Range Molecular Dynamics." *J. Comput. Phys.*, 117(1): 1-19.
13. Darden, T., D. York, and L. Pedersen. 1993. "Particle Mesh Ewald: An N·Log (N) Method for Ewald Sums in Large Systems." *J. Chem. Phys.*, 98(12): 10089-10092.
14. Humphrey, W., A. Dalke, and K. Schulten. 1996. "Vmd: Visual Molecular Dynamics." *J. Mol. Graph.*, 14(1): 33-38.
15. Tersoff, J. 1989. "Modeling Solid-State Chemistry: Interatomic Potentials for Multicomponent Systems." *Phys. Rev. B.*, 39(8): 5566-5568.
16. Brenner, D. W., O. A. Shenderova, J. A. Harrison, S. J. Stuart, B. Ni, and S. B. Sinnott. 2002. "A Second-Generation Reactive Empirical Bond Order (Rebo) Potential Energy Expression for Hydrocarbons." *J. Phys.: Condens. Matter*, 14(4): 783.
17. Allen, M. P., and D. J. Tildesley. 1989. *Computer Simulation of Liquids*. Oxford university Press.
18. Singh, U. C. K., P. A. 1984. "An Approach to Computing Electrostatic Charges for Molecules." *J. Comput. Chem.*, 5(2): 129-145.
19. [https://www.chemicalbook.com/ChemicalProductProperty\\_EN\\_CB9460153.htm](https://www.chemicalbook.com/ChemicalProductProperty_EN_CB9460153.htm)
20. Usman, A., H.-K. Fun, H.-L. Zhu, and G. Ke. 2003. "Bis(4-Maleimidophenyl)Methane." *Acta Crystallogr E*, 59(5): o652-o653.
21. Varshney, V., S. S. Patnaik, A. K. Roy, and B. L. Farmer. 2008. "A Molecular Dynamics Study of Epoxy-Based Networks: Cross-Linking Procedure and Prediction of Molecular and Material Properties." *Macromolecules*, 41(18): 6837-6842.
22. [https://multimedia.3m.com/mws/mediawebserver?mwsId=SSSSSufSevTsZxtUoY\\_ePxtB evUqevTSevTSevTSevTSeSSSSSS--](https://multimedia.3m.com/mws/mediawebserver?mwsId=SSSSSufSevTsZxtUoY_ePxtB evUqevTSevTSevTSeSSSSSS--)
23. Moynihan, C. T., A. J. Easteal, J. Wilder, and J. Tucker. 1974. "Dependence of the Glass Transition Temperature on Heating and Cooling Rate." *J. Phys. Chem.*, 78(26): 2673-2677.
24. Ho, C. Y., and R. E. Taylor. 1998. *Thermal Expansion of Solids*. ASM international.
25. <https://polycomp.mse.iastate.edu/files/2012/2001/2016-Bismaleimide-Resins.pdf>
26. Anderson, C. V. D. R., and K. K. Tamma. 2003. "An Overview of Advances in Heat Conduction Models and Approaches for Prediction of Thermal Conductivity in Thin Dielectric Films." *Int. J. Numer. Method H.*, 14(1): 12-65.
27. Varshney, V., A. K. Roy, D. S. Dudis, J. Lee, and B. L. Farmer. 2012. "A Novel Nano-Configuration for Thermoelectrics: Helicity Induced Thermal Conductivity Reduction in Nanowires." *Nanoscale*, 4(16): 5009-5016.
28. Varshney, V., S. S. Patnaik, A. K. Roy, and B. L. Farmer. 2009. "Heat Transport in Epoxy Networks: A Molecular Dynamics Study." *Polymer*, 50(14): 3378-3385.
29. The authors are not aware of any study which undertook and reported the thermal conductivity of the BMI-5292 matrix.
30. Singh, V., T. L. Bougher, A. Weathers, Y. Cai, K. Bi, M. T. Pettes, S. A. McMenamin, W. Lv, D. P. Resler, T. R. Gattuso, et al. 2014. "High Thermal Conductivity of Chain-Oriented Amorphous Polythiophene." *Nat. Nanotech.*, 9(5): 384-390.

31. Ijima, T. 1996. "Bismaleimide Resins," Salamone, J. C., *Polymeric Materials Encyclopedia*. CRC Press, p. 643.
32. Due to the employed timestep of 0.2 fs on a system ~60,000 atoms, we could only run upto 003 ns with the computational resources in hand.
33. Roy, A. K., B. L. Farmer, V. Varshney, S. Sihn, J. Lee, and S. Ganguli. 2012. "Importance of Interfaces in Governing Thermal Transport in Composite Materials: Modeling and Experimental Perspectives." *ACS Appl. Mater. Interfaces*, 4(2): 545-563.
34. Varshney, V., A. K. Roy, T. J. Michalak, J. Lee, and B. L. Farmer. 2013. "Effect of Curing and Functionalization on the Interface Thermal Conductance in Carbon Nanotube-Epoxy Composites." *JOM-J. Min, Met. Mat. S.*, 65(2): 140-146.
35. Huxtable, S. T., D. G. Cahill, S. Shenogin, L. Xue, R. Ozisik, P. Barone, M. Usrey, M. S. Strano, G. Siddons, M. Shim, et al. 2003. "Interfacial Heat Flow in Carbon Nanotube Suspensions." *Nat Mater*, 2(11): 731-734.
36. Shenogin, S., L. Xue, R. Ozisik, P. Keblinski, and D. G. Cahill. 2004. "Role of Thermal Boundary Resistance on the Heat Flow in Carbon-Nanotube Composites." *J. Appl. Phys.*, 95(12): 8136-8144.
37. Clancy, T. C., and T. S. Gates. 2006. "Modeling of Interfacial Modification Effects on Thermal Conductivity of Carbon Nanotube Composites." *Polymer*, 47(16): 5990-5996.
38. Bryning, M. B., D. E. Milkie, M. F. Islam, J. M. Kikkawa, and A. G. Yodh. 2005. "Thermal Conductivity and Interfacial Resistance in Single-Wall Carbon Nanotube Epoxy Composites." *Appl. Phys. Lett.*, 87(16): 161909.

## Appendix B. Gold Nanorod Temperature Sensors

# High-Resolution Mapping of Thermal History in Polymer Nanocomposites: Gold Nanorods as Microscale Temperature Sensors

W. Joshua Kennedy,<sup>†,‡</sup> Keith A. Slinker,<sup>†,‡</sup> Brent L. Volk,<sup>‡</sup> Hilmar Koerner,<sup>‡</sup> Trenton J. Godar,<sup>§,‡</sup> Gregory J. Ehlert,<sup>‡</sup> and Jeffery W. Baur<sup>\*,‡</sup>

<sup>†</sup>Universal Technology Corporation, Materials and Manufacturing, 1270 North Fairfield Road, Dayton, Ohio 45433, United States

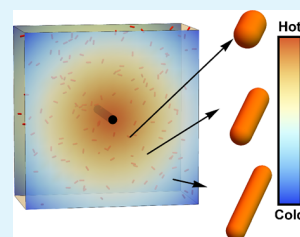
<sup>‡</sup>Air Force Research Laboratory, Materials and Manufacturing Directorate (AFRL/RXCC), Wright-Patterson Air Force Base, Ohio 45429, United States

<sup>§</sup>University of Dayton Research Institute, 300 College Park, Dayton, Ohio 45469, United States

## Supporting Information

**ABSTRACT:** A technique is reported for measuring and mapping the maximum internal temperature of a structural epoxy resin with high spatial resolution via the optically detected shape transformation of embedded gold nanorods (AuNRs). Spatially resolved absorption spectra of the nanocomposites are used to determine the frequencies of surface plasmon resonances. From these frequencies the AuNR aspect ratio is calculated using a new analytical approximation for the Mie-Gans scattering theory, which takes into account coincident changes in the local dielectric. Despite changes in the chemical environment, the calculated aspect ratio of the embedded nanorods is found to decrease over time to a steady-state value that depends linearly on the temperature over the range of 100–200 °C. Thus, the optical absorption can be used to determine the maximum temperature experienced at a particular location when exposure times exceed the temperature-dependent relaxation time. The usefulness of this approach is demonstrated by mapping the temperature of an internally heated structural epoxy resin with 10  $\mu\text{m}$  lateral spatial resolution.

**KEYWORDS:** gold nanorods, polymer nanocomposites, temperature sensing, thermal reshaping, structural composites



## ■ INTRODUCTION

Gold nanorods (AuNRs) are known to change their shape from cylindrical to ovoid or spheroid under the influence of both environmental heat and direct laser irradiation.<sup>1–8</sup> This thermal shape transformation leads to a correlation between the temperature of a gold nanorod and its optical properties, which are dominated by shape-dependent plasmon resonances. The shape change is primarily driven by the competition between surface energy minimization across both sides of the interface and recrystallization within a surface melt layer (or virtual melt).<sup>6,8–11</sup> The exact mechanism of the shape transformation of AuNRs is not fully understood, and no analytical expression exists to describe the characteristic relaxation time.

AuNRs are reshaped to an extent which depends on a number of factors, including the absolute size of the particle,<sup>12–15</sup> crystal structure and defects,<sup>2,11,16,17</sup> and the nature of the interface with the surrounding medium.<sup>3,15,18–20</sup> Because thermal reshaping is strongly dependent on the nanorod's environment, the rate and amplitude of the shape change at a particular temperature can vary dramatically. For example, AuNRs that have been stabilized by enclosures of metals or oxides can have surface melting onsets that differ by hundreds of degrees from uncoated rods.<sup>21–23</sup> Moreover, when the surrounding matrix properties change upon heating, the correlation between temperature and spectra becomes more complicated. Recently Liu et al. observed that, when held at

elevated temperatures for extended times, AuNRs in poly(methyl methacrylate) (PMMA) evolve asymptotically toward a final shape that is between the as-grown cylinder and the thermodynamically favorable spheroid.<sup>4</sup> Similar observations have been made by Ng and Cheng<sup>5</sup> as well as Petrova et al.<sup>7</sup> Even after many days of heating, the rods in PMMA nanocomposites did not transform completely to spheres. Liu et al. demonstrated the usefulness of the temperature-dependence of the final nanorod shape by using a thermal gradient to produce a color gradient in a composite film,<sup>4</sup> but they did not attempt to quantify the temperature gradient in the film via the nanorod spectra. In this work, we have developed a technique that enables the microscale, ex situ measurement of temperature within a polymer nanocomposite by exploiting this thermally induced shape change. We calibrate the temperature response of the rods by measuring their shape after long isothermal holds while accounting for changes in the local dielectric constant. We then use this calibration to determine the maximum temperature experienced within a nanocomposite with a lateral spatial resolution of 10  $\mu\text{m}$ . We demonstrate the usefulness of this technique by applying it to measure the thermal gradients inside a structural epoxy resin containing a single 6  $\mu\text{m}$  carbon fiber that is electrically heated.

**Received:** May 13, 2015

**Accepted:** November 30, 2015

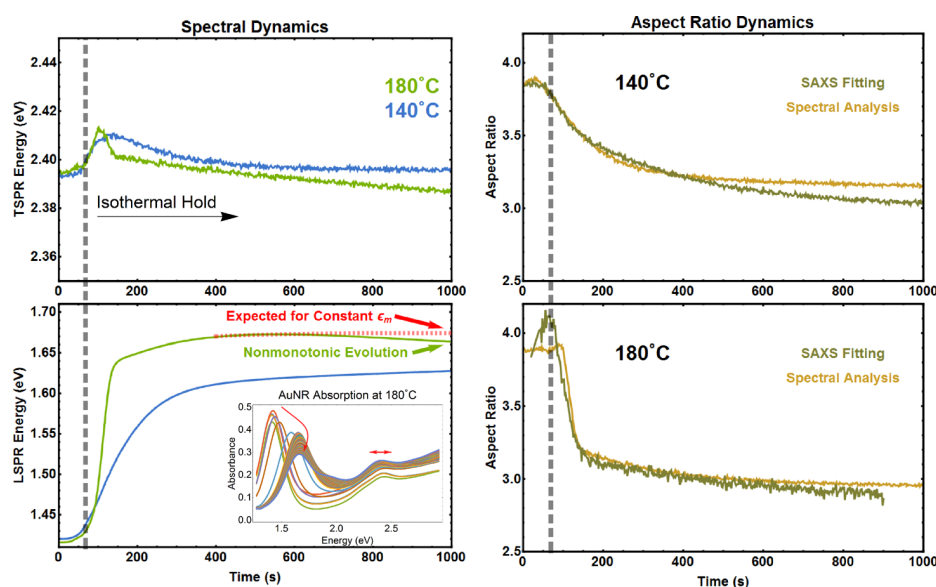


**Figure 1.** Examples of the spectral characteristics necessitating the new analytical approach presented here. (Left) SPR peak positions as a function of time for two different isothermal holds. The vertical dashed line represents the end of the initial heating ramp period. The inset shows a subset of the absorption spectra at 180 °C. (Right) Aspect ratios as a function of time determined simultaneously via SAXS and spectroscopic analysis for the same samples.

The same approach is extendable to much finer spatial resolutions via improved optical methods, and it may be expanded to larger temperature ranges and alternative material systems by using different nanoparticles.

## SPECTROSCOPIC ANALYSIS

At ~40 nm in length, the rods in our AuNR-Epoxy are small enough to treat with the dipole approximation (ignoring the size-dependent dielectric correction) without consideration of quantum scattering effects.<sup>24–26</sup> Under these conditions, in a nonabsorbing medium, one can calculate the extinction cross section spectrum from the aspect ratio according to Gans' extension of the classical Mie theory. Following the treatment of Eustis and El-Sayed<sup>18</sup> we write the extinction  $\gamma$  as a function of photon energy  $E$  as

$$\gamma(E) = \frac{2\pi N V \epsilon_m^{3/2} E}{3hc} \sum_j \frac{\epsilon_2}{P_j^2 \left[ \left( \epsilon_1 + \frac{1-P_j}{P_j} \epsilon_m \right)^2 + \epsilon_2^2 \right]} \quad (1)$$

where  $N$  is the number of scatterers,  $V$  is the volume of each scatterer, and  $\epsilon_1$  and  $\epsilon_2$  are the real and imaginary dielectric constants of the scatterer, respectively. The nonabsorbing surrounding medium is considered to have a frequency-independent, real dielectric constant  $\epsilon_m$ . The  $P_j$  are three depolarization factors which depend only on the aspect ratio  $a$ . These factors lead to two peaks in the absorption spectrum corresponding to the surface plasmon resonances (SPRs) parallel ( $E_L$ ) and perpendicular ( $E_T$ ) to the rod axis. Others have analyzed AuNR absorption spectra using linear approximations of  $E_L(a; \epsilon_m)$ , and have ignored the small but measurable changes in  $E_T$ .<sup>18,27</sup> However, in complex systems the changes in local dielectric can obfuscate the relationship between the absorption spectrum and the temperature. In an epoxy nanocomposite (AuNR-Epoxy), for example, the dielectric constant of the matrix can change as a result of chemical reactions (such as cross-linking), glass transitions, and

photothermal degradation. As demonstrated in this work, this makes a direct, unambiguous correlation between absorption peak position and temperature impossible. The collective influence of a simultaneously changing dielectric and aspect ratio is apparent in Figure 1, which shows the evolution of the transverse (TSPR) and longitudinal (LSPR) resonance energies in AuNR Epoxy for isothermal holds at 140 and 180 °C (as measured by the total extinction in optical transmission).

The SPR peak positions in Figure 1 are identified by fitting each spectral region to a Gaussian line shape on top of a locally linear background. At lower temperatures the LSPR shifts to higher energies as expected, but at temperatures above about 150 °C the LSPR first blue shifts and then slightly red shifts. If the longitudinal peak were used as a direct measure of nanorod morphology in this sample then we would conclude that the nanorods were first contracting and then lengthening. This is not consistent with the currently accepted physical picture of the shape transformation process. To illustrate this departure from expected behavior we have included a dashed red line in the 180 °C curve corresponding to a simple exponential fit to the data between 150 and 400 s. This line represents the LSPR evolution that would be expected based on the current literature on the subject.

To understand why the LSPR deviates from this expected behavior, it is helpful to analyze the concurrent changes in the TSPR. The TSPR peak is much broader than the LSPR peak, primarily because of the presence of spherical particles in the starting material, inhomogeneous size distribution, and homogeneous broadening from surface scattering. Even so, it is possible to track the very small changes in the TSPR peak position because the uncertainty in the fit parameter is small. The TSPR resonance in each case increases sharply once the target temperature is reached and then begins to gradually decrease. While the spectral shifts are small compared to the peak width, the movement is more apparent when the spectra are stacked on top of each other as in the inset in Figure 1. Again, the nonmonotonic changes in the TSPR peak energy are inconsistent with a model that only considers changes in the

nanorod aspect ratio. To understand this phenomenon, we invoke some general properties of Mie–Gans scattering in gold nanorods as described below. Referring to eq 1, for a particular dielectric environment the longitudinal mode energy  $E_L$  is red-shifted and the transverse mode energy  $E_T$  is blue-shifted as the aspect ratio increases. On the other hand, as  $\epsilon_m$  increases both  $E_L$  and  $E_T$  shift to lower energies (see Figure S1 for an illustration of this effect). The observed evolution of the SPR energies reflects a material system in which the average aspect ratio of the nanorods monotonically decreases but the effective surrounding dielectric does not change monotonically, presumably due to chemical processes in the resin. This behavior is consistent with the well-known cure temperature dependency of the index of refraction in epoxies.<sup>28</sup> At short times, the dielectric constant of the epoxy decreases because of thermal expansion. At longer times, the dielectric constant increases as the degree of cross-linking increases, resulting in a net redshift in both SPR energies.

To develop a more robust mapping between the absorption spectrum and the temperature, we begin with the ansatz that the two physical quantities  $a$  and  $\epsilon_m$  are uniquely determined by the two SPR absorption peaks. Specifically, we use the theoretical  $\gamma(E)$  for aspect ratios between 1 and 5 and local dielectric between 1 and 10, along with values for  $\epsilon_1$  and  $\epsilon_2$  of gold from Johnson and Christy,<sup>29</sup> to find the SPR peak energies  $E_L$  and  $E_T$ . We thereby associate each pair of  $(a; \epsilon_m)$  to the corresponding  $(E_L; E_T)$  and then fit the two resonances to a smooth analytical function of these two variables. We approximate these relationships as  $E_L = f_L(a)g_L(\epsilon_m)$  and  $E_T = f_T(a)g_T(\epsilon_m)$  where  $f$  and  $g$  are polynomials of sufficient order to achieve the desired precision. This can be rewritten as

$$E_i(a, \epsilon_m) = \sum_{j,k} c_{ijk} a^j \epsilon_m^k \quad (2)$$

for each of the two resonances ( $i = L, T$ ). These equations are then solved numerically for a given pair of measured  $(E_L; E_T)$  to simultaneously determine  $a$  and  $\epsilon_m$  from the absorption spectrum. For AuNR-Epoxy, and over a finite range of aspect ratios and dielectric constants, we used 4th order polynomials for  $f$  and  $g$  (see Table S1 for function parameters), and the calculated aspect ratios agree well with independently measured aspect ratios as discussed below.

The average aspect ratios of the nanorods in a subset of the postheated AuNR-Epoxy samples were measured by determining the length and diameter of individual rods in TEM micrographs. A few representative images are shown in the Supporting Information. Unfortunately, the sample geometry and composition makes such measurements difficult, and the dilute concentration makes it impossible to survey large numbers of rods efficiently. Therefore, we used small-angle X-ray scattering (SAXS) to measure the average aspect ratio of a relatively large sample volume. SAXS data were collected at the Advanced Light Source both during and after heating various samples. Absorption spectra were obtained simultaneously and analyzed independently. The agreement between the two independent measurement techniques, shown for two different temperatures in Figure 1, is remarkable. It provides strong validation for the spectral analysis described in this work.

## ■ TEMPERATURE CALIBRATION

The AuNR shape transformation is an irreversible thermodynamic process with an equilibrium state that is determined by

the temperature and by surface and bulk energies. The rate of change of the aspect ratio in AuNR-Epoxy is several orders of magnitude smaller than the thermal motion of the atoms, and at least 1 order of magnitude smaller than the overall heating rate of the samples. Under such quasi-isothermal conditions we expect that the final aspect ratio of the AuNRs will not be strongly dependent on temperature history. Thus, the final aspect ratio of the AuNRs after heating in a given environment is determined uniquely by the maximum steady state temperature experienced (see Figure S2). Because of changes in the local dielectric, the energy of either SPR resonance alone is not enough to determine the temperature. However, if the AuNRs are exposed to elevated temperatures for long periods, then their spectroscopically determined aspect ratios can be used as a measure of the steady state temperature they experienced. We calibrated the AuNR temperature response by holding a set of samples at various uniform temperatures and recording the absorption spectra over time. Inhomogeneous broadening from the size and aspect ratio distribution of our AuNRs leads to resonance peaks that are adequately fit by two Gaussian curves, for  $E_L$  and  $E_T$ , respectively, along with a second-order polynomial background. A few of the spectra for a sample held at 160 °C are shown in Figure 2a along with their spectral fits and the time evolution of the peak positions extracted from the fits (inset). Unlike the previously reported behavior of AuNRs in solution,<sup>5,7</sup> neither  $E_L(t)$  nor  $E_T(t)$  in AuNR-Epoxy are well fit by any simple monotonic function.

Once the time-dependent aspect ratio  $a_T(t)$  is extracted from each set of spectra (by solving eq 2) the relevant dynamics become more apparent. Figure 2b highlights these dynamics by showing  $a_T(t)$  for  $T = 160$  °C. The time evolution is fit well by the biexponential decay

$$a_T(t) = a_1 e^{-t/\tau_1} + a_2 e^{-t/\tau_2} + a_\infty \quad (3)$$

$$a_\infty = a_0 - (a_1 + a_2) \quad (4)$$

where  $a_0$  is the original aspect ratio of our AuNRs and the other terms are fit parameters related to the amplitude ( $a_1, a_2$ ) and rate ( $\tau_1, \tau_2$ ) of the shape transformation at the temperature  $T$ . The shape evolution is not well fit by a single exponential, as shown in Figure 2b. The inset of Figure 2b shows the calculated aspect ratios for a range of temperatures between 100° (blue) and 200 °C (red), each of which is well fit by the same biexponential function with different (temperature-dependent) fit parameters. These fits have  $R^2$  values of over 0.98 and average residuals of less than 0.05%.

The origin of the biexponential character of the shape evolution is not immediately obvious. Much of the previous work has described the process as diffusion-limited, and some have gone so far as to calculate an activation energy for the shape transformation.<sup>1,5–8</sup> Liu et al. proposed that the diffusion of the AuNR capping ligands into the polymer host could play a role in destabilizing the surface, resulting in shape transformations at temperatures above the glass transition temperature of the polymer.<sup>4</sup> Unfortunately, this does not explain why the AuNRs in polymers evolve toward a shape that is not spherical, even at temperatures far above the glass transition of the host. Some computational models have indicated that the reshaping is not diffusion limited, but is governed in part by the barrier to nucleation of new facets.<sup>30</sup> Our results clearly indicate that more than one temperature-dependent phenomenon influences the shape transformation of gold nanorods in polymers. Still, it is unclear whether or not the steady-state



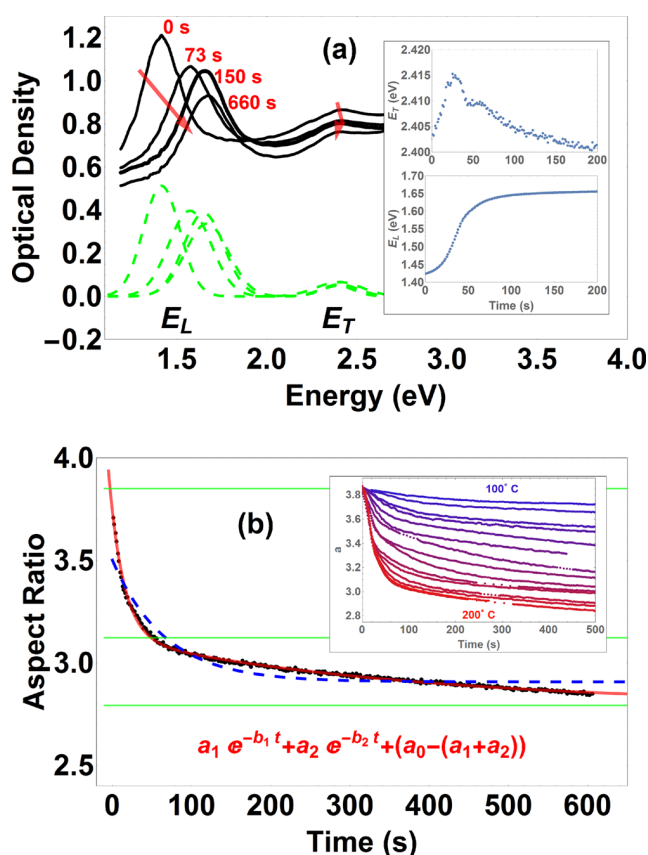


**Figure 2.** Illustration of the process for determining the final aspect ratio using  $T = 160\text{ }^{\circ}\text{C}$  as example data. (a) Raw data (solid black) at four different times along with Gaussian fits (dashed green) with background subtracted. Insets show peak positions as a function of time. (b) Aspect ratio calculated from eq 2 as a function of time. The biexponential fit is the solid red line through the data and the solid blue curve represents the (poor) single exponential fit. The horizontal line at  $a = 3.12$  shows the asymptotic limit of the fast process, while the lower line at  $a = 2.79$  shows the total (fast plus slow) limit corresponding to  $a_{\infty}$ . The horizontal line at  $a_0 = 3.85$  shows the original aspect ratio. The inset shows the aspect ratio evolution in AuNR-Epoxy for a range of temperatures, comprising the calibration data.

aspect ratio determined from the fits actually corresponds to an equilibrium morphology of the nanorods. Previous observations of nanorod spectra during longer heating periods suggest that the rate of shape change reaches a limit,<sup>4–7</sup> and the linear region at long times provides an upper bound on the uncertainty associated with longer heating times. For example, after 600 s at  $180\text{ }^{\circ}\text{C}$  the rate of change ( $da/dt$ ) is only  $1 \times 10^{-10}\text{ s}^{-1}$ . If the evolution asymptotically approaches this linear rate of change, rather than a constant aspect ratio, then it would take an additional 2.4 years of heating at  $180\text{ }^{\circ}\text{C}$  to see a  $1^{\circ}$  difference in the calculated temperature. Because the asymptotic aspect ratio in AuNR-Epoxy is a function of temperature only, the temperature calibration consists of the relationship  $a_{\infty}(T)$ , which is approximately linear ( $R^2 = 0.95$ ) between  $100^{\circ}$  and  $200\text{ }^{\circ}\text{C}$ . In Figure 3, we plot the calibration data along with the linear fit. It is worth noting that this linear fit extrapolates to an asymptotic aspect ratio of 3.73 at a temperature of  $40\text{ }^{\circ}\text{C}$  (the resin processing temperature), which is within 3% of the fit value  $a_0 = 3.85$ . This fit value for  $a_0$  is consistent within  $\pm 0.05$  across all of the calibration samples,

which provides further evidence of the robustness and fidelity of our data analysis technique. The error bars of  $\pm 0.05$  in the calculated aspect ratios shown in Figure 3d are estimated from the uncertainty in the peak assignments from the spectral fits. This is similar to the RMS error of  $\pm 0.053$  in the linear fit of  $a_{\infty}$  and corresponds to an uncertainty in the calculated temperature of  $6.6\text{ }^{\circ}\text{C}$ . If the LSPR, rather than the aspect ratio, were used to measure the temperature then the calibration process in AuNR-Epoxy would be impossible. No asymptotic limit would be found for temperatures above around  $150\text{ }^{\circ}\text{C}$  (see Figure 1), and so the temperature calibration would be ill-defined. At these temperatures, the decrease in  $E_L$  is accompanied by a decrease in the  $E_T$ , which allows decoupling of the dielectric changes from the morphological changes. Without this correction, we would calculate a temperature that is more than  $20\text{ }^{\circ}\text{C}$  lower than the actual temperature. This difference would be temperature- and time-dependent, and the method would predict temperatures in poor agreement with the FLIR measurements and COMSOL calculations as discussed below.

To verify the accuracy of this new temperature measurement we prepared a rectangular slab of AuNR-Epoxy with dimensions  $8.5 \times 37.5 \times 2.2\text{ mm}$  and heated it at one end with a hot stage while cooling at the opposite end with a copper coldfinger immersed in water. We recorded the surface temperature of the sample using an infrared camera. After heating for 3 h the absorption was mapped point by point using the microspectrophotometer. A  $3 \times 10\text{ mm}$  section of the slab near the hot end is shown in Figure 3a, b.

A quantitative comparison between the two methods is obtained by averaging the temperatures in each row in the spectral maps. We calculated the average linear temperature profiles from the colder side to the hot side using both the radiometric and spectroscopic methods and the results are shown in Figure 3c. The temperature maps and average temperature profiles are qualitatively similar, with both measurements indicating hot and cool areas as expected. The average variance between the spectroscopically determined temperatures and a second order interpolation curve through the FLIR temperatures over the measured range is  $7\text{ }^{\circ}\text{C}$ . At higher temperatures ( $>200\text{ }^{\circ}\text{C}$ ) the deviation may be due to the extrapolation of  $a_{\infty}(T)$  beyond the calibration range. At lower temperatures ( $<100\text{ }^{\circ}\text{C}$ ) the stochastic fluctuations in the calculated aspect ratio are large with respect to the overall change in aspect ratio.

## APPLICATION TO AN INTERNALLY HEATED SYSTEM

Finally, we demonstrate the utility of this novel technique by measuring the interior temperature of an internally heated specimen ex situ. We prepared a model system consisting of a single carbon fiber surrounded by AuNR-Epoxy in a traditional dogbone configuration as shown in Figure 4. This single fiber dogbone (SFDB) was heated by delivering electrical power directly to the fiber. We modeled the system with COMSOL, and Figure 4d shows the computational results, from a stationary finite element method (FEM) analysis in COMSOL, which agree qualitatively with our observations via optical radiometry (Figure 4c).

Cross-sections approximately  $1.5\text{ mm}$  thick at different positions along the fiber axis allow the measurement of thermal gradients inside the SFDB via the method described above. Examples of these cross sections are shown in Figure 5. In a computer-automated, point-by-point algorithm the aspect ratios

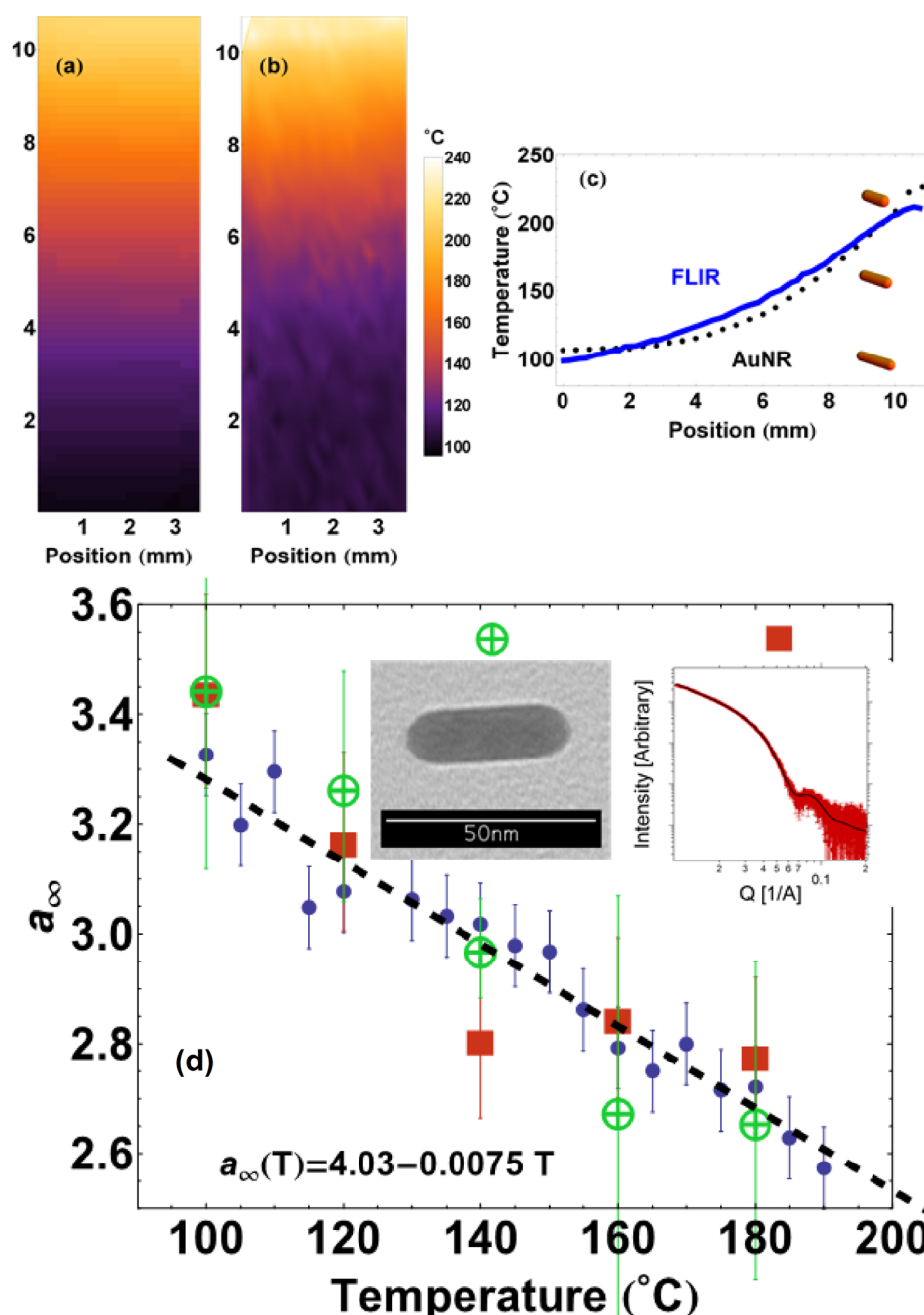


**Figure 3.** Temperature calibration for the nanorod temperature sensors. (a) Infrared image of thermal gradient across a slab of AuNR-Epoxy. (b) Spectrally calculated temperature map of the postheated slab. (c) Average temperature profile in the direction of the gradient for each image. Illustrations of AuNRs with different aspect ratios show the physical scale of their transformation. (d) The final aspect ratio  $a$  (blue circles) from the spectral calculations along with values measured by TEM (green circle crosses) and SAXS (red squares). Insets show example raw data for the TEM and SAXS measurements. The linear fit  $a_\infty(T)$  is shown as a dashed line.

were determined from the absorption spectra and then converted to temperature. Figure 5c shows the spectroscopically determined temperature maps for cross sections A and B from one such sample (see Figure 4). In the low-resolution raster scans, the large-scale temperature profile is evident, but the intrinsic spatial averaging blurs the temperature variations near the fiber where the temperature gradient is the highest. At high resolution, the steep thermal gradients near the fiber are more apparent, but because the fiber is not perfectly perpendicular to the sample surface the signal contains contributions from the projection of the fiber throughout the

1.5 mm sample thickness. This causes an apparent stripe of high temperatures, and the same phenomenon is responsible for the blurring in the magnified visible light image in Figure 5a.

To quantitatively compare the spectral temperature maps with the FEM model, we use the temperature profiles along a straight line through the fiber at cross sections A and B. Figure 5c shows the temperature profiles for the AuNR method along with the FEM predictions for the set of parameters that minimizes the square deviation between the model and the data. The fitted model parameters of total input power ( $P = 1.09$  W), convective heat transfer coefficient ( $h = 11$  W/(m<sup>2</sup>

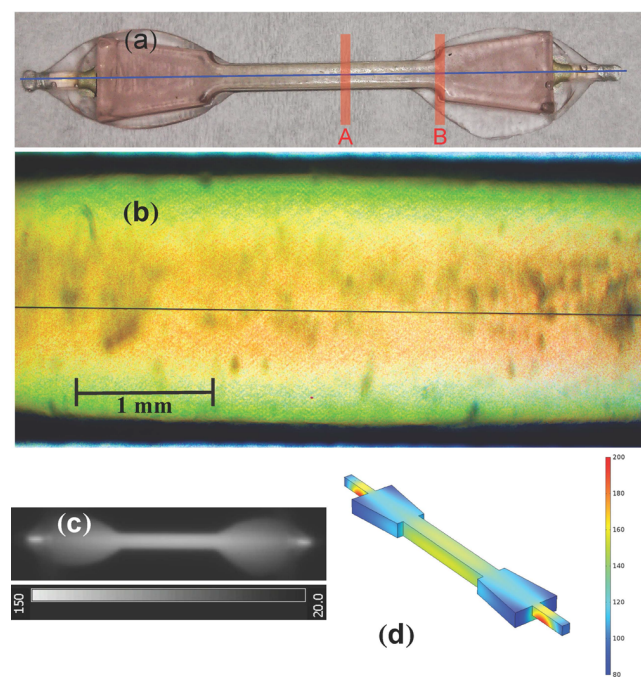


**Figure 4.** SFDB after Joule heating of the carbon fiber. (a) True color image. A solid blue line is drawn to indicate the fiber position, which is barely visible at this magnification. Thick, vertical lines indicate cross sections A and B. (b) Optical micrograph with exaggerated color saturation. (c) FLIR image during heating. (d) Surface temperatures from COMSOL solution.

K)), and epoxy thermal conductivity ( $k = 0.201 \text{ W/(m K)}$ ) result in an average deviation of  $6.4 \text{ }^{\circ}\text{C}$  between the model predictions and the spectrally calculated temperature at each point. Importantly, the same set of parameters is used to fit the temperature profiles at both cross sections. This increases our confidence in the accuracy of the computational model and the fidelity of this new temperature measurement technique. It also demonstrates how one might generate a three-dimensional thermographic map by serially sectioning a sample and creating raster scans at each slice. We note that most of the temperatures in section A exceed the calibration range and are based on an extrapolation of  $a_{\infty}(T)$ , but they still fit the COMSOL model well.

## DISCUSSION

Many other thermometric techniques are limited in their ability to probe spatial temperature distributions in three dimensions at such small scales. Thermocouples are available in sizes of a few microns or less, but spatial mapping with thermocouples is cumbersome and impractical at high resolution.<sup>31,32</sup> Radiometric thermography (infrared imaging) is possible with spatial resolution better than  $10 \text{ }\mu\text{m}$ , but these methods are sensitive only to the sample surface.<sup>33,34</sup> Some specialized techniques for measuring thermal properties of materials at small scales have been developed or improved in the past few years including time-dependent thermoreflectance (TDTR),<sup>35,36</sup> third-harmonic thermoresistance ( $3-\omega$ ),<sup>37,38</sup> and scanning thermal microscopy (SThM).<sup>34,39,40</sup> These techniques also impose significant restrictions on sample geometry and surface conditioning, and quantitative measurements depend on accurate models of thermal transport in the experiments. Our nanorod-based technique complements these other nanoscale thermographic

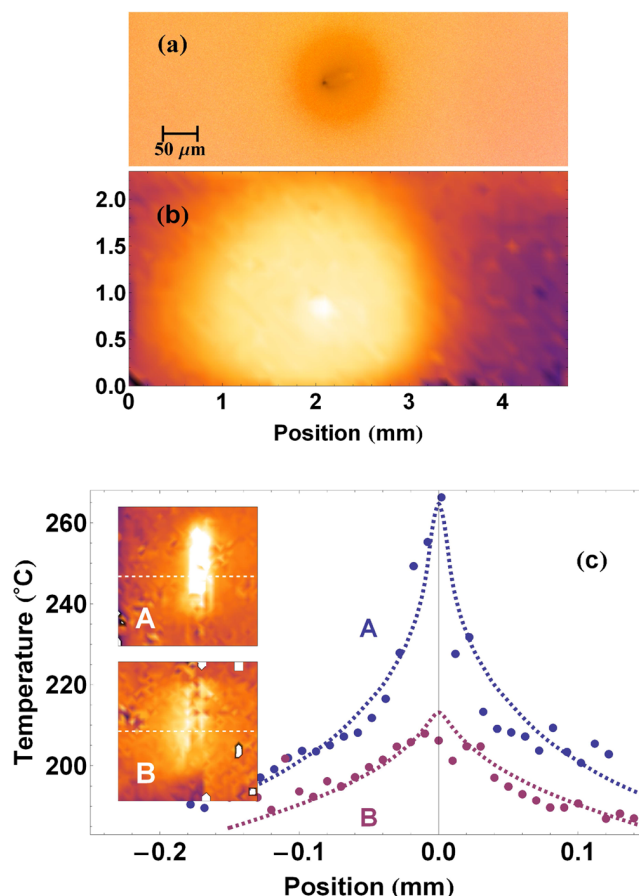


**Figure 5.** SFDB cross-sections. (a) Optical micrograph with exaggerated color saturation. (b) Spectral thermal map at coarse steps. (c) Temperature profile for two different cross-sections. Dashed lines are COMSOL calculations, and points are spectroscopically determined temperatures; insets show the spectral maps for slices A and B in Figure 4a.

methods by combining high spatial resolution, a wide range of continuous temperature response, and the ability to record maximum steady-state temperature for ex situ measurement. It is particularly well-suited to the study of polymer nanocomposites where the AuNRs can be well-dispersed in a transparent matrix and the dynamics of the thermally induced shape change are relatively slow. Thus, it provides an important tool for studies of micro- and nanoscale thermal transport in such materials.

The temperature resolution of the nanosensors depends on a number of factors. The intrinsic heterogeneity of the as-prepared, commercially obtained AuNRs results in broad plasmon peaks due to a distribution of sizes. This limits the precision of the plasmon peak determination and also gives rise to a spread in the temperature response for a given population of nanosensors. This limitation would be minimized by using high purity, uniform size distributions of nanorods. The accurate determination of the SPR energies is vital to the determination of the temperature, and even with monodisperse particles the uncertainty associated with the measurement of the plasmon resonance energies will ultimately limit the precision of the temperature measurement. The physical basis for the observed transformation dynamics remains unknown, and this necessitates a new calibration for each material system in which this technique is used. For example, although all of the



temperature calibration curves are well-fit by a biexponential function, there is a qualitative difference between the dynamics above and below the glass transition temperature of the epoxy (around 140 °C). This seems to indicate that the relevant rates are determined in part by the stiffness or reactivity of the surrounding matrix. The calibration curves may also differ as a function of nanorod encapsulation or growth technique. We expect that the analysis approach reported herein will enable theoretical and computational advances by providing more detailed information about the nanorod transformations in various environments.

## CONCLUSIONS

We have shown that AuNRs may be used as embedded, continuously varying, irreversible temperature sensors over the temperature range of 100–200 °C with an accuracy of at least 6 °C. For steady state thermal profiles of sufficient duration this method enables the ex situ determination of temperature with spatial resolution down to at least 10  $\mu\text{m}$ . These temperatures agree well with surface temperature readings using a commercial infrared camera as well as with the predictions of FEM simulations. In principle, the ultimate spatial resolution is limited only by the density of nanorods, and the nature of the SPR probe. Thus, nanoscale resolution may be achieved with the appropriate confocal or near-field approach.

Because of the dynamic nature of the shape transformation, the accuracy of this technique is subject to the condition that the nanorod aspect ratios have effectively reached steady-state. A more complete understanding of the shape transformation process would enable the use of these nanosensors under nonsteady state conditions. For example, if the rate of shape transformation is limited only by the solubility of the AuNR capping ligands in the host polymer, as suggested by Liu et al., then an analytical expression for the aspect ratio as a function of time may be developed from well-established chemical kinetics. With appropriate physical boundary conditions for surface temperature and/or heating times the full temperature history inside a nanocomposite could be calculated from a series of absorption measurements.

## EXPERIMENTAL SECTION

**Sample Preparation.** AuNRs with average dimensions of 10  $\times$  41 nm were purchased commercially (Nanopartz: Organic Gold Nanorod E12–10–808), dispersed in isopropyl alcohol, and mixed with an epoxy resin (Momentive: EPON 828 + Huntsman: Jeffamine D230) to form a rigid nanocomposite herein referred to as AuNR-Epoxy. The AuNR-Epoxy contains 0.004% gold by volume (0.06% by weight), corresponding to a number density of approximately  $1 \times 10^{13} \text{ mL}^{-3}$ . A survey of TEM images confirms that the AuNRs are well-dispersed in the matrix. In order to avoid prematurely transforming the AuNRs we limited their exposure to elevated temperatures before the experiment. AuNR-Epoxy samples were processed in small batches (<15 mg) to avoid large exotherms and cured at 40 °C for 6 h. The resulting nanocomposite is a structurally rigid material with approximately 60% of the cross-link density of a fully cured system as determined by differential scanning calorimetry (DSC).

For the calibration samples we prepared 2 mm thick samples of AuNR-Epoxy and heated each in a hot stage (Mettler FP82HT) to temperatures between 100° and 200 °C. The target temperature was typically attained within 1 min of heating and was stable to within 1 °C thereafter for the duration of the experiment.

**Absorption Spectroscopy.** Absorption spectra were obtained using a microspectrophotometer (CRAIC MSP 121) in transmission mode. Spatially resolved spectra are obtained using a combination of high magnification and square aperture collection window. AuNR

densities were designed to yield a maximum optical density at the longitudinal plasmon resonance peak between 0.4 and 1.0 over a 2 mm path length. Coarse raster maps were produced with a lateral raster step size of 100  $\mu\text{m}$ , a 15 $\times$  objective, and a camera collection aperture of 40  $\times$  40  $\mu\text{m}$ . Finer resolution maps were produced with a 10  $\mu\text{m}$  step size, a 36 $\times$  objective, and a camera collection aperture of 5  $\times$  5  $\mu\text{m}$ .

**TEM.** Transmission electron micrographs (TEM) were obtained of 100 nm thick microtomed slices of the AuNR-Epoxy after heating using a Phillips CM 200. Aspect ratios were estimated by measuring the longest distances along the length and width of the hemispherically capped cylinders. These values were then averaged over sample populations of 10–20 rods for each temperature, and the errors are estimated as the sample standard deviation.

**SAXS.** Small-angle X-ray scattering (SAXS) measurements were performed at the SAXS/WAXS beamline 7.3.3 of the Advanced Light Source at Lawrence Berkeley National Laboratory both during and after heating. The scattering intensity  $I(Q)$  was fitted with the Irena ? analysis package using standard models for the scattering of rods in dilute systems, where  $Q = (4\pi \sin \theta)/\lambda$  is the magnitude of the scattering vector. The form factor for a rod with log-normal distribution was used to fit the data with the following fit parameters: AuNR volume fraction, breadth of the size distribution ( $\beta \approx 0.15$ ), aspect ratio, and mean radius. Raw intensity versus  $Q$  data was fitted using previously reported methods.<sup>41</sup> The fitted aspect ratio is noisy due to the limited lower  $Q$  range, but  $a$  is calculated from the mean radius by assuming volume conservation of individual nanorods. The uncertainty is estimated from the fitted radius distribution.

**FLIR.** Surface temperature measurements were obtained with a FLIR SC620 using a 40 mm lens. The camera was calibrated by the manufacturer, and an emissivity of 0.88 was assumed for the AuNR-Epoxy surface.

**SFDB.** The single-fiber dogbones (SFDB) used in the internal spatial temperature maps comprise individual carbon fibers (Hexel HexTow IM7) encased in AuNR-Epoxy. These were heated with a Keithley 2100 source-meter via silver paint contacts directly to the fiber at the ends of the SFDB.

## ASSOCIATED CONTENT

### Supporting Information

The Supporting Information is available free of charge on the ACS Publications website at DOI: 10.1021/acsami.5b08188.

Detailed description of the polynomial approximation for light scattering from gold nanorods, including theoretical motivation and coefficient values for the approximate polynomial; study of the asymptotic AuNR aspect ratio after various thermal cycling; and example TEM images (PDF)

## AUTHOR INFORMATION

### Corresponding Author

\*E-mail: jeffery.baur@us.af.mil.

### Author Contributions

The manuscript was written through contributions of all authors. All authors have given approval to the final version of the manuscript.

### Funding

Funding for the project was provided by AFOSR 13RX02COR: Dr. Byung-Lip “Les” Lee, Program Officer.

### Notes

The authors declare no competing financial interest.

## ACKNOWLEDGMENTS

The authors thank Dhriti Nepal, Kyoungweon Park, Rich Vaia, and Vikas Varshney for many helpful discussions. H.K. thanks

Alexander Hexemer and Eric Schaible for assistance with experiments at the SAXS/WAXS beamline 7.3.3 at ALS.

## REFERENCES

- (1) Mohamed, M. B.; Ismail, K. Z.; Link, S.; El-Sayed, M. A. *J. Phys. Chem. B* **1998**, *102*, 9370–9374.
- (2) Link, S.; Burda, C.; Nikoobakht, B.; El-Sayed, M. A. *J. Phys. Chem. B* **2000**, *104*, 6152–6163.
- (3) Al-Sherbini, A.-S. A.-M. *Colloids Surf., A* **2004**, *246*, 61–69.
- (4) Liu, Y.; Mills, E. N.; Compsto, R. J. *J. Mater. Chem.* **2009**, *19*, 2704–2709.
- (5) Ng, K. C.; Cheng, W. *Nanotechnology* **2012**, *23*, 105602.
- (6) Link, S.; El-Sayed, M. A. *Int. Rev. Phys. Chem.* **2000**, *19*, 409–453.
- (7) Petrova, H.; Perez Juste, J.; Pastoriza-Santos, I.; Hartland, G. V.; Liz-Marzán, L. M.; Mulvaney, P. *Phys. Chem. Chem. Phys.* **2006**, *8*, 814–821.
- (8) Taylor, A. B.; Siddiquee, A. M.; Chon, J. W. M. *ACS Nano* **2014**, *8*, 12071–12079.
- (9) Ercolessi, F.; Andreoni, W.; Tosatti, E. *Phys. Rev. Lett.* **1991**, *66*, 911–914.
- (10) Wang, Y.; Teitel, S.; Dellago, C. *Nano Lett.* **2005**, *5*, 2174–2178.
- (11) Wang, Y.; Teitel, S.; Dellago, C. Effect of Surface Structure of Shape Transformations of Gold Nanorods. *J. Comput. Theor. Nanosci.* **2007**, *4*, 282–290.
- (12) Lai, S.; Guo, J.; Petrova, V.; Ramanath, G.; Allen, L. *Phys. Rev. Lett.* **1996**, *77*, 99–102.
- (13) Lai, S. L.; Carlsson, J. R. A.; Allen, L. H. *Appl. Phys. Lett.* **1998**, *72*, 1098–1100.
- (14) Levitas, V. I.; Ren, Z.; Zeng, Y.; Zhang, Z.; Han, G. Crystal-crystal phase transformation via surface-induced virtual premelting. *Phys. Rev. B: Condens. Matter Mater. Phys.* **2012**, *85*, 220104.
- (15) Levitas, V. I.; Samani, K. Melting and solidification of nanoparticles: Scale effects, thermally activated surface nucleation, and bistable states. *Phys. Rev. B: Condens. Matter Mater. Phys.* **2014**, *89*, 075427.
- (16) Carbó-Argibay, E.; Rodríguez-González, B.; Gómez-Graña, S.; Guerrero-Martínez, A.; Pastoriza-Santos, I.; Pérez-Juste, J.; Liz-Marzán, L. M. *Angew. Chem., Int. Ed.* **2010**, *49*, 9397–9400.
- (17) Katz-Boon, H.; Rossouw, C. J.; Weyland, M.; Funston, A. M.; Mulvaney, P.; Etheridge, J. Three-Dimensional Morphology and Crystallography of Gold Nanorods. *Nano Lett.* **2010**, *11*, 273–278.
- (18) Eustis, S.; El-Sayed, M. A. *J. Appl. Phys.* **2006**, *100*, 044324.
- (19) Al-Sherbini, E.-S. A. M. *Mater. Chem. Phys.* **2010**, *121*, 349–353.
- (20) Joy, N. A.; Janiszewski, B. K.; Novak, S.; Johnson, T. W.; Oh, S.-H.; Raghunathan, A.; Hartley, J.; Carpenter, M. A. *J. Phys. Chem. C* **2013**, *117*, 11718–11724.
- (21) Pastoriza-Santos, I.; Pérez-Juste, J.; Liz-Marzán, L. M. *Chem. Mater.* **2006**, *18*, 2465–2467.
- (22) Chen, Y.-S.; Frey, W.; Kim, S.; Homan, K.; Kruizinga, P.; Sokolov, K.; Emelianov, S. *Opt. Express* **2010**, *18*, 8867.
- (23) Nepal, D.; Park, K.; Vaia, R. A. *Small* **2012**, *8*, 1013–1020.
- (24) Ungureanu, C.; Rayavarapu, R. G.; Manohar, S.; van Leeuwen, T. G. Discrete dipole approximation simulations of gold nanorod optical properties: Choice of input parameters and comparison with experiment. *J. Appl. Phys.* **2009**, *105*, 102032.
- (25) Bohren, C. F.; Huffman, D. R. *Absorption and Scattering of Light by Small Particles*; Wiley: New York, 2013.
- (26) Pelton, M.; Bryant, G. *Introduction to Metal-Nanoparticle Plasmonics*; John Wiley: Hoboken, NJ, 2013.
- (27) Link, S.; Mohamed, M. B.; El-Sayed, M. A. *J. Phys. Chem. B* **1999**, *103*, 3073–3077.
- (28) Chailleux, E.; Salvia, M.; Jaffrezic-Renault, N.; Matejec, V.; Kasik, I. *Smart Mater. Struct.* **2001**, *10*, 194.
- (29) Johnson, P. B.; Christy, R. W. *Phys. Rev. B* **1972**, *6*, 4370–4379.
- (30) Combe, N.; Jensen, P.; Pimpinelli, A. *Phys. Rev. Lett.* **2000**, *85*, 110–113.
- (31) Fish, G.; Bouevitch, O.; Kokotov, S.; Lieberman, K.; Palanker, D.; Turovets, I.; Lewis, A. *Rev. Sci. Instrum.* **1995**, *66*, 3300–3306.
- (32) Shrestha, R.; Lee, K. M.; Chang, W. S.; Kim, D. S.; Rhee, G. H.; Choi, T. Y. *Rev. Sci. Instrum.* **2013**, *84*, 034901.
- (33) Breitenstein, O.; Warta, W.; Langenkamp, M. *Lock-in Thermography Basics and Use for Evaluating Electronic Devices and Materials*; Springer-Verlag: Berlin, 2010.
- (34) Lo, H.; Ram, R. J. *J. Electron. Mater.* **2012**, *41*, 1332–1336.
- (35) Zhu, J.; Tang, D.; Wang, W.; Liu, J.; Holub, K. W.; Yang, R. J. *Appl. Phys.* **2010**, *108*, 094315.
- (36) Feser, J. P.; Cahill, D. G. *Rev. Sci. Instrum.* **2012**, *83*, 104901.
- (37) Koh, Y. K.; Singer, S. L.; Kim, W.; Zide, J. M. O.; Lu, H.; Cahill, D. G.; Majumdar, A.; Gossard, A. C. *J. Appl. Phys.* **2009**, *105*, 054303.
- (38) Wang, H.; Sen, M. *Int. J. Heat Mass Transfer* **2009**, *52*, 2102–2109.
- (39) Gong, F.; Bui, K.; Papavassiliou, D. V.; Duong, H. M. *Carbon* **2014**, *78*, 305–316.
- (40) Mecklenburg, M.; Hubbard, W. A.; White, E. R.; Dhall, R.; Cronin, S. B.; Aloni, S.; Regan, B. C. *Science* **2015**, *347*, 629–632.
- (41) Koerner, H.; MacCuspie, R. I.; Park, K.; Vaia, R. A. *Chem. Mater.* **2012**, *24*, 981–995.

## Supporting Information

# High Resolution Mapping of Thermal History in Polymer Nanocomposites: Gold Nanorods as Microscale Temperature Sensors

W. Joshua Kennedy,<sup>†,‡</sup> Keith A. Slinker,<sup>†,‡</sup> Brent L. Volk,<sup>‡</sup> Hilmar Koerner,<sup>‡</sup>

Trenton J. Godar,<sup>¶,‡</sup> Gregory J. Ehlert,<sup>‡</sup> and Jeffery W. Baur<sup>\*,‡</sup>

<sup>†</sup>*UTC, Materials and Manufacturing, 1270 North Fairfield Road, Dayton, OH 45433*

<sup>‡</sup>*Air Force Research Laboratory, Materials and Manufacturing Directorate (AFRL/RXCC),  
Wright-Patterson Air Force Base, OH 45429*

<sup>¶</sup>*UDRI, 300 College Park, Dayton, OH 45469*

E-mail: jeffery.baur@us.af.mil

Several of the works cited in the main text have investigated the degree to which expressions such as Equation 1 correlate with observed absorption spectra for various values of  $a$  and  $\epsilon_m$ , as well as for subtle differences in  $\epsilon_1$  and  $\epsilon_2$ . We make no specific claims about the accuracy of this expression other than to highlight the agreement of our calculated aspect ratios with independently measured values from TEM and SAXS. However, our general approach to the temperature calibration is motivated by the fact that changes in  $a$  and  $\epsilon_m$  affect the predicted resonance energies in qualitatively different ways. Figure S-1 illustrates this principle by showing predicted extinction coefficients for various values of these two parameters.



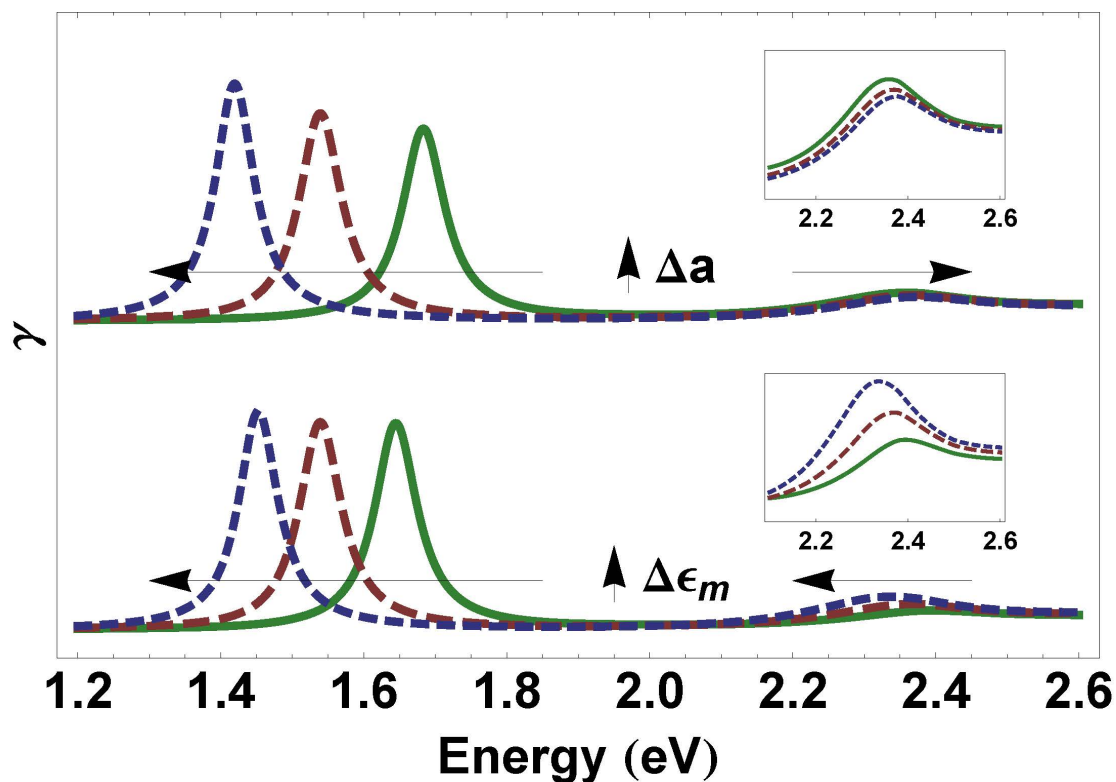


Figure S-1: Theoretical dependence of the scattering spectrum for AuNRs on aspect ratio  $a$  and local dielectric  $m$ . The upper plots show the extinction for aspect ratios of 2.5 (solid green), 3.0 (dashed red), and 3.5 (dotted blue) while the local dielectric is fixed at 3.0. In the lower plots the dielectric takes the same sequence of values (2.5, 3.0, 3.5) while the aspect ratio is fixed at 3.0. The ET resonances for each plot are magnified in the insets. Arrows indicate the direction that the peak shifts as the parameters increase.

The choice of a separated-variable, 4th order polynomial as the numerically solvable approximation for the two  $E_i(a, \epsilon_m)$  (Equation 2 in the text) is arbitrary but justifiable. Table S-1 shows the coefficients  $c_{jk}$  that minimize  $R^2$  between the invertible polynomial function and Equation 1, which is non-invertible due to the empirical values for  $\epsilon_1$  and  $\epsilon_2$ . While the zero and first order terms obviously dominate, the higher order terms are not negligible. Only by including up to 4th order terms is the RMS variance between the polynomial function and the full expression reduced to less than one percent over the sampled domain ( $a \in [1, 5]; \epsilon_m \in [1, 10]$ ).

Table S-1: Coefficients for the polynomial approximation of  $E(a, \epsilon_m)$  in Equation 4. Index  $j$  is the row and index  $k$  is the column.

j\k	$\frac{E_L}{\epsilon_m}$				
	0	1	2	3	4
0	1.37017	1.13551	-0.31381	0.03685	-0.00161
1	2.02695	-1.82677	0.45046	-0.05196	0.00225
2	-1.03890	0.79840	-0.20623	0.02459	-0.00108
3	0.21013	-0.15923	0.04281	-0.00519	0.00023
4	-0.01558	0.01192	-0.00328	0.00040	-0.00002

j\k	$\frac{E_T}{\epsilon_m}$				
	0	1	2	3	4
0	2.61635	-0.25875	0.03873	-0.00447	0.00020
1	-0.26946	0.36822	-0.09556	0.01129	-0.00048
2	0.11918	-0.15128	0.04150	-0.00499	0.00021
3	-0.01997	0.02520	-0.00709	0.00086	-0.00004
4	0.00121	-0.00154	0.00044	-0.00005	0.000002

We also tried an alternate approach by employing both polynomial fits and numeric interpolation functions for  $\epsilon_m$ , but the subsequent inversion procedure was not robust over the set of experimental data in the temperature calibration procedure (ie, numerically solving Equation 2 proved unstable).

In order to test the uniqueness of the final shape at a particular temperature we subjected several samples to various thermal histories. Figure S-2 shows the time evolution of the calculated aspect ratio for three of these measurements, each of which was initially heated to 120° C for one hour and then allowed to cool to room temperature. Each sample was

then reheated to a steady state ( $\sim 3$  hours) temperature of (a)  $100^\circ\text{C}$ , (b)  $120^\circ\text{C}$ , and (c)  $160^\circ\text{C}$ . The final aspect ratio in each of these cases is uniquely determined by the maximum steady state temperature experienced regardless of the order of heating. For example, sample (a) does not change substantially during the second heating cycle because it has already experienced a higher temperature. Sample (b) continues the same biexponential evolution as if it had not been interrupted. The evolution of sample (c) changes character completely during the second cycle and asymptotically approaches the same value as the calibration sample held at  $160^\circ\text{C}$ . We repeated these experiments for several temperature profiles and in different resin systems and found similar behavior. Note that the plots shown in Figure S-2 pertain to a different batch of AuNRs than those of Figure 2 in the text; therefore the specific asymptotic values are different.

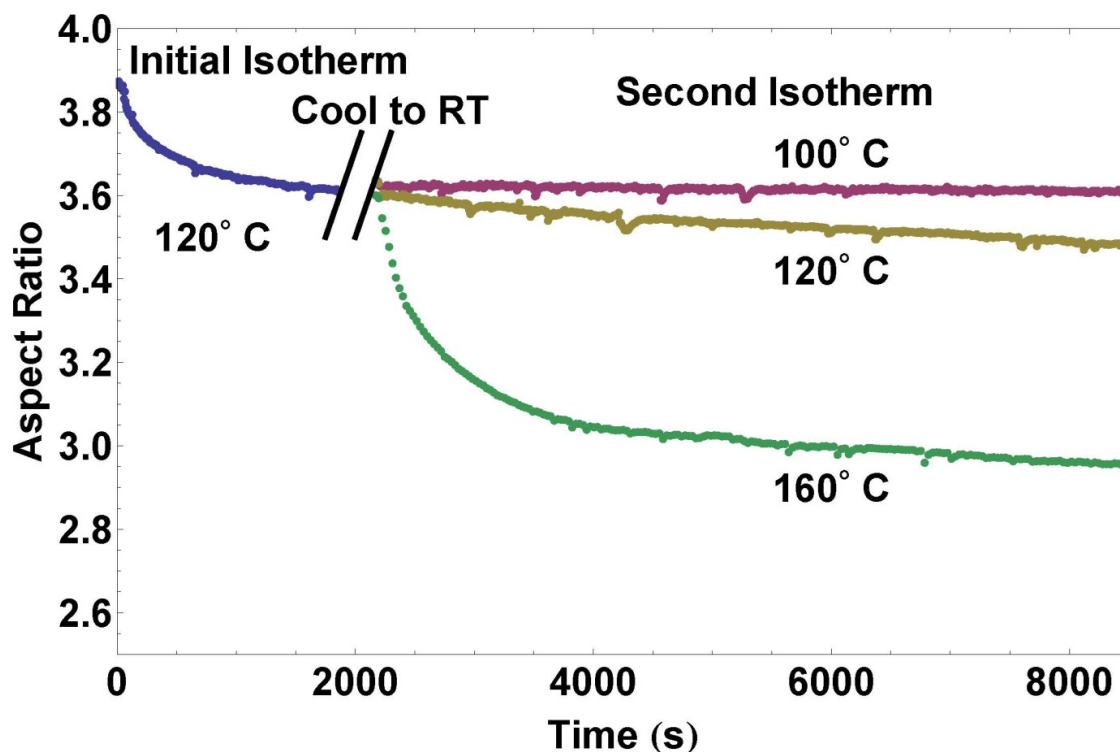


Figure S-2: Aspect ratio evolution for three different samples initially heated and held at  $120^\circ\text{C}$  for 30 min and subsequently heated to  $100^\circ$ ,  $120^\circ$ , and  $160^\circ\text{C}$  respectively. In each case the final asymptotic aspect ratio is limited by the maximum temperature experienced over the course of the thermal history, irrespective of the time between heating cycles.

Figure S-3 shows a few representative TEM micrographs of AuNRs after heating. The

AuNRs are dilutely dispersed in the matrix, and so only one rod at a time is visible at high magnification. We measured approximately 100 individual nanorods in this manner and report the measured aspect ratios for the data in Figure 2 using the variance in our measurements for a particular temperature as the uncertainty. However, it is difficult to know, without time-consuming tilting measurements, whether or not the nanorod axes are perpendicular to the field of view. This is especially true because of the intrinsic inhomogeneity in the sample population. The as-received nanorods already had a noticeable variation in radius, so that direct comparison of micrographs between temperatures is ambiguous. Therefore, we kept only the aspect ratios in the top 25% of all measurements at a particular temperature, potentially biasing the results.

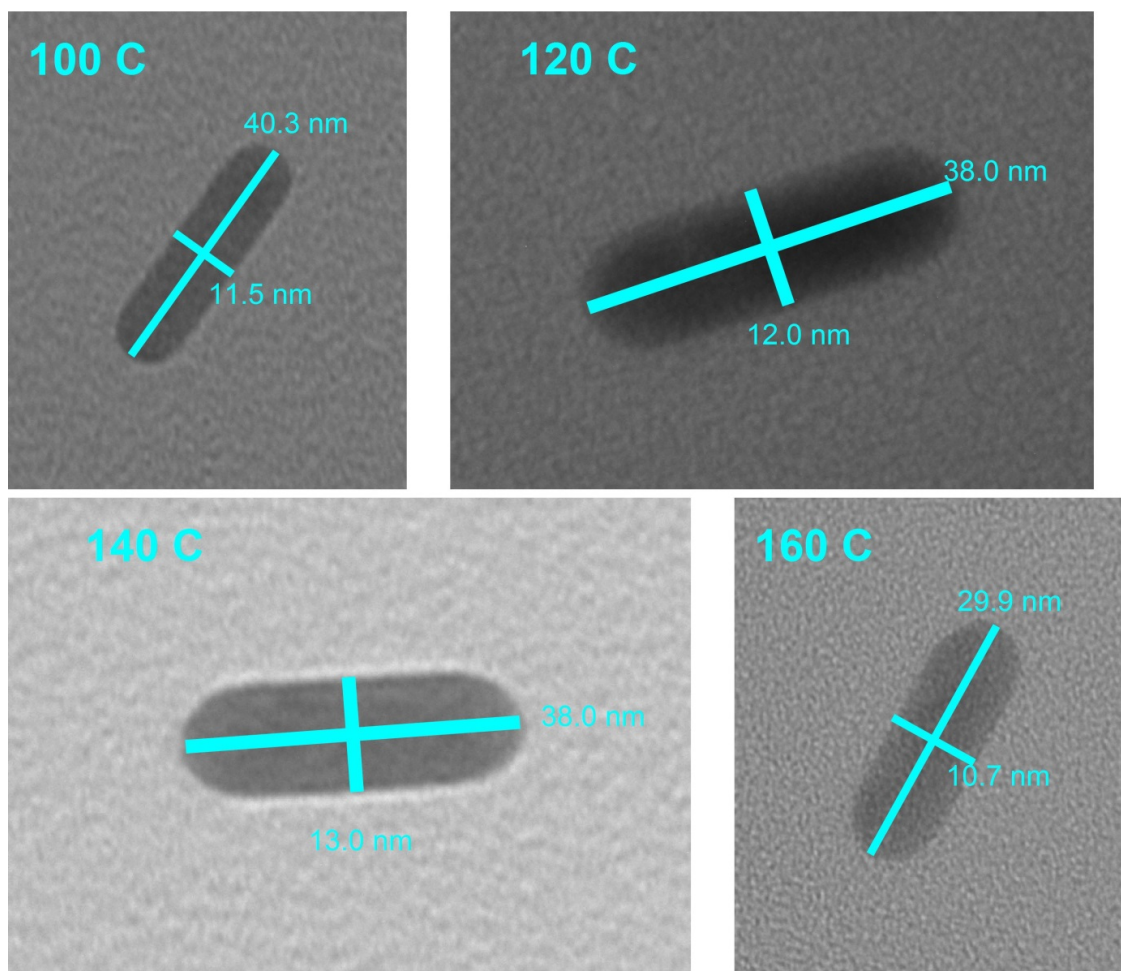


Figure S-3: Sample TEM images of AuNRs in Epoxy matrix after heating for several hours at the temperatures shown.

## Appendix C. COMSOL® Multiphysics

# Predicting the Combined Optical and Thermal Response of Polymer Matrix Composites with Varying Composite Properties

Trenton J. Godar\*

*University of Dayton Research Institute, Dayton, Ohio, 45469, USA*

Brent L. Volk <sup>†</sup>

*Air Force Research Laboratory, Dayton, Ohio, 45433, USA*

W. Joshua Kennedy<sup>‡</sup>

*Universal Technology Corporation, Dayton, OH 45432, USA*

Geoffrey J. Frank<sup>§</sup>

*University of Dayton Research Institute, Dayton, OH 45469, USA*

Gregory J. Ehlert<sup>†</sup>

*Air Force Research Laboratory, Dayton, OH 45433, USA*

The effective optical and thermal properties as well as the opto-thermal response of composite materials are investigated. A stochastic method is developed which implements a random microstructure generation (RMG) algorithm to produce a synthetic microstructure representing the geometry of unidirectional continuous fiber reinforced polymer matrix composites (PMCs). Simulation of the synthetic microstructure determines effective thermal properties, effective optical properties, and the thermal response to optical energy. The micromechanics framework developed herein is also applied to unit cell analysis and compared with analytical solutions. The metrics of effective transverse thermal conductivity, effective attenuation coefficient, and temperature response are studied as a function of fiber volume fraction. We show that some composites' effective thermal properties can be adequately predicted using unit cell analysis or analytic techniques; however, effective optical properties and thermal response to optical input depend strongly the specific random arrangement of the fibers.

## Nomenclature

$\alpha$	Attenuation coefficient, $1/m$
$\epsilon$	Surface emissivity
$\rho$	Density, $kg/m^3$
$A$	Power absorption coefficient
$C_p$	Specific heat capacity, $J/(kg * K)$
$H$	RVE Height, $m$
$I$	Intensity, $W/m^2$
$I_0$	Incident intensity, $W/m^2$
$L$	RVE Length, $m$

---

\*Associate Research Engineer, Multiscale Composites and Polymers, Dayton, OH, Member

<sup>†</sup>Research Materials Engineer, Materials and Manufacturing Directorate, Dayton, OH, non-Member

<sup>‡</sup>Research Scientist, Materials and Manufacturing, Dayton, Ohio, non-member

<sup>§</sup>Senior Research Engineer, Aerospace Mechanics, Dayton, Ohio, Member



$Q_{src}$	Heat Source, $W/m^3$
$R$	Power reflection coefficient
$T$	Temperature, $K$ or $^{\circ}C$
$T_r$	Power transmission Coefficient
$h$	Heat transfer coefficient, $W/(K * m^2)$
$k$	Thermal conductivity, $W/(K * m)$
$\dot{q}$	Heat Flux, $W/m^2$
$r_f$	Fiber Radius, $m$
$t$	Time, $s$
$v_f$	Fiber volume fraction
<i>Subscripts</i>	
$eff$	Effective property
$f$	Fiber
$m$	Matrix
$normal$	Direction normal to the surface
$x, y, z$	x-component, y-component, z-component

## I. Introduction

Polymer matrix composites (PMCs) continue to increase as the material of choice in modern aerospace systems on account of the high specific stiffness, high specific strength, enhanced environmental stability, and the ability to tailor anisotropic properties. The methods and processes to implement PMCs in aerospace systems are fairly well established; however there remains ongoing development in the methods to manufacture and finish PMCs. High power lasers in particular have been utilized to great effect in various composite processing and evaluation applications, including trim operations, paint removal, thermoplastic consolidation, laser machining, curing, medical/dental applications, and non-destructive evaluation (NDE).<sup>1-7</sup> The laser is utilized as a focused, variable intensity heat source in each of these applications, which requires an understanding of how optical energy is transduced into heat and how the heat is subsequently transferred.

Transducing optical energy to thermal energy *within* composites must be well understood in order to optimize materials and processes associated with these applications; thus, we study the interaction between incident optical energy and thermal transport in the microstructure of PMCs. Several analytic models can predict the effective properties of composites but they are not valid or well developed for all composite systems across all types of energy input mechanisms, especially those with high fiber volume fractions, fiber coatings, finite thermal resistances, and for optical properties.

Traditional composite mechanics generally utilize representative volume elements with patterned packing or unit cells to homogenize the microstructure into an effective composite material and then apply laminated plate or similar theories to understand a structure. Stress analysis utilizing the homogenized microstructure is highly accurate; however the predictions are not nearly as accurate for estimating other effective properties such as thermal conductivity, electrostatic coefficients, or piezoelectric coefficients. The micromechanics community has adapted multi-inclusion models to account for discrepancies when modeling multiphase composites. Thus far multi-inclusion models have been applied to mechanical, piezoelectric, and thermal problems but not optical to thermal transduction.

Analytic models are able to predict the effective thermal conductivity of composite materials, including those with interface resistance and fiber coatings, but are subject to certain restrictions.<sup>8-12</sup> Many analytic models rely on the simple rule of mixtures (SRM), enhanced rule of mixtures (EROM), or the equivalent inclusion method (EIM) to predict effective properties. Analytic models predicting thermal conductivity have shortcomings which can be overcome using microscale finite element analysis (FEA), such as inaccurate conductivity prediction at high volume fraction due to neglecting conductive paths.<sup>13,14</sup>

Sihn and Roy<sup>12</sup> have explored the applicability of the EROM and EIM to finding the transverse thermal conductivity of continuous fiber composites; however, the EROM does not include the effects of coatings or interface thermal resistance. Hasselman and Johnson<sup>9</sup> have also developed a closed form analytic solution based on the equivalent inclusion method (EIM). Unit cell FEA can typically account for high fiber volume fraction, fiber coatings, and interface resistance, but still neglects conductive paths that may develop in a real microstructure. Because of the limitations of analytic thermal models and unit cell methods to account for

these situations and the lack of optical models developed for fiber reinforced composites, a micromechanical approach with RMG is implemented. Though the micromechanics approach is capable of including fiber coatings and interface resistance, these effects are not considered in this work.

Due to the complex scattering, absorption, and reflection occurring via inclusion interaction, unit cell analysis and various rule of mixtures methods will not be sufficient to determine effective optical properties. Analytic prediction methods for effective optical properties of continuous fiber reinforced composites are considerably less developed than the thermal conductivity models, likely due to their lack of application as optical components. Some simplified models can be used to predict PMC optical behavior such as the Kubelka-Munk two flux and four flux models, but these require experimental evaluation to find fit parameters.<sup>15</sup> Geometric optics or ray tracing has also been used successfully to study the optical properties of unidirectional composite systems where the relative length scales and wavelengths fall within appropriate margins.<sup>16</sup> In this work, we demonstrate the implementation of a random microstructure generation (RMG) algorithm and link optical interaction to thermal effects to enable the accurate prediction of effective optical and thermal properties, as well as the thermal response to optical energy, in a stochastic manner. The approach is verified, through comparison to existing analytical models and literature values, for predicting the effective thermal conductivity of composites. The full wave solution of Maxwell's equations is employed to account for diffraction and interference effects that become significant when the wavelength of the incident radiation is similar in size or larger than the inclusions and other geometric scattering features.

## II. Method

### A. Synthetic Microstructure Generation

The challenges of high volume fraction, conductive paths, and unit cells are addressed through the use of an RMG algorithm developed by Melro et al.<sup>17</sup> This RMG algorithm is further modified by Romanov et al.<sup>18</sup> to include a random minimum fiber spacing to prevent an unnaturally large amount of touching fibers and verified this modification through image analysis and micromechanics simulations; thus, the RMG algorithm with Romanov's modification is implemented in Matlab and used in this work. The RMG code uses a random, hard-core packing algorithm to place circular fibers in a rectangular matrix until either the desired fiber volume fraction ( $v_f$ ) or the jamming limit ( $\approx 50\%$ ) is reached. If this limit is reached, a series of heuristic re-ordering steps moves the existing fibers closer together which allows new fibers to be inserted in the matrix rich regions. An example of a microstructure subject to the jamming limit and one that overcomes this limit is shown in Figure 1.

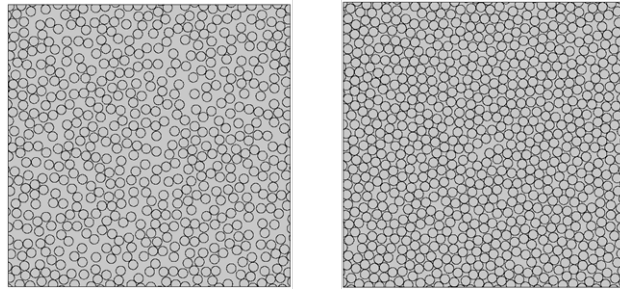


**Figure 1.** The microstructure on the left is subject to the jamming limit of approximately 50% while the microstructure on the right has achieved a volume fraction of 65% through heuristic reordering

The theoretical maximum volume fraction ( $\frac{\pi}{2\sqrt{3}} \approx 90.69\%$ ) is achieved with perfect hexagonal packing. Theoretically, the heuristic reordering algorithm will eventually achieve this volume fraction if the minimum fiber spacing condition is set to zero and the algorithm is allowed to execute without iteration limits. However, the practical upper limit on volume fraction is about 70% for both the RMG algorithm and actual composites.

### B. Thermal Conductivity

Effective thermal conductivity of continuous fiber reinforced PMCs can be found in a number of ways. Using the simple rule of mixtures (SRM) as a parallel resistive network calculates the lower limit to transverse thermal conductivity (assuming perfect interfaces) and provides a good approximation of the longitudinal

thermal conductivity.<sup>13</sup> The longitudinal conductivity approximation by the SROM assumes the fibers are perfectly aligned and that fiber waviness does not significantly affect the effective thermal conductivity. Other analytic methods have been used to determine the effective thermal conductivity, but only the EIM and SROM are included in this work because others have successfully used the EIM whereas SROM is the simplest model available.<sup>9,12</sup> The boundary conditions used for predicting the effective thermal conductivity via FEA are shown in Figure 2.

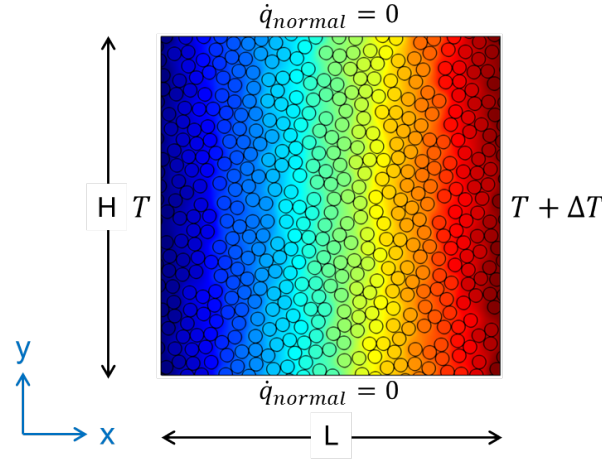


**Figure 2. Boundary conditions for predicting transverse thermal conductivity in a continuous fiber reinforced composite**

The boundary conditions in Figure 2 are chosen based on the work of Pramla et al.<sup>19</sup> which explores and evaluates several methods of applying boundary conditions to an RVE to approximate the thermal conductivity of composites. Their work identified the boundary conditions shown in Figure 2 as the most accurate method of predicting effective thermal conductivity. Once the steady state temperature field is solved for a given microstructure, the effective transverse thermal conductivity is calculated using Equation 1.

$$K_{eff} = \frac{L \int_0^H h_x(y) dy}{H \Delta T} \quad (1)$$

Where  $K_{eff}$  is the effective thermal conductivity,  $L$  is the length of the RVE,  $H$  is the height of the RVE,  $\Delta T$  is the temperature difference, and  $h_x$  is the heat flux in the x direction. Unlike analytic solutions, very few composite property restrictions, such as high thermal conductivity mismatch ratio, exist in the FE solution. Unfortunately, the size of the RVE must be at least approximately 50x the average fiber radius ( $r_f$ ) in any direction so as to avoid boundary effects and find a good approximation for the average heat flux.<sup>19</sup> The FE simulation allows us to assess the variability due to the stochastic nature of the microstructure because each synthetic generation has a unique geometry. Stochastic variation is generally small with respect to effective thermal conductivity when perfect interfaces are assumed (no coatings or thermal interface resistance).

### C. Optical Properties

Effective optical properties of random microstructure composites depend strongly on the arrangement of fibers due to diffraction and interference effects that occur at fiber edges and between fibers. The fiber size relative to the wavelength and the inter-fiber spacing perpendicular to wave propagation has a significant impact on how energy moves through the composite due to absorption, slit diffraction between fibers, and edge diffraction occurring at every fiber subject to irradiation. Epoxies and other polymers used as matrix material for PMCs are generally transparent in the near infrared spectrum (700 nm to 2500 nm) while the inclusions (fibers) may have a wide range of properties in this spectrum. Carbon fibers are typically highly absorbing in the near IR spectrum while glass fibers are mostly transparent and other fibers such as aramids may have optical properties somewhere in between. Due to the complexity of arrangements and size of the fibers and fiber spacing relative to the wavelength, the full wave solution is solved to account for all the contributing effects. In cases where the wavelength is much smaller than the smallest feature size, the

geometric optics approximation known as ray tracing may be used. The geometric optics (i. e. ray tracing) approximation may be appropriate when the fibers are highly absorbing and densely packed enough such that diffraction effects are negligible. For lower volume fractions, diffraction effects become more significant due to the prevalence of fiber edges and gaps which further motivates the full wave solution compared to the geometric optics approach which neglects the enhanced absorption and scattering caused by diffraction.

The effective optical properties of the composite are quantified through a method similar to the effective thermal properties: FE simulation of an RVE. Finding the effective optical properties of a composite first uses the RMG algorithm to generate a random microstructure. A periodic port produces a plane wave which propagates toward the synthetic microstructure. The plane wave can be either “s” or “p” polarized with respect to the fiber surface, but in this work the EM waves are always “p” polarized so that the initial electric field is perpendicular to the fiber axis. To capture and remove any portion of the incident energy that is reflected or transmitted, perfectly matched layers (PMLs) surround the microstructure and the port at the right and left boundaries as shown in Figure 3. The PML boundaries quickly attenuate any incident wave and prevent reflection of waves in nearly any orientation without needing to have prior knowledge of the polarization or propagation constant. The top and bottom boundaries in Figure 3 are perfect electric conductors (PEC) which causes perfect reflection and simulates a semi-infinite condition. A summary of these boundary conditions is shown in Figure 3.

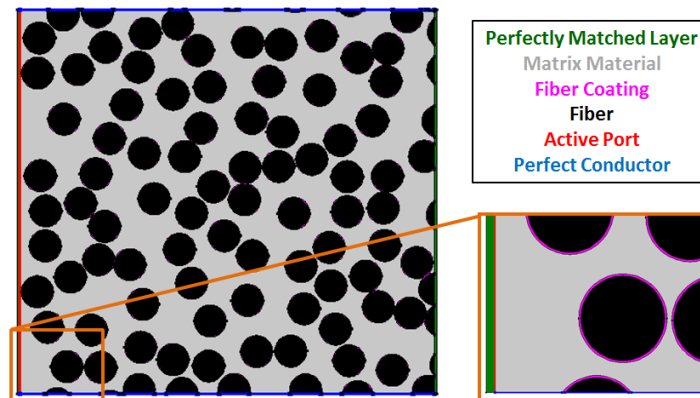


**Figure 3. Boundary conditions and model configuration for random fiber optical simulation.**

From the optical simulation shown in Figure 3, the effective values for power absorption ( $A$ ), power transmission ( $T_r$ ), power reflection ( $R$ ), and attenuation coefficient ( $\alpha_{eff}$ ) can be found.  $T_r$  is found by integrating the time averaged power density on the right side of the RVE whereas  $A$  is calculated by integrating the power dissipation density within the RVE, or just within the fibers if the matrix is considered transparent. According to conservation of energy, all of the incident optical energy must either be transmitted, reflected, or absorbed. Thus,  $R$  is calculated by subtracting  $A$  and  $T_r$  from unity.

Due to the finite, random nature of the RVE, the transmission may be non-zero. This is especially true for low volume fractions of highly absorbing fibers any volume fraction of transparent or weakly absorbing fibers. In order to accurately predict effective optical properties for a given microstructure, the transmission term in the RVE should be as close to zero as possible in order to be considered optically thick. Achieving an optically thick RVE with unit cells is difficult at low volume fractions, thus the unit cells are repeated along the wave propagation direction to address this issue. For highly absorbing fibers at high fiber volume fractions, the depth at which the transmission term approaches zero may be within a few fiber diameters. However if the fibers are transparent, weakly absorbing, reflective, or the volume fraction is low, the composite could conceivably have a non-zero transmission term depending on the total thickness. Thus, the actual thickness of the part must be considered when finding the effective optical properties of thin materials or transparent or translucent materials. Figure 4 shows the various types of unit cell configurations and an example of the random microstructure applied to the optical simulation. Figure 5 highlights the difficulty of producing an optically thick RVE via the unit cell methods shown in Figure 4 by plotting the required depth to be considered optically thick as a function of fiber volume fraction.

The value for  $\alpha_{eff}$  is found by first reducing the two dimensional power density (i.e. intensity) to a one

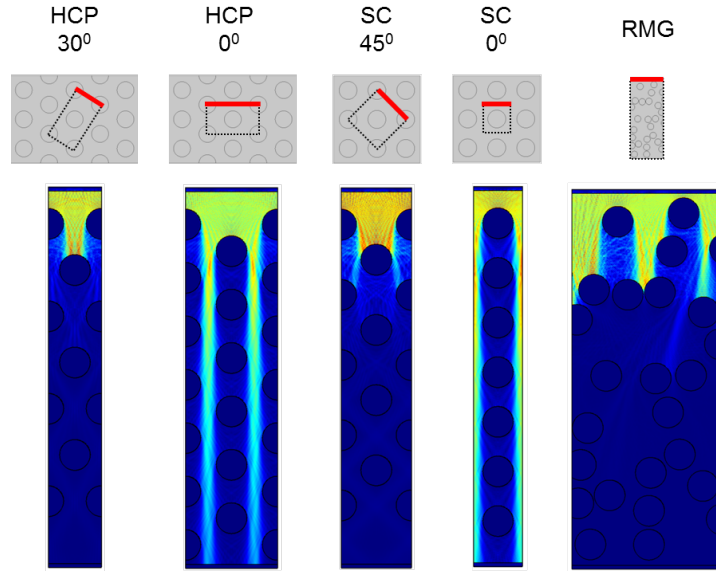


Figure 4. Different types of RVEs showing electric field propagation and location of the input port (red line) with the wave always initially propagating normal to the port. All RVEs shown here are at 30% fiber volume fraction and  $100\text{ }\mu\text{m}$  ( $20\text{ fiber radii}$ ,  $20r_f$ ) deep.

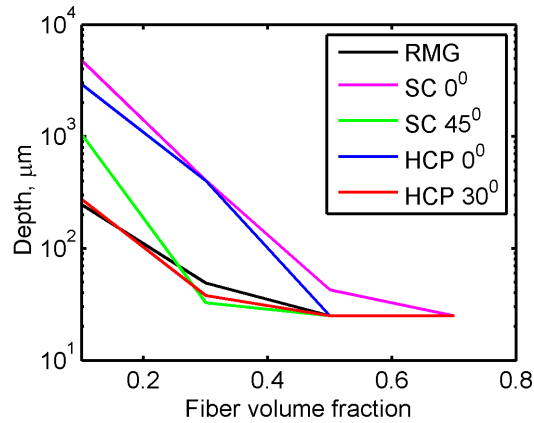


Figure 5. Optical simulation depth required to be considered optically thick for various microstructure generation types. Values larger than the part thickness are estimated based on effective attenuation coefficient.

dimensional spatial average so that power is represented as a function of depth. The attenuation coefficient ( $\alpha_{eff}$ ) is then found by fitting the intensity as a function of depth to the Beer-Lambert law (Equation 2) and extracting the exponential coefficient.<sup>15</sup> As shown in Figure 6, the Beer-Lambert law describes the power attenuation well in the RMG microstructure which allows  $\alpha_{eff}$  to be found using a least squares fit. Analytically, the negative derivative of the Beer-Lambert law can be used to find the heat source as a function of depth ( $Q_{src}$ ) as shown in Equation 3.

$$I(x) = I_0 e^{-\alpha_{eff} * x} \quad (2)$$

$$Q_{src}(x) = -\frac{dI(x)}{dx} = \alpha_{eff} I_0 e^{-\alpha_{eff} * x} \quad (3)$$

The left plot in Figure 6 shows the FEA results for the electric field propagation through a 30% volume fraction composite microstructure generated using the RMG method. The middle plot in Figure 6 shows Equation 2 fit to the intensity as a function of depth. Of the two fit parameters  $\alpha_{eff}$  and  $I_0$ ,  $\alpha_{eff}$  is the

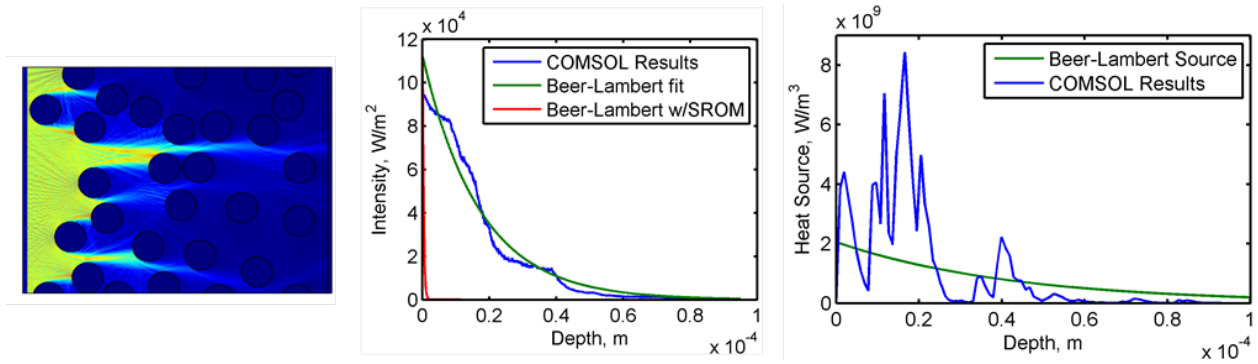


**Figure 6. Left: Electric field propagation, Middle: Beer-Lambert law fit to power density and SROM results, Right: Distributed heat source. All images are from the same 30% volume fraction composite.**

most important because it describes the effective wave propagation and attenuation through the depth of the composite whereas  $I_0$  is simply an input to the model. The SROM curve in the middle plot of Figure 6 shows power distribution if SROM were used to calculate  $\alpha_{eff}$ . Clearly, the SROM over-predicts  $\alpha_{eff}$  and causes the heat source to essentially be a surface heat source. The right plot in Figure 6 shows the heat source as a function of depth for the FEA simulation and assuming Beer-Lambert law absorption. Although Equation 2 fits the intensity distribution well, using the extracted  $\alpha_{eff}$  to define the heat source as a function of depth (Equation 3) does not agree very well with the FEA results. This is because the intensity distribution from the FEA accounts for absorption, reflection, multiple reflections, and scattering whereas Equation 3 assumes the reduction in intensity is only due to absorption.

#### D. Thermal Response to Optical Energy

Typically the thermal response to optical input for a material system is simulated by either a one dimensional surface flux approximation (1D SFA) or a logarithmic heat source.<sup>20,21</sup> The simulation is then treated as a thermal transport problem with no feedback to the optical solution except in the form of element removal or "element death" in some FE simulations where ablation thresholds are reached.<sup>4</sup> While this approach may be applicable to homogeneous materials or heterogeneous materials with pulsed lasers, it is not necessarily valid for continuous wave (CW) laser interaction with composite materials having constituents with varying optical properties that lead to non-uniform absorption and reflections. These varying properties and non-dilute loading conditions of inclusions on the order of the wavelength also make it difficult to analytically predict the intensity distribution due to scattering and absorption.

In this work, determining the thermal response to optical input within a composite is accomplished using a multi-fidelity approach within a single simulation. Two zones of differing fidelity are created to simulate the optical energy absorption and the thermal response. The high fidelity zone is used to solve for the wave propagation and absorption, which in turn becomes the heat source input for the thermal simulation. The size of this zone will depend on the depth required to be considered optically thick, the overall part thickness, the wavelength of interest, and computational resource constraints. The lower fidelity zones ("Mesh Transition Zone" and "Bulk Material Zone" in Figure 7) are present to include the influence of convection and radiation at the non-irradiated (back surface) of the part while taking into account the actual part thickness and different external thermal conditions on the irradiated surface (front surface) and the back surface. The geometry created to encompass both fidelity zones and the simulation steps corresponding to each zone are shown in Figure 7.

In Figure 7, the spatial heat source ( $Q_{src}$ ) is determined by the optical simulation whereas the effective specific heat capacity ( $C_{p,eff}$ ) and effective density ( $\rho_{eff}$ ) are determined using SROM. The decision step condition of  $T_r \leq 0.5\%$  was determined via numerical convergence on  $R$ ,  $T_r$ ,  $A$ , and  $\alpha_{eff}$ . Once the boundary conditions are set,  $Q_{src}$  has been determined, and the effective thermal properties have been determined, a transient heat transfer simulation is performed to determine the temperature field. All of the simulation steps in this work are completed using COMSOL. It should be noted that the geometry in Figure 7 makes the inherent assumption that the incident optical beam width is larger than the thickness of the composite. It should also be noted that the solution most closely resembles what is happening directly under



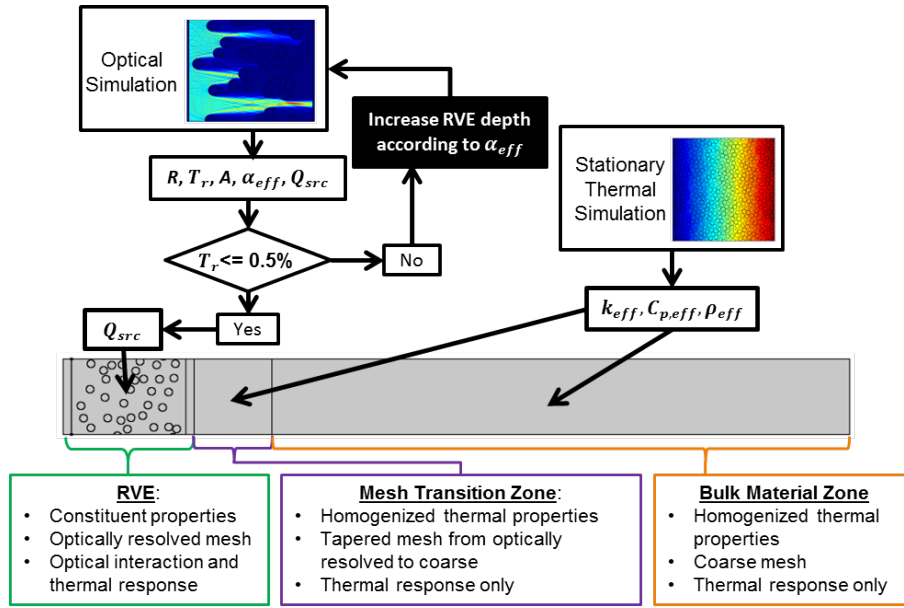


Figure 7. Optical to thermal algorithm and corresponding geometric configuration

the center of the beam and will not be as accurate near the beam edge due to the semi-infinite assumptions made by this model. In the areas labeled “Bulk Material Zone” and “Mesh Transition Zone”, the effective thermal properties are assumed to be quasi-isotropic such that the conductivity is isotropic within the plane being simulated. For the purposes of comparing this multi-fidelity approach, a simple one dimensional heat transfer model is constructed which uses the same thermal boundary conditions as the model in Figure 7, but assumes the heat source either comes from a point flux at the surface (1D SFA), or as a distributed heat source as defined by the attenuation coefficient and Equation 3 (1D RMG Input). The 1D RMG Input model is a low fidelity thermal model which uses the effective thermal properties and effective optical properties as determined by the higher fidelity RMG model. The effective thermal properties for the 1D SFA model are found using the EIM whereas the effective optical properties assume all the incident energy is absorbed at the surface.

The thermal boundary conditions used to determine the temperature field of the opto-thermal response will greatly impact the temperature solution inside the material. In this work, the top and bottom boundaries in Figure 7 are perfectly insulated, which assumes semi-infinite conditions. The convection conditions are assumed to be asymmetric with heat transfer coefficients of  $50 \frac{W}{m^2 K}$  on the front surface (left surface in Figure 7), and  $10 \frac{W}{m^2 K}$  on the back surface (right surface in Figure 7). Surface to ambient radiation is also considered on the front and back surfaces because of the relatively high (0.88) surface emissivity ( $\epsilon$ ) of the epoxy. The total composite thickness used in this work is 1 mm and all initial temperatures and surrounding temperatures are assumed to be 20 °C.

### III. Results and Discussion

#### A. Thermal Conductivity

The ultimate goal of this work is to determine the temperature field of PMCs after optical energy absorption; thus accurately predicting the effective through thickness thermal conductivity is essential. Although the transverse conductivity can be found in a number of ways, the FE method with RMG is used due to its versatility, stochastic capability, and lack of restrictions regarding constituent and interface properties. Effective thermal conductivity predictions are compared to experimental results<sup>22</sup> in Figure 8 using the following methods: RMG FE, EIM, SROM, HCP unit cell, and SC unit cell.

The material system used to generate Figure 8 consists of pitch based carbon fibers in an epoxy matrix where the fiber conductivity is  $200 W/(m * K)$  while the matrix conductivity is  $0.3 W/(m * K)$  to match the material system used by Thornburg and Pears<sup>22</sup> and verify the thermal conductivity model. In general,

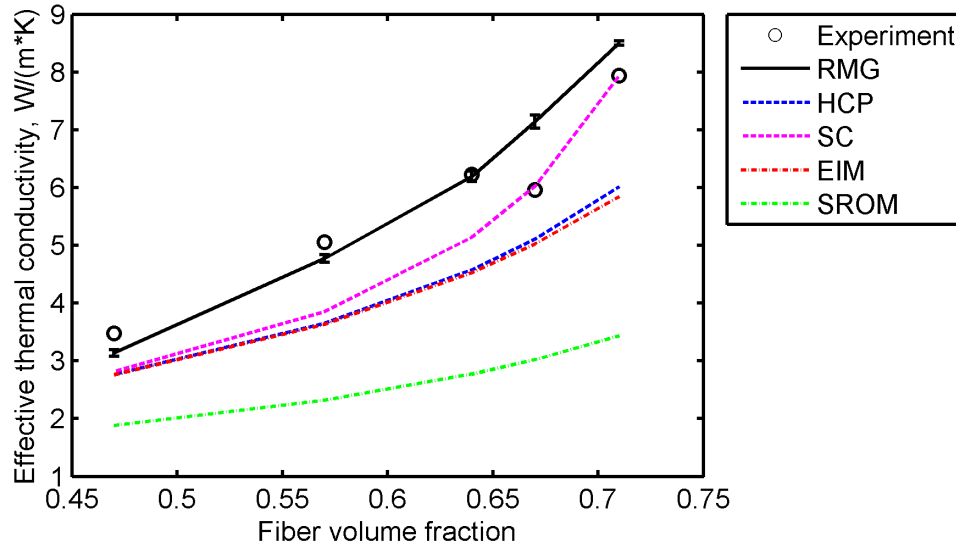


Figure 8. Effective through-thickness thermal conductivity predictions compared to literature values

as the ratio of fiber conductivity to matrix conductivity increases, the more the random arrangement and subsequent development of conductive paths will matter. It should be noted that Thornburg and Pears<sup>22</sup> observed a large increase in porosity in the two highest volume fraction composites, which could account for the non-monotonic behavior of the transverse thermal conductivity. As is shown in Figure 8, the SROM does a poor job of predicting the effective conductivity, but can still be used as a lower bound assuming perfect interfaces between constituents. The other analytic method included in Figure 8 is the EIM which agrees very closely with the hexagonal unit cell results; however, both of these methods predict lower conductivity than the experimental results, RMG FEM, and the SC unit cell method. The EIM is known to have limitations on conductivity ratios, which are exceeded in this particular case.<sup>9</sup>

The unit cell analyses fall victim to the some of the same shortcomings as the EIM in terms of neglecting conductive paths that may develop due to the stochastic nature of the microstructure. Another advantage of using the RMG FEM compared with other methods is the ability to perform stochastic simulations to find a range of properties. Standard error for each volume fraction simulated using the RMG FEM is found by generating 5 realizations of the same microstructure. The error bars included in Figure 8 are of standard error and are quite small even for a large conductivity mismatch ratio. Based on these results and literature knowledge, some computational expense may be saved by using an analytic method such as the EIM when the relative constituent properties, volume fraction, and interface properties are within the allowable range of the analytic method. In general, the EIM is valid for nearly all interface thermal resistance situations, low volume fraction, and a small mismatch ratio ( $< 100$ ) of fiber conductivity to matrix conductivity. The PMC system used in this work is based on the properties of PAN based carbon fibers, i.e. Toray T300<sup>TM</sup>, and the epoxy system EPON 828<sup>TM</sup> with thermal conductivities of  $10.46 \text{ W/(m} \cdot \text{K)}$  and  $0.223 \text{ W/(m} \cdot \text{K)}$  respectively. The thermal conductivity of the composite system as predicted by various methods is shown in Figure 9.

Much like the comparison in Figure 8, Figure 9 shows the RMG method consistently predicting the highest thermal conductivity of any method while the EIM analytic method and HCP unit cells agree very closely with each other. Also similar to Figure 8, Figure 9 shows that the conductivity predictions begin to diverge at larger fiber volume fractions, differing by 19% for SC unit cells and 22% for HCP unit cells and EIM at 60% fiber volume fraction. Assuming perfect interfaces, the reason for the higher conductivity in the RMG case is again because of the conductive paths that develop due to the random placement. Unsurprisingly the orientation of the unit cells has a negligible effect on the effective conductivity; however, unit cell orientation will prove to be a factor when considering effective optical properties.

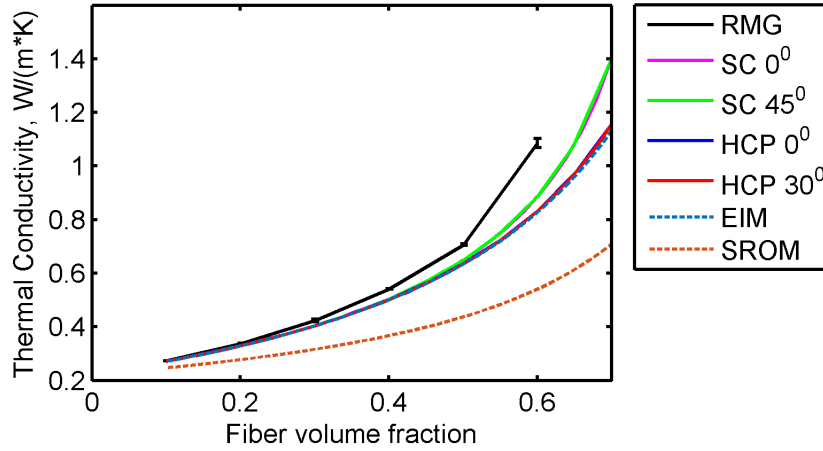


Figure 9. Thermal conductivity predictions of the PAN based carbon fiber-epoxy system

## B. Optical Properties

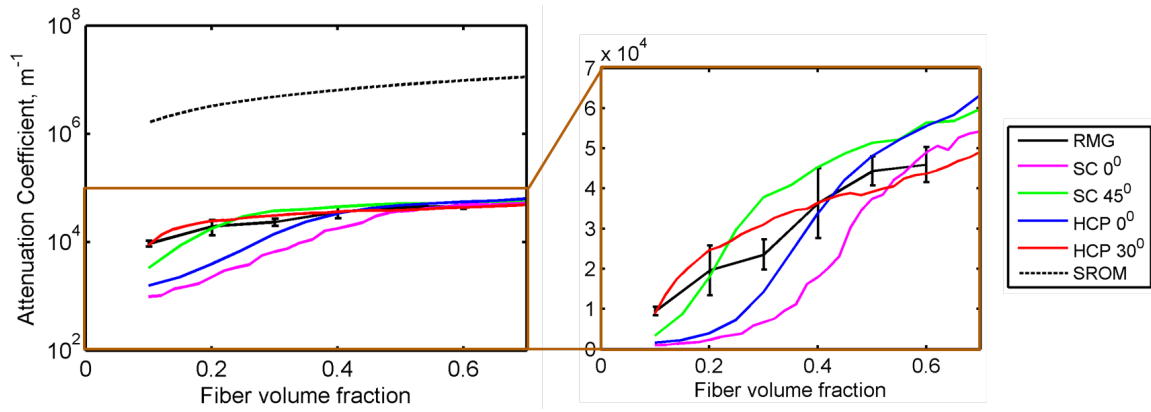
Effective optical properties are useful inputs to lower fidelity laser interaction models, or on their own as composite properties. However, the resulting temperature field can be found within the micromechanics framework without calculating the effective optical properties if the framework is fully coupled. The most important optical properties related to the thermal response are  $R$ ,  $T_r$ ,  $A$ , and  $\alpha_{eff}$ . These metrics together describe the magnitude and location of the transduction of optical energy to thermal energy. In the interest of balancing computational time and accuracy, the “Increase RVE depth” step shown in Figure 7 is limited to resizing to a maximum depth of  $150\ \mu\text{m}$ . As shown in Figure 5,  $150\ \mu\text{m}$  may not be considered optically thick for some synthetic generation methods at low volume fractions which means their transmission terms may be non-zero. However, because of the method used to determine effective attenuation coefficient, the RVE is not required to be optically thick to determine  $\alpha_{eff}$ . The material system used for optical simulation is also T300/EPON 828 with the electrical and optical properties summarized in Table 1. The fiber optical properties are the averaged from values for graphite and amorphous carbon since PAN based carbon fiber structure may be either of these depending on processing.<sup>23</sup> The electrical properties and matrix optical properties are specified by the manufacturer.

Table 1. Electrical and Optical Properties

Property	Epoxy	Fiber
Electrical conductivity, $\frac{S}{m}$	$10^{-12}$	58,862.5
Real refractive index	1.57	2.68
Imaginary refractive index	0	1.49

The combined effects of reflection, transmission, absorption, and scattering will all contribute to  $\alpha_{eff}$ . Considering that most reflection takes place near the surface and the transmission for a given RVE should be as close to zero as possible, the loss of intensity as a function of depth is primarily due to absorption and scattering. Scattering effectively increases the optical path length, which leads to more absorption if the fibers are in fact absorbing. The predictions for the effective attenuation coefficient as a function of volume fraction using various methods is shown in Figure 10.

Figure 10 indicates that the HCP  $30^\circ$  unit cell method most closely resembles the RMG method in terms of effective attenuation values. Considering Figures 5 and 10, the HCP  $30^\circ$  unit cell agrees with the RMG method on metrics related to optical interaction, but differs when considering thermal conductivity (Figure 9). The error bars present on the RMG results in Figure 10 are the standard error from 5 stochastic iterations at each volume fraction. Finding the  $\alpha_{eff}$  for a given volume fraction requires several stochastic simulations using the RMG method in order to predict a value with reasonable confidence. The SROM curve in Figure



**Figure 10. Effective attenuation coefficient ( $\alpha_{eff}$ ) as a function of volume fraction using various prediction methods.**

10 indicates that the simple analytic solution does not provide a reasonable approximation for  $\alpha_{eff}$  because it basically assumes that everything is absorbed at the surface. It should be noted that these assertions only apply to opaque fibers in a transparent matrix where the wavelength of the incident light is smaller than the fibers. The polarization dependence of these claims is also not evaluated in this work.

### C. Opto-Thermal Response

The temperature field due to incident optical energy will vary as a function of several parameters such as radiation duration and intensity, location (depth), thermal boundary conditions, wavelength, polarization, synthetic generation method, and composite type. Important composite properties that will affect the temperature solution include the constituent properties (optical and thermal), relative volume fractions of the fibers and matrix, and the thickness of the composite part. Though all these factors play a role in the thermal response, only the effects due to volume fraction and generation method are studied in this work. The fiber volume fraction is of particular interest because it is a physical property that impacts both the optical properties and effective thermal properties. The generation method has also been shown to affect both the effective conductivity (Figure 9) and the attenuation coefficient (Figure 10), however its effect is numerical and should be mitigated. The motivation to employ a unit cell method over the RMG method is to save computational time. The thermal response metrics considered are the surface temperatures as a function of time and the average temperature profile as a function of depth.

The temperature as a function of time is directly correlated with the total energy absorbed by the microstructure; therefore, if the synthetic generation method affects the overall power absorption it will ultimately influence the thermal response. For this material system, Figures 5 and 10 indicate that microstructure generation will affect temperature more severely at low volume fraction (10% - 20%) for SC 0°, HCP 0°, and SC 45° methods due to the difficulty of creating an optically thick RVE which in turn affects overall power absorption. The HCP 0° method at high volume fraction will also invoke a different thermal response due to a higher power absorption coefficient (0.879 at 60%) than all the other 2D FE methods (0.821-0.833 at 60%) which manifests as a higher temperature and faster temperature increase at both the front and back surfaces of the composite. The surface temperatures as a function of time are shown in Figure 11.

The SC 0°, HCP 0°, and SC 45° unit cell models show significantly lower surface temperatures at low volume fraction (Figures 11A and 11B) due to their inability to be optically thick within the 150  $\mu\text{m}$  depth constraint. Even at low volume fractions, the SFA predicts much higher temperatures at both the front and back surfaces which is a direct result of assuming all the incident energy is absorbed at the surface, which neglects possible reflections and multiple reflections due to the carbon fibers. Effectively, this means the SFA assumes more total energy is absorbed than the RMG and unit cell methods. A similar yet less severe effect is shown in Figures 11C and 11D for the HCP 0° method again because of a higher overall power absorption. The 1D RMG Input method agrees very closely with the RMG method for both high and low volume fraction composites which demonstrates the RMG method's usefulness as an input to lower fidelity models when trying to predict surface temperatures. The position of the knee of the curve in Figures 11B

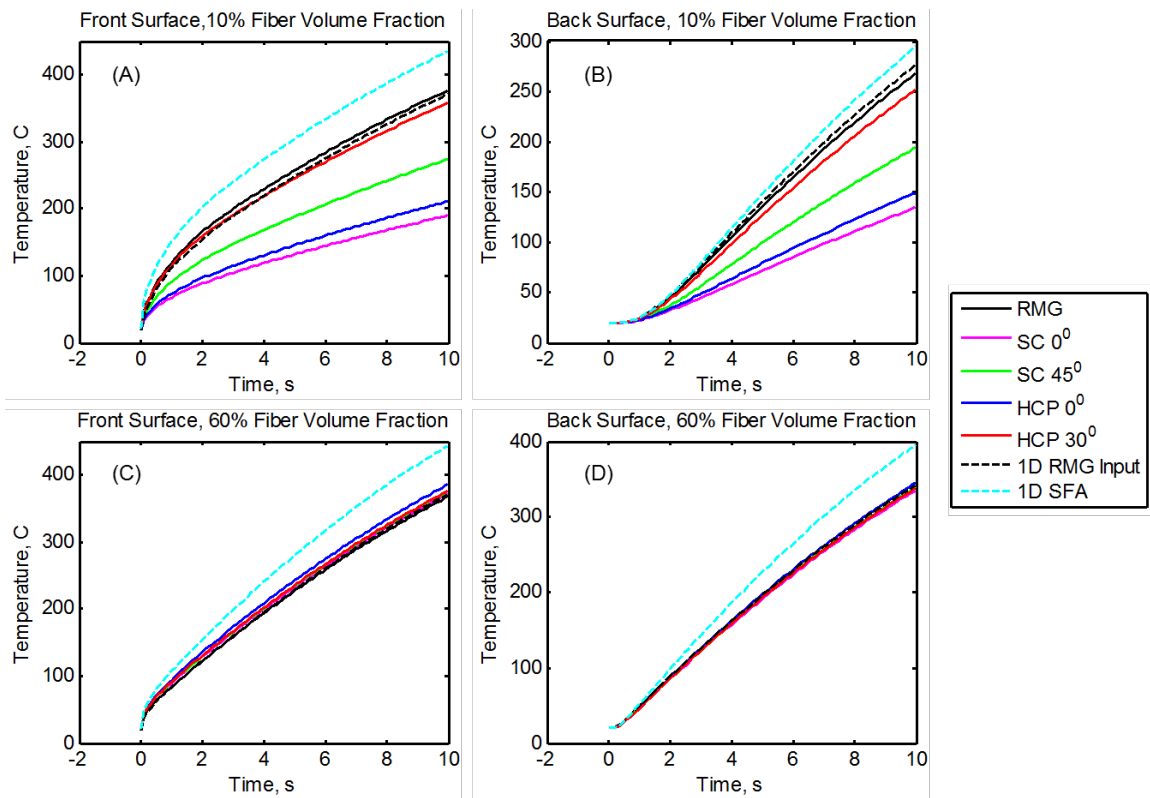


**Figure 11. Front and back surface temperatures as a function of time for 10% volume fraction and 60% volume fraction using various prediction methods.**

and 11D correspond to a Fourier number of approximately 1 when the total composite thickness is the characteristic length whereas this distance is typically the half width of a semi-infinite wall. As expected, the knee is pushed further to the right at low volume fractions due to the lower effective thermal diffusivity of the composite. Considering the knee in the back surface temperature curves, the temperature profile plots shown in Figure 12 occur at 2 seconds to ensure enough time has elapsed to allow thermal diffusion from the heat source in the RVE near the front surface to the back surface for all volume fraction conditions.

Figures 12A - 12D show interesting trends in agreement between the different methods used. At very low volume fraction (Figure 12A) the SC 0°, SC 45°, and HCP 0° predict much lower temperatures throughout the thickness due to not being optically thick, which is the same effect seen in the front and back surface temperature figures. However, the HCP 30°, 1D RMG Input, and the 1D SFA mostly agree except the 1D SFA near the surface and the overall temperature profile shape. The simultaneous agreement at the back surface and disagreement at the front surface can be attributed to the relative locations of the heat sources in each microstructure and the asymmetric thermal boundary conditions. The heat source in the SFA is directly at the surface with the largest heat transfer coefficient whereas the heat source in the RMG and HCP 30° is not as large overall, yet the sources are located somewhat below the surface. Since the effective conductivities are approximately equal at this low volume fraction, the thermal resistance between the heat source and the back surface is approximately equal in each case. Also aiding in the SFA and RMG method agreeing at very low volume fraction is the power reflection coefficient of the RMG is proportional to the volume fraction which means the overall heat source magnitude is more comparable between the RMG and SFA at very low volume fraction. The 1D RMG Input method and the RMG method mostly agree at low volume fraction except near the surface. This difference can be attributed to the method of applying the heat source as shown in Figure 6 where the 1D RMG Input method has the largest source at the surface as opposed to the RMG's largest heat source which is generally some distance below the surface.

Figure 12D shows that even though the total power input is approximately equal (except the SFA) the temperature profile and temperature gradient varies between microstructure generation types. The difference between the temperature profiles, their slope in particular, at high fiber volume fraction is due

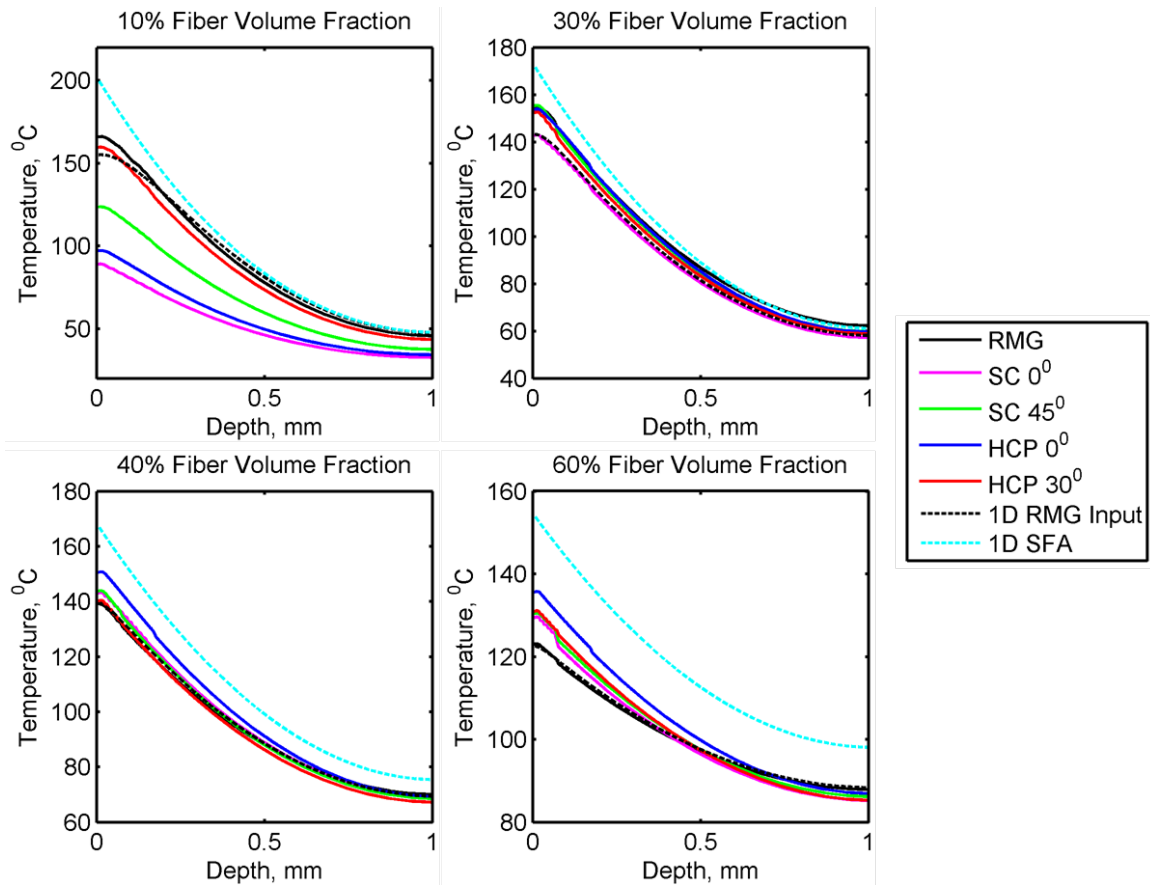


Figure 12. Temperature profiles through the depth using various prediction methods

to the differences in thermal diffusivity, especially in the regions with homogenized properties. The RMG method always predicts the highest thermal conductivity which causes it to have a more uniform temperature through the thickness, i.e. a higher back surface temperature and a lower front surface temperature than methods with comparable total power input. The 1D RMG Input model agrees very well with the RMG model at high volume fraction because the high density of fibers forces the largest part of the distributed heat source closer to the surface, which is what the 1D RMG Input model assumes. However, unlike the 1D SFA model, the 1D RMG Input model also accounts for total power reflection and uses the higher effective thermal conductivity values calculated by the RMG model. In comparing the 1D SFA model to the 1D RMG Input model, it is clear that accounting for reflection, a distributed heat source, and correct effective thermal conductivity is necessary to predict the thermal response with a low fidelity model.

At moderate volume fractions (30% and 40% in Figures 12B and 12C) the various prediction methods agree well with each other aside from the 1D SFA predicting somewhat higher temperature due to a larger total heat source. The agreement at these volume fractions represents a balance of two competing numerical mechanisms, optical absorption and effective thermal conductivity. The trade-off between thermal conductivity agreement and attenuation coefficient agreement as a function of volume fraction is shown in Figure 13.

Figure 13 shows better thermal conductivity agreement at lower volume fractions for various generation types whereas they begin to diverge at larger volume fractions. Meanwhile, it is difficult to achieve an optically thick RVE with good values for attenuation coefficient at low volume fraction with unit cell methods but easy to achieve this condition at high volume fraction. Thus, the various generation methods agree on thermal conductivity at low volume fraction and agree on optical absorption at high volume fraction. This trade-off is why the various generation methods do not agree at volume fraction extremes while agreeing much better at moderate volume fractions.



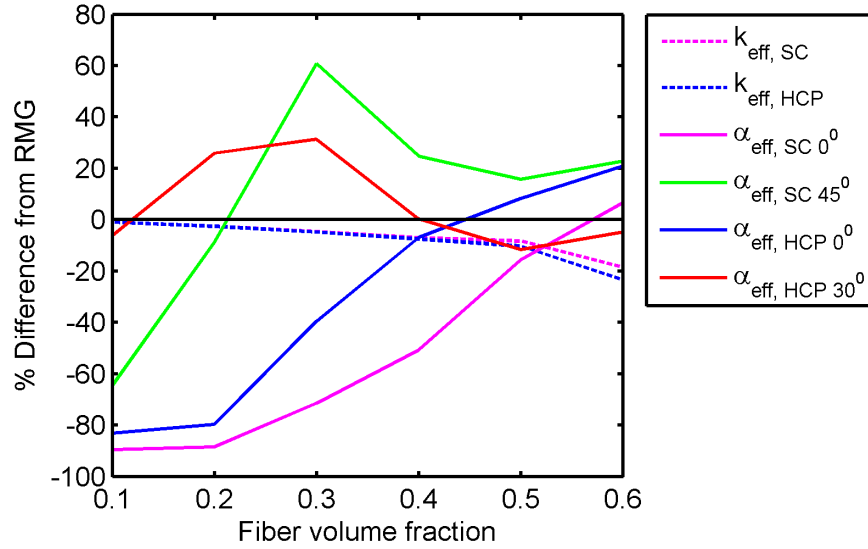


Figure 13. Relative agreement with RMG effective properties at various volume fractions for various generation methods.

## IV. Conclusion

We have developed a stochastic, micromechanics framework in Matlab and COMSOL to find the thermal response of a PMC due to incident optical energy. The micromechanics framework developed in this work finds the effective thermal properties, effective optical properties, heat source and thermal response to optical energy within the microstructure in a stochastic manner. We have shown that commonly employed analytic models cannot always sufficiently predict effective thermal properties and are not valid for optical property prediction. This work has also demonstrated the ability to solve the full wave solution of Maxwell's equations inside the random and ordered microstructure of a composite which accounts for diffraction and interference effects that are neglected by geometric optics and surface flux approximations.

Effective thermal properties can generally be found using analytic expressions or unit cell analysis in many composite systems, but it was shown that this is not the case all composite systems and accurate prediction of the effective conductivity is vital to predicting the opto-thermal response. The applicability of this model was demonstrated in a composite with high thermal conductivity mismatch ratio where the series resistance between the fibers (a function of fiber spacing and matrix conductivity) plays a large role. Although unit cell analysis can typically be used to find effective thermal properties, it does not perform well when finding effective optical properties due to the fundamental differences between thermal diffusion and wave propagation.

The periodic nature of the unit cell method allows clear propagation paths at lower volume fractions within the microstructure that are highly unlikely to arise in real composites. These paths diminish the contribution of the fiber properties to the effective optical properties when the matrix is transparent. Should the optical properties of the matrix and the fibers be reversed, the effect of the periodic arrangement of the fibers may not have as much impact on the results. Thus, for the case of highly absorbing fibers in a transparent matrix, a random microstructure must be used as opposed to a periodic microstructure in order to find effective optical properties, especially the total power input and the effective attenuation coefficient.

The thermal response to optical energy takes into account both the effective thermal properties and the optical absorption of the composite. We have assessed the applicability of using a unit cell analysis, 1D thermal analysis, and a random RVE to find the thermal response of a composite due to absorption of optical energy. At low volume fractions, the unit cell models predict lower temperatures than the RMG model due to their higher transmission (smaller attenuation coefficient) through the RVE, thus reducing the heat source. However, at higher fiber volume fraction the unit cell methods predict higher temperatures on the front surface and lower temperatures at the back surface when compared to the RMG method. This is due to the effective attenuation coefficients and total power input being approximately the same but the effective

conductivity is higher when using the RMG method which allows more efficient dissipation of the thermal energy through the thickness of the composite. Two 1D transient thermal models were also evaluated for their ability to predict the temperature profile through the thickness. It was shown that the SFA assuming that all energy is absorbed at the surface leads to much higher temperature predictions than all the other methods. This is primarily due to neglecting reflections and assuming the heat source is concentrated at the surface instead of being applied as a distributed source.

The agreement between the 1D RMG Input model and the RMG model demonstrates the usefulness of this micromechanics framework and its ability to find effective optical and thermal properties which can subsequently be used as inputs to lower fidelity models. The developed framework predicts the microscale thermal response of composites under laser irradiation for various composite properties which allows optimization of processing steps such as laser curing and thermoplastic consolidation where the desired temperature response is within a certain range. The full wave solution within the microstructure includes the effects of fiber arrangement and other microscale inclusions that can significantly affect laser absorption and subsequent heat transfer. These microscale effects, which can manifest as a macro scale temperature response, are neglected by lower fidelity models and are not fully captured by geometric optics approximations.

## Acknowledgments

This work is sponsored by the Air Force Research Laboratory, Materials and Manufacturing Directorate, WPAFB under Air Force Contract No: FA8650-10-D-5011. We would also like to thank Antonio Melro formerly from the Universidade do Porto and now with the University of Bristol for providing the RMG algorithm.

## References

- <sup>1</sup>Wahab, M. S., Rahim, E. A., Mustafa, M. S., and Rahman, N. A., "The effect of laser cutting parameters on the aerospace structure panel of CFRP composite material," *AEROTECH IV - 2012, November 21, 2012 - November 22, 2012*, Vol. 225 of *Applied Mechanics and Materials*, Trans Tech Publications, 2012, pp. 127–131.
- <sup>2</sup>Head, J. D. and Niedzielski, J. P., "Laser Paint Stripping." Tech. rep., United States, June 1991.
- <sup>3</sup>Stokes-Griffin, C. M. and Compston, P., "A combined optical-thermal model for near-infrared laser heating of thermoplastic composites in an automated tape placement process," *Composites Part A: Applied Science and Manufacturing*, Vol. 75, Aug. 2015, pp. 104–115.
- <sup>4</sup>Negarestani, R., Sundar, M., Sheikh, M. A., Mativenga, P., Li, L., Li, Z. L., Chu, P. L., Khin, C. C., Zheng, H. Y., and Lim, G. C., "Numerical simulation of laser machining of carbon-fibre-reinforced composites," *Proceedings of the Institution of Mechanical Engineers, Part B: Journal of Engineering Manufacture*, Vol. 224, No. 7, July 2010, pp. 1017–1027.
- <sup>5</sup>Abliz, D., Duan, Y., Steuernagel, L., Xie, L., Li, D., and Ziegmann, G., "Curing methods for advanced polymer composites -A review," *Polymers and Polymer Composites*, Vol. 21, No. 6, 2013, pp. 341–348.
- <sup>6</sup>Vila Verde, A., Ramos, M. M. D., Stoneham, M., and Mendes Ribeiro, R., "Mesoscopic modelling of the interaction of infrared lasers with composite materials: an application to human dental enamel," *Applied Surface Science*, Vol. 238, No. 14, Nov. 2004, pp. 410–414.
- <sup>7</sup>Fernandes, H. and Maldague, X., "Fiber orientation assessment on surface and beneath surface of carbon fiber reinforced composites using active infrared thermography," *Thermosense: Thermal Infrared Applications XXXVI, 5 May 2014*, Vol. 9105 of *Proc. SPIE, Int. Soc. Opt. Eng. (USA)*, SPIE - The International Society for Optical Engineering, 2014, p. 91050D (9 pp.).
- <sup>8</sup>Benveniste, Y., Chen, T., and Dvorak, G. J., "The effective thermal conductivity of composites reinforced by coated cylindrically orthotropic fibers," *Journal of Applied Physics*, Vol. 67, No. 6, 1990, pp. 2878–2884.
- <sup>9</sup>Hasselman, D. P. H. and Johnson, L. F., "Effective thermal conductivity of composites with interfacial thermal barrier resistance," *Journal of Composite Materials*, Vol. 21, No. 6, 1987, pp. 508–515.
- <sup>10</sup>Hatta, H. and Taya, M., "Thermal conductivity of coated filler composites," *Journal of applied physics*, Vol. 59, No. 6, 1986, pp. 1851–1860.
- <sup>11</sup>Lu, Y., Donaldson, K. Y., Hasselman, D. P. H., and Thomas, J. R., "Thermal conductivity of uniaxial coated cylindrically orthotropic fiber-reinforced composite with thermal barriers," *Journal of composite materials*, Vol. 29, No. 13, 1995, pp. 1719–1724.
- <sup>12</sup>Sihn, S. and Roy, A. K., "Micromechanical analysis for transverse thermal conductivity of composites," *Journal of Composite Materials*, 2010, pp. 0021998310382311.
- <sup>13</sup>Springer, G. S. and Tsai, S. W., "Thermal conductivities of unidirectional materials," *Journal of Composite Materials*, Vol. 1, No. 2, 1967, pp. 166–173.
- <sup>14</sup>Alcaraz, D., Moreno, J., and Alhama, F., "Thermal conductivity estimation in continuous fiber metal matrix composites with random distributions," *THERMEC'2003. International Conference on Processing and Manufacturing of Advanced Materials, 7-11 July 2003*, Vol. 426-432 of *Mater. Sci. Forum (Switzerland)*, Trans Tech Publications, 2003, pp. 2169–74.
- <sup>15</sup>Ishimaru, A., *Wave Propagation and Scattering in Random Media*, IEEE Press, 1997.

- <sup>16</sup>Boley, C. D. and Rubenchik, A. M., "Modeling of laser interactions with composite materials," *Applied optics*, Vol. 52, No. 14, 2013, pp. 3329–3337.
- <sup>17</sup>Melro, A. R., Camanho, P. P., and Pinho, S. T., "Generation of random distribution of fibres in long-fibre reinforced composites," *Composites Science and Technology*, Vol. 68, No. 9, 2008, pp. 2092–2102.
- <sup>18</sup>Romanov, V., Lomov, S. V., Swolfs, Y., Orlova, S., Gorbatiikh, L., and Verpoest, I., "Statistical analysis of real and simulated fibre arrangements in unidirectional composites," *Composites Science and Technology*, Vol. 87, 2013, pp. 126–134.
- <sup>19</sup>Islam, M. R. and Pramila, A., "Thermal conductivity of fiber reinforced composites by the FEM," *Journal of Composite Materials*, Vol. 33, No. 18, 1999, pp. 1699–1715.
- <sup>20</sup>Vila Verde, A., Ramos, M. M. D., Stoneham, M., and Mendes Ribeiro, R., "Mesoscopic modelling of the interaction of infrared lasers with composite materials: an application to human dental enamel," *Applied Surface Science*, Vol. 238, No. 14, Nov. 2004, pp. 410–414.
- <sup>21</sup>Parandoush, P. and Hossain, A., "A review of modeling and simulation of laser beam machining," *International Journal of Machine Tools and Manufacture*, Vol. 85, Oct. 2014, pp. 135–145.
- <sup>22</sup>Thornburg, J. D. and Pears, C. D., "Prediction of the thermal conductivity of filled and reinforced plastics," ASME, 1965.
- <sup>23</sup>Kong, L., Liu, H., Cao, W., and Xu, L., "PAN fiber diameter effect on the structure of PAN-based carbon fibers," *Fibers Polym*, Vol. 15, No. 12, Jan. 2015, pp. 2480–2488.

## LIST OF ACRONYMS, ABBREVIATIONS, AND SYMBOLS

AFM	atomic force micrograph
AFRL	Air Force Research Laboratory
ALD	atomic layer deposition
BMI	bismaleinimide
BMPPM	bismaleimidodiphenyl methane
FEA	Finite element analysis
FEM	finite element models
ICMSE	Integrated computational materials science and engineering
MD	molecular dynamics
OMC	organic matrix composite
SThM	scanning thermal microscopy
WPAFB	Wright-Patterson Air Force Base